

University of Pretoria etd – Kock, L.D. (2009)

**Raman spectroscopic studies of the
underglaze pigments of porcelain shards
of archaeological origins**

by

Lesotlho David Kock

Submitted in partial fulfilment of the degree

PHILOSOPHIAE DOCTOR

in

CHEMISTRY

Faculty of Natural and Agricultural Sciences of the

**UNIVERSITY OF PRETORIA
PRETORIA**

Promoter: Prof. P.H. van Rooyen

Co-promoter: Prof. S.O. Paul

October 2009

Declaration

I, Lesotlho David Kock, the author of the current thesis entitled “Raman spectroscopic studies of the underglaze pigments of porcelain shards of archaeological origins”, declare that the thesis contains only original work and that all the results included were generated by the author.

Signature:.....

Date:.....

Acknowledgements

The author wishes acknowledge the following:

- Prof. P.H. van Rooyen (promoter) and Prof. S.O. Paul (co-promoter) for undertaking the mammoth task of picking up in the middle of my work in difficult circumstances
- Prof. Ignacy Cucrowski for excellent advice and encouragement which allowed me to complete this work
- Dr Danita de Waal for her guidance in the initial research leading to this work
- Colleagues and friends who were an inseparable part of my life during the compilation of this work
- Ms Tina Joemat-Pettersson and Dr Juanita Fleming for their support
- To my wife, Noluthando, the children Dineo, Ofentse and Lesego, and my mother, Mrs Sinah Moloto, and my mother in law Mrs Georgina Sidwaba for always being there when I needed them
- The University of Pretoria and the National Research Foundation (NRF) for their financial support.

Summary

The technique of Raman spectroscopy was used in a study of shards of known (Ming and Meissen) and unknown (archaeological) origin. A tile shard from the Citadel of Algiers was included in this study as further confirmation of the consistency of the methods that are developed. The Citadel from which the tile shard was obtained was built in 1516 and represents a landmark from pre-colonial Algeria. The results were compared with those obtained from studies on intact museum pieces of known (Ming) origin. A consistent method of studying underglaze pigments on glazed ceramic artifacts by directing the laser beam through the predominantly silicate glaze was developed. The glaze depth profiling method developed proved to be very useful in the analysis and gives not only a detailed composition for the glaze/ceramic interfacial pigment, but also the order in which the various interfacial pigment layers were applied at the time of manufacture.

The information acquired leads to an understanding of the level of technological development of the manufacturers. The detailed study and characterisation of the pigments that were analysed in this way gives insight into trade relations among ancient societies of the Mediterranean and will also assist archaeologists in establishing cut-off dates for the archaeological sites from which the artifacts were recovered. All the shards, except one from Meissen (Germany), were provided by the National Cultural History Museum of South Africa and the intact Ming dynasty plates were provided by the J.A. van Tilburg Museum of the University of Pretoria. The tile shard sample from the Citadel of Algiers was donated for the study.

The results indicate that none of the archaeological shards could possibly be of Ming dynasty origin based on, firstly, the use of amorphous carbon to darken the cobalt blue (CoAl_2O_4) used as decoration on the shards, and secondly on the use of white (synthetic) anatase to whiten the ceramic surface before the application of the

pigment since this synthetic anatase is known to have been manufactured for the first time around 1920.

An ancient rediscovered ternary pigment ($\text{Pb}_2\text{SnSbO}_{6.5}$) previously found on Italian paintings of the 16th century, for example, “Lot and his daughters” by G.B. Langetti and “Entrance of Christ in Jerusalem” by Luca Giordano, was identified on the Citadel tile and successfully characterised. A Pb-O vibrational Raman band at 127 cm^{-1} for this pigment was assigned for the first time. Additional pigments identified on the tile include Naples yellow ($\text{Pb}_2\text{Sb}_2\text{O}_7$), lead (II) stannate (Pb_2SnO_4), cobalt blue (CoAl_2O_4) and cassiterite (SnO_2). The bulk of the tile body is composed mainly of hematite ($\alpha\text{-Fe}_2\text{O}_3$), maghemite ($\gamma\text{-Fe}_2\text{O}_3$), magnetite (Fe_3O_4) and quartz ($\alpha\text{-SiO}_2$), with traces of calcite (CaCO_3) and amorphous carbon. The unique non-destructive depth profiling method that was developed in this study can now be applied to the study of underglaze pigments on intact porcelain artifacts in museums and private collections around the world for authentication purposes and for comparison with archaeological shard samples.

Table of contents

DECLARATION.....	II
ACKNOWLEDGEMENTS	III
SUMMARY	IV
LIST OF FIGURES	X
LIST OF TABLES.....	XVI
CHAPTER 1.....	1
Introduction 1	
1.1 Background.....	1
1.2 Statement of the problem.....	2
1.3 Fluorescence: Impediments to the study of underglaze pigments	4
1.4 Pigment characterisation	5
1.5 Glaze characterisation	6
1.5.1. Glaze type and composition.....	6
1.5.2. Glaze transition temperature.....	7
1.5.3. Glaze microstructure.....	7
1.6 Conclusion	8
1.7 References	9
CHAPTER 2.....	12
Literature review	12
2.1 Studies of glazed blue and white porcelain.....	13
2.1.1. Glaze composition studies	15
2.1.2. Pigment analysis studies	15
2.1.3 Porcelain body studies.....	17
2.2 Pigment analysis on glazed tiles.....	17

University of Pretoria etd – Kock, L.D. (2009)

2.3.	Conclusion	18
2.4	References	20
CHAPTER 3.....		24
Synthesis and analysis techniques.....		24
3.1	Theory of Raman spectroscopy	24
3.2.	Applications of the techniques used in the study	30
3.2.1.	Raman experiments.....	30
3.2.2.	Powder X-ray diffractometry (XRD)	32
3.2.3.	Energy dispersive X-ray spectrometry	34
3.3.	Synthesis of selected reference compounds	35
3.3.1.	Cobalt aluminium oxide or cobalt blue (CoAl_2O_4).....	35
3.3.2.	Ternary (Pb-Sn-Sb) oxide ($\text{Pb}_2\text{SnSbO}_{6.5}$)	37
3.3.3.	Preparation of lead (II) stannate (Pb_2SnO_4).....	38
3.4.	Conclusion	40
3.5	References	42
CHAPTER 4.....		44
Underglaze pigments on shards and plates		44
4.1	Glaze depth profiling	44
4.2.	Ceramic/glaze interfacial structure.....	47
4.3.	Identification of pigments, characterisation and implications	51
4.3.1.	Cobalt aluminium oxide (CoAl_2O_4).....	51
4.3.2.	Amorphous carbon	63
4.3.3.	Anatase (TiO_2)	65
4.3.4	Rutile (TiO_2).....	66
4.3.5	Hematite ($\alpha\text{-Fe}_2\text{O}_3$)	67
4.3.6	Mullite ($2\text{Al}_2\text{O}_3\cdot\text{SiO}_2$ or $3\text{Al}_2\text{O}_3\cdot 2\text{SiO}_2$).....	69
4.4	Intact plates	70

University of Pretoria etd – Kock, L.D. (2009)

4.4.1	Ming dynasty plates Hongzhi (1488–1505) and Wanli (1573–1620) 70	
4.4.2	Unknown intact plate	73
4.5	Conclusion	77
4.6	References	78
CHAPTER 5.....		81
Pigments on a tile from the Citadel of Algiers.....		81
5.1	Tile history and description	81
5.2	Pigment analysis on the Citadel tile	84
5.2.1	Yellow pigments.....	85
5.2.1.1	Ancient rediscovered yellow pigment ($\text{Pb}_2\text{SnSbO}_{6.5}$).....	86
5.2.1.2	Naples yellow or lead antimonite ($\text{Pb}_2\text{Sb}_2\text{O}_7$)	95
5.2.1.3	White pigment: cassiterite (SnO_2).....	96
5.2.1.4	Blue pigment: cobalt aluminium oxide (CoAl_2O_4)	98
5.3	Tile body analysis	101
5.3.1	Iron oxides	102
5.3.1.1	Hematite ($\alpha\text{-Fe}_2\text{O}_3$)	102
5.3.1.2	Maghemite ($\gamma\text{-Fe}_2\text{O}_3$)	103
5.3.1.3	Magnetite (Fe_3O_4).....	103
5.3.2	Quartz ($\alpha\text{-SiO}_2$)	103
5.3.3	Calcite (CaCO_3)	104
5.3.4	Amorphous carbon	105
5.4	Implications for restoration and preservation	105
5.5	Conclusion	106
5.6	References	107
APPENDIX 5.1.....		109
EDX data: Yellow section of Citadel tile.....		109

CHAPTER 6.....	112
Glaze analysis of shards and plates	112
6.1. Glaze analysis method.....	112
6.2. Application to blue and white porcelain glaze	114
6.2.1. Samples.....	115
6.2.2. Raman and EDX measurements	116
6.2.3. Results on sample glazes	118
6.4 Conclusion	123
6.5 References	124
CHAPTER 7.....	125
Overall conclusion.....	125

List of Figures

- Figure 1.2.1.** Due to the inability of researchers to access the pigment of glazed artifacts through the glaze, a shard was often placed in the position shown above in order to access the underglaze pigment on glazed artifacts. This effectively ruled out studies on intact museum pieces where the pigment is not exposed to the surface 3
- Figure 2.1.** Diagram showing the interdisciplinary nature of art analysis and how it relates to a number of research fields (adapted and modified from Vandenaabeele¹⁸)..... 13
- Figure 3.1.1.** Illustration of the normal Raman scattering showing Rayleigh, Stokes and anti-Stokes components. The far right depicts fluorescence radiation that, when present, often swamps the Raman signal 28
- Figure 3.2.1.1.** Schematic view of the micro-Raman 180° back-scattering configuration [adapted from: www.ens-lyon.fr/LST/Raman; accessed 20/7/2008]. See also Clark, R.J.H., C. R. *Chimie* 2002, **5**, 7..... 31
- Figure 3.2.2.1.** Schematic view of X-ray diffraction from the sample. The scattered radiation contains information on the type and spacing of the atoms in the sample. [adapted from: www.eserc.stonybrook.edu/ProjectJava/Bragg/; accessed 1/4/2009]..... 32
- Figure 3.3.1.1. (a-b).** Raman spectra of two samples of cobalt blue that were cooled at different rates: (a) cooled slowly and (b) cooled rapidly, at a wavenumber resolution of 2 cm⁻¹..... 36
- Figure 3.3.1.2.** The XRD pattern in this figure is representative of the cobalt blue samples that were cooled rapidly by immediate removal from the furnace..... 37
- Figure 3.3.3.1.** The XRD pattern in this figure is representative of the product in equation 3.1 and has been identified as lead tin yellow type I or lead stannate 39

- Figure 3.3.3.2.** The Raman spectrum of lead (II) stannate (lead tin yellow type I). Incident radiation was 514.5 nm wavelength radiation, with 0.3 mW laser power at the sample. Integration time was 10 seconds and 1 accumulation with wavenumber resolution of 2 cm^{-1} 39
- Figure 4.1.1.** Schematic view of the focus positions for both the glaze surfaces and the ceramic/glaze interface 45
- Figure 4.1.2.** Typical positioning of a precious porcelain museum piece for glaze depth profile studies using micro-Raman spectroscopy (unknown plate from the J.A. van Tilburg Museum, University of Pretoria)..... 46
- Figure 4.1.3.** The set of samples chosen for this study is shown. Samples A and B are of Ming dynasty origin; samples C, D and F are archaeological samples; sample E is of Meissen origin; and samples H and I are intact Ming plates 46
- Figure 4.2.3.** Schematic view of the ceramic/glaze interfacial region as determined through generating a typical glaze profile with micro-Raman spectroscopy on dark blue sections of sample C (see Figure 4.1.3)..... 49
- Figure 4.2.4.** Raman spectra in which the glaze surface spectrum in (a) at $0\ \mu\text{m}$ shows only the glaze. The spectra shown from 100 to $120\ \mu\text{m}$ for this sample D (unknown shard) typically show the spectral evolution of the interfacial region 49
- Figure 4.2.5.** Schematic view of the ceramic/glaze interfacial region as determined from the Raman glaze profile in Figure 4.2.4 50
- Figure 4.3.1.1.** The Raman spectra of cobalt blue cooled rapidly (a), cooled slowly (b) and a commercial sample (c); the commercial sample was supplied by *Farbmühle Kraemer* in Germany and was used as received 52
- Figure 4.3.1.1.** (B) A representative Raman spectrum of an underglaze blue pigment at the ceramic/glaze interface showing all the identified Raman bands. The broad band at 1007 cm^{-1} is due to the silicate glaze, while the shoulder at around 410 cm^{-1} (not labelled) is due to cobalt blue 61

-
- Figure 4.3.1.2.** The figure shows an XRD pattern of synthesised cobalt blue showing cobalt blue as the only phase present in the sample. This sample was removed from the furnace and allowed to cool slowly 61
- Figure 4.3.1.3.** The surface (a) and interface (b) spectra for the Meissen sample E (Figure 4.1.3 (E)), is typical for all the blue and white porcelain blue pigment in our possession. The 461 cm^{-1} Raman band is attributed to α -quartz which is similar to all the blue and white porcelain in our study 62
- Figure 4.3.3.1.** (a) Rutile (TiO_2) spectrum, with characteristic Raman bands at 244 cm^{-1} (A_{1g}), 440 cm^{-1} (E_g) and 609 cm^{-1} (B_{1g}), and (b) anatase (TiO_2) spectrum, with bands at 140 cm^{-1} (E_g), 197 cm^{-1} (E_g), 394 cm^{-1} (B_{1g}), 517 cm^{-1} (B_{1g}) and 637 cm^{-1} (E_g). Both (a) and (b) are recorded from the ceramic body of sample E (Meissen) 66
- Figure 4.3.5.1.** The brown line at the bottom of Ming sample B is indicated with an arrow. This line is more prominent on the inside bottom than the outside bottom where it appears to have been scraped off 68
- Figure 4.3.5.2.** Spectrum showing typical $\alpha\text{-Fe}_2\text{O}_3$ Raman bands at 221 cm^{-1} (A_{1g}), 294 cm^{-1} (E_g), 409 cm^{-1} (E_g) and 601 cm^{-1} (E_g) as collected directly from the brown line of sample B, indicated with an arrow in Figure 4.3.4.1 68
- Figure 4.3.6.1.** Spectrum of mullite in the ceramic body of the Meissen sample (Figure 4.1.3 (E)) with Raman bands at 320 cm^{-1} , 485 cm^{-1} , 600 cm^{-1} , 960 cm^{-1} and 1129 cm^{-1} 70
- Figure 4.4.1.1.** Surface (a) and interface (b) spectra for the Ming plate (Hongzhi (1488 – 1505)) shown also in Figure 4.1.3 (H). Note the glaze thickness of about $390\text{ }\mu\text{m}$ 71
- Figure 4.4.1.2.** Surface (a) and interface (b) spectra for the Ming plate (Wanli (1573–1620)) shown also in Figure 4.1.3 (I). Note the glaze thickness of about $420\text{ }\mu\text{m}$ on this plate 72

-
- Figure 4.4.2.1.** Unknown intact plate, showing the various positions chosen for study 73
- Figure 4.4.2.2.** Glaze depth profile showing a predominantly cassiterite (SnO_2) glaze (position A in Figure 4.4.2.1). The blue pigment is not detected here despite the visibly blue glaze 74
- Figure 4.4.2.3.** Glaze depth profile for the unknown plate (position B in Figure 4.4.2.1). The blue pigment on this plate shows that it has an olivine-type pigment and is more intense on the glaze surface rather than the glaze interior 75
- Figure 4.4.2.4.** Raman spectrum of the “golden” rim, showing rutile as the main component as indicated by the main Raman bands with traces of anatase (140 cm^{-1}) and CaCO_3 . (1086 cm^{-1}) 76
- Figure 5.1.1.** The different views of the Citadel tile highlight the different colours (above) and the relative thickness of the tile body (below) with respect to the glaze thickness 82
- Figure 5.2.1.1.1.** This Figure shows spectra of the various shades of yellow pigment with 568 nm wavelength radiation at 0.5 mW at the sample. The wavenumber resolution is 2 cm^{-1} 87
- Figure 5.2.1.1.2.** Raman spectrum of sample (a) in Table 5.2.1.1.1. The Raman bands at 210 cm^{-1} and 655 cm^{-1} are assigned to trace amounts of rosielite (PbSb_2O_6). A 514.5 nm wavelength radiation, 0.3 mW laser power at the sample, with 2 cm^{-1} wavenumber resolution was used 89
- Figure 5.2.1.1.3.** The XRD pattern of sample (a) in Table 5.2.1.1.1, shows the ternary pyrochlore as the dominant product. The asterisks are used to show the ternary compound ($\text{Pb}_2\text{SnSbO}_{6.5}$) 90

-
- Figure 5.2.1.1.4.** The Raman spectrum of sample (e) in Table 5.2.1.2. is consistent with the XRD data. This sample shows two sharp Raman bands at 210 cm^{-1} and 655 cm^{-1} characteristic of PbSb_2O_6 , in addition to the other Raman bands. 91
- Figure 5.2.1.1.5.** XRD pattern of the synthetic rosiite (PbSb_2O_6) with trace amounts of the unknown compound $\text{Pb}_{3+x}\text{Sb}_2\text{O}_{8+x}$ indicated with a star 92
- Figure 5.2.1.1.6.** Raman spectrum of sample (d) in Table 5.2.1.2, consistent with Pb_2SnO_4 (see also row one of Table 5.2.1.1 from Clark³ for the Raman band assignments for this compound) 92
- Figure 5.2.1.1.7.** EDX spectra of the brown line on the Citadel tile. The ratio of Pb:Sn = 2.19 is close to that of Pb_2SnO_4 . The sample penetration depth is in the order of $20\text{ }\mu\text{m}$ 93
- Figure 5.2.1.1.8.** Raman spectrum of the tile pigment showing the presence of lead tin yellow type II ($\text{PbSn}_{1-x}\text{Si}_x\text{O}_3$) on the tile shard 94
- Figure 5.2.1.2.1.** Naples yellow Raman spectrum as identified on the Citadel tile. The wavelength of the excitation line was 514.5 nm and the power at source was 0.5 mW 95
- Figure 5.2.1.3.1.** Two Raman bands for white pigment: the spectrum in (a) is that from the white pigment on the Citadel tile and (b) is that of a reference compound SnO_2 97
- Figure 5.2.1.4.1.** The cross-section of the blue background from the tile shard is shown. The blue pigment is shown spread homogeneously through the top section of the tile shard and could be the result of dissolved cobalt 99
- Figure 5.2.1.4.2.** Glaze depth profile Raman spectra, which does not show the identity of the blue colour but shows that cassiterite and quartz form part of the glaze 99
- Figure 5.3.1.1.1.** The presence of hematite ($\alpha\text{-Fe}_2\text{O}_3$) is indicated by the observation of all the hematite Raman bands in Figure 5.3.1.1.1(a) 102

-
- Figure 5.3.4.1.** Both glassy silica (a) and quartz (b) were detected on the body of the tile. Amorphous carbon and traces of calcite were also detected as shown in (c) 104
- Figure 5.3.6.1.** Amorphous carbon inclusions found in the glaze and presumed to be contamination that occurred during the manufacturing process. This photo was acquired with an Olympus camera mounted on top of the microscope using a 50X objective lens..... 105
- Figure 6.1.1.** In highly connected SiO_4 tetrahedral units, such as in the SiO_2 network, the bending vibrations illustrated here with white arrows are most intense and are associated with the 500 cm^{-1} envelope in the Raman spectrum (Silicon atoms are the grey spheres and the red spheres are those of oxygen atoms.) [The Figure was obtained and modified from Kotz, J.C. and Treichel, P. Chemistry and Chemical Reactivity, 4th Ed, Harcourt Brace College Publishers, Orlando, Florida USA.]..... 113
- Figure 6.2.1.1.** These sets of shards and intact plates are those that were used for the glaze analysis. Samples A and B are Ming shards, C, D and F are of archaeological origin, E is of Meissen origin, H and I are intact museum collection pieces and G is the tile shard from the Citadel of Algiers..... 116
- Figure 6.2.2.1.** The Figure illustrates the position of the shard in a normal horizontal position for probing the glaze directly. This position is also ideal for probing the ceramic/glaze interface through the glaze on the shards..... 117
- Figure 6.2.3.3.** Representative deconvolution results from glaze spectra (514.5 nm wavelength radiation; 50X objective lens). Figure 4.2.1. (a) was used in the illustrated deconvolution. 119
- Figure 6.2.3.4.** Plot of the A_{500}/A_{1000} ratio (index of polymerisation, I_p) of the various samples. This ratio has been found to correlate closely with the sintering temperature of the glaze 121

List of Tables

- Table 3.2.2.1.** The Instrument and data collection parameters for the Siemens D 501 XRD instrument that was used to collect XRD data on reference samples are given in this table. The samples were prepared using standard Siemens sample holders and the powder was pressed into the holder using a glass slide 34
- Table 3.3.2.1.** The various samples that were prepared for the purpose of identifying the pigments on the Citadel tile..... 38
- Table 4.3.1.1.** The values of the species that are chosen are shown below and depend on the type of crystal or molecule being considered. 54
- Table 4.3.1.2.** The distinct kinds of T_d , D_{3d} and C_{3v} sites and the number of equivalent atoms that can occupy each distinct site within the same distinct kind of site 56
- Table 4.3.1.3.** Aluminium atom site D_{3d} , with the degree of vibrational freedom for each species ($n = 4$ atoms / equivalent set)..... 56
- Table 4.3.1.4.** Cobalt atom site T_d , with the degree of vibrational freedom for each species ($n = 2$ atoms / equivalent set) 57
- Table 4.3.1.5.** Oxygen atom site C_{3v} , with the degree of vibrational freedom for each species ($n = 8$ atoms / equivalent set) 57
- Table 4.3.1.6.** Correlation between the D_{3d} site group and the O_h^7 factor group for the aluminium atoms ($n = 4$ atoms / equivalent set). Note that italicised T in the t^Y column designates translations, while the non-italicised T designates the degeneracy of a particular symmetry species..... 58
- Table 4.3.1.7.** Correlation between the T_d site group and the O_h^7 factor group for the cobalt atoms ($n = 2$ atoms / equivalent set). Note that italicised T in the t^Y column designates translations, while the non-italicised T designates the degeneracy of a particular symmetry species..... 58

Table 4.3.1.8. Correlation between the C_{3v} site group and the O_h factor group for the oxygen atoms ($n = 8$ atoms / equivalent set). Note that italicised T in the t^y column designates translations, while the non-italicised T designates the degeneracy of a particular symmetry species.....	59
Table 4.3.2.1. The Raman, infrared and inactive modes of a single graphite crystal as compiled from the literature.....	63
Table 5.2.1.1. Summary of the ancient yellow pigments and some of the Raman band assignments (adapted from Clark ³).....	85
Table 5.2.1.1.1. XRD results for synthesised samples, labelled from (a) to (e) according to the ratio of Pb to Sn to Sb (Pb:Sn:Sb).....	88
Table 6.2.3.4. Peak maximum as obtained from the deconvolution process of the glaze spectra for the various blue and white samples and the calculated index of polymerisation (I_p). The νQ_n values are indicated in cm^{-1}	120
Table 6.2.3.3. Glaze thicknesses of the samples studied as determined by direct measurement using a ruler and by approximate location of the ceramic/glaze interface using a laser beam.....	123

Chapter 1

Introduction

1.1 Background

A new interest in the applications of natural science in an interdisciplinary approach to art and archaeology has prompted the need to look at routine spectroscopic methods that will assist in the study of archaeological samples for identification of underglaze pigments. The results from these studies can be contrasted with those from museum pieces for classification and comparison. These museum pieces are more often than not irreplaceable and therefore necessitate the application of non-destructive methods of analysis to preserve the integrity of these artifacts. The types of art artifacts, among other archaeologically important ones, are paintings, frescoes, paper, leather and – the most resilient artifact that can survive hundreds of years buried in earth and water – porcelain. In recent years there has been a flurry of research activity around the world in various laboratories in search of the most suitable analytical technique, either destructive or non-destructive. Among these are particle-induced X-ray emission (PIXE),¹⁻³ X-ray powder diffraction, inductively coupled plasma (ICP), optical spectroscopy, atomic absorption spectroscopy (AAS), scanning electron microscopy (SEM)^{4,5} and vibrational spectroscopic techniques such as infrared and Raman spectroscopy.^{6,7} Although Raman spectroscopy was used to study a number of artifacts, some of which were of archaeological origin, a consistent non-destructive method as applied to the study of underglaze pigments on glazed porcelain was not established. Indeed, Raman spectroscopy was tried for this purpose in other laboratories but due to the high fluorescence emanating from the glaze, it was thought unsuitable for studying underglaze pigments on glazed porcelain.^{8,9}

1.2 Statement of the problem

While Raman spectroscopy had been widely used to characterise the glaze on glazed ceramic shards and intact artifacts,¹⁰⁻¹⁵ the ceramic body of broken shards, as well as pigments on broken shards, it had not been successfully used to study underglaze pigments through the glaze on glazed porcelain artifacts (intact or broken shards). However, it had been tried and the frustrations that resulted from repeated attempts to study underglaze pigments on glazed ceramic artifacts non-destructively through the glaze are illustrated by the following excerpts:

“... However, the glaze on shards constitute an impediment to analysis by Raman microscopy; such samples were placed for analysis on the XY translation stage of the microscope using a holder which permitted adjustments by rotation about an axis perpendicular to the light beam. In this way the cross-sections of the glazed shards, i.e. the broken edges, could be studied by looking at the coloured layer coating the ceramic material ...”^{8,9}

*“... The major problem which seems to prevent the successful recording of the Raman spectra of underglaze pigments through the glaze itself is the fluorescence under visible excitation ...”*¹⁰

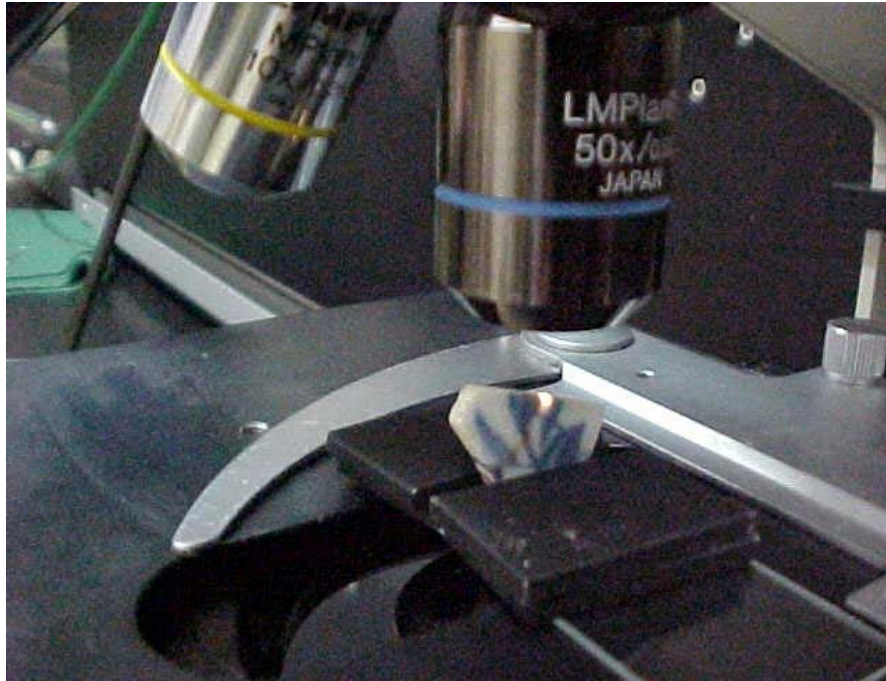


Figure 1.2.1. Due to the inability of researchers to access the pigment of glazed artifacts through the glaze, a shard was often placed in the position shown above in order to access the underglaze pigment on glazed artifacts. This effectively ruled out studies on intact museum pieces where the pigment is not exposed to the surface

Due to the problem presented by the high fluorescence emanating from the glaze of glazed porcelain artifacts, the following solution was developed:

1. Study underglaze pigments on glazed ceramic artifacts on broken edges (as illustrated in Figure 1.2.1.).
2. Study underglaze pigments through the glaze by looking at the influence of fluorescence as impediment.
3. Attempt to extend these methods and present them as routine methods in studying underglaze pigments on glazed porcelain artifacts, both on

broken shards and on intact porcelain artifacts where the pigment is not exposed to the surface for direct study.

4. The result should be applicable to archaeology in order to facilitate the comparison of excavated shards with intact museum pieces on which the pigment is not exposed to the surface for direct study.
5. The results thus obtained should also facilitate the classification and/or identification of the excavated shards in order to assist the archaeologist in correctly identifying and dating the artifact, thereby adding value to the interpretation of findings from historical sites. In some cases the characterisation should be usable in the restoration and preservation of artifacts where applicable.

1.3. Fluorescence: Impediments to the study of underglaze pigments

Fluorescence in Raman spectroscopy as applied to the study of glazed ceramic artifacts greatly affects the spectral assignment because it can mask spectra collected from the glaze and/or pigments in the sample. In the case of glazed ceramic artifacts, the fluorescence emanates from the glaze of the artifact and is attributed largely to the presence of impurities¹⁴ and to the degree of porosity of the glaze under study.¹⁵

Since the use of a con-focal set-up in Raman microscopy ensures that mainly the spectrum from the focus point is obtained,¹⁶⁻¹⁸ the collection of scattered radiation from volumes in orders of magnitude less than one cubic micron ($\leq 1 \mu\text{m}^3$) at the focus point allows high spatial resolution at high spectral resolution ($\leq 1 \mu\text{m}$)¹⁹ which can be used to access interfacial pigment spectra from the ceramic/glaze interface. However, this technique has not seriously been attempted as shown by the available literature. The interfacial ceramic/glaze region is usually composed of decorative

pigments and other colouring agents which are the main target for study if one is to identify and characterise these pigments through the intervening glaze.^{17,18}

1.4. Pigment characterisation

Although the method of accessing pigment spectra from the interfacial (ceramic/glaze) region is the first step, the ability to characterise and correctly identify the resulting spectra is equally important.

The use of pigments on ceramic artifacts in both art and archaeology can be traced back to antiquity.¹⁹ As such the characterisation of these pigments is of major significance in art analysis and can be used for dating, authenticating and restoring works of art and other historically important artifacts.¹⁹ The pigments are usually made up of natural and/or synthetic pigments whose exact chemical composition and degradation products can assist in deciding on the conservation methods to be used.²⁰ It is also useful to determine cut-off dates for the manufactured pigments on artifacts by determining the date of first use (or manufacture) of the pigments found on the artifacts,²¹ if this can be established. Issues of authentication can often be resolved on the basis of knowledge of the methods used by the manufacturers of the artifacts in comparison with the artifact in question.¹⁷ In some instances, knowledge of pigments that are no longer in use is rediscovered.²²⁻²⁶

As a further tool in the process of pigment characterisation, pigments are often synthesised in the laboratory for comparison with pigments on archaeological artifacts for positive identification. The specificity of the Raman signal, which comes from the fact that Raman scattering is a function of the three-dimensional location of atoms in space relative to each other in the scattering medium, makes it possible to consider the Raman signal as a “fingerprint” technique for comparison and/or identification with synthesised pigments. One should always be aware, however,

that the environment in which these pigments are located can also change the Raman spectrum. For instance, cobalt blue on the shards as compared with an isolated pigment shows two different spectra that could be due to stresses in the ceramic/glaze interface and experiments have shown that the physico-chemical environment of this pigment can change the peak intensities.²⁷

To this end, a number of pigment databases²⁸⁻³¹ are available for the purposes of comparing spectra from various samples and thereby aid in pigment identification. Reviews have also been published in which emphasis is placed on the publication of extensive pigment spectra for reference purposes. The work of Clark and co-workers aptly fits this description.³²⁻³³ It is therefore not necessary in all instances to synthesise pigments in the laboratory for purposes of positive identification.

1.5. Glaze characterisation

An attempt to collect the Raman scattered radiation from the glaze necessitates a knowledge of the glaze through which this signal is to be collected. This, in turn, may assist in generalising the methods to be used for the various types of glaze, based on composition, sintering temperature (glaze/glass transition temperature at the time of manufacture) and other properties, including the microstructure of the glaze, such as its porosity which, in turn, may contribute to the opacity of the glaze.

1.5.1. Glaze type and composition

The predominant glaze type is based on a silicate (SiO_4) network, with various compounds interspersed throughout this network in various patterns of concentration and distribution. This allows further classification based on how much these elements break or strengthen this silicate network.

The second type of glaze is also composed of a silicate network but with a predominant amount of SnO₂ usually added as an opacifier. This type is expected to affect either the scattered radiation from the ceramic/glaze interface or the incident beam into the sample to the ceramic/glaze interfacial region.

1.5.2. Glaze transition temperature

Due to the strengthening and weakening of the glaze silicate network as a result of the various compounds (network formers (Si and Al oxides) and network breakers or flux (Na, K, Ca, Pb oxides)),^{34,35} it is possible to determine the approximate glass transition temperature at the time of manufacture and thereby not only determine the level of technology of the manufacturers,³⁶ but also compare the various archaeological samples with museum pieces for possible similarity of place of origin^{14,17,36} or method of manufacture. Comment on the generality of obtaining spectra through such a glaze from the ceramic/glaze interface can also be made by considering the intensity of fluorescence from the glaze.

1.5.3. Glaze microstructure

Since fluorescence is also a function of the general porosity of the glaze,¹ the microstructure of the glaze should also be an indicator of the success or failure of any method that will attempt to direct a beam through a highly refractive and porous glaze to the ceramic/glaze interface. Comment on the porosity of the samples will therefore add immense value to these discussions.

1.6. Conclusion

The intention in Chapter 1 was to give an overview of and background information on the prevailing situation with regard to the stated problem and the solution being sought.

In summary therefore, it became clear that despite the simplified definition of the problem, the field of archaeology has had limited tools at its disposal without an accurate non-destructive method of characterising underglaze pigments on intact ceramic pieces.

Therefore, a non-destructive method of analysis needed to be devised to unlock the vast body of information buried in these artifacts by identifying the underglaze pigments through the glaze. This will open a new chapter in archaeological research.

1.7. References

1. Cheng, H.S., Zhang, Z.Q., Xia, H.N. and Yang F.J. *Nucl. Instrum. Meth.* 2002, B **190**, 488.
2. Cheng, H.S., Zhang Z.Q., Zhang, B. and Yang, F.J. *Nucl. Instrum. Meth.* 2004, B **219**, 16.
3. Lin, E.K., Yu, Y.C., Wang, C.W., Liu, T.Y., Wu, C.M., Chen, K.M. and Lin, S.S. *Nucl. Instrum. Meth.* 1999, **150**, 581.
4. Padeletti, G. and Fermo, P. *Appl. Phys. A: Mater. Sci. Process.* 2003, **77(1)**, 125.
5. Best, S.P. and Clark, R.J.H. *Endeavour.* 1993, **16**, 66.
6. Davey, R., Gordimer, D.J., Singer, B.W. and Spokes, M.J. *J. Raman Spectrosc.* 1994, **25**, 53.
7. Sato, R.K. and McMillan, P.F. *J. Phys. Chem.* 1987, **91**, 3494.
8. Clark, R.J.H. and Curri, L.M. *J. Mol. Struc.* 1998, **440**, 105.
9. Clark, R.J.H. and Gibbs, P.J. *J. Raman Spectrosc.* 1997, **28**, 99.
10. Brooke, C.J., Edwards, H.G.M. and Tait, J.K.F. *J. Raman Spectrosc.* 1999, **30**, 429.
11. Colombari, P. *Appl. Phys. A.* 2004, **79**, 167.
12. Welter, N., Schüssler, U. and Kiefer, W. *J. Raman Spectrosc.* 2007, **38**, 113.
13. Colombari, P., Etcheverry, M-P., Asquier, M., Bounichou, M. and Tounié A. *J. Raman Spectrosc.* 2006, **37**, 614.
14. Osticioli, I., Zoppi, A. and Castellucci, M. *J. Raman Spectrosc.* 2006, **37**, 974.
15. Colombari, P. *Mater. Res. Soc. Symp. Proc.* 2005, **852E**, 008.3.1.
16. Huang, P.V. *Vibrational Spectrosc.* 1996, **11**, 17.
17. Kock, L.D. and de Waal, D. *J. Raman Spectrosc.* 2007, **38**, 1480.

18. Kock, L.D. and de Waal, D. *Spectrochim. Acta. A.* 2008, **71**, 1348.
19. Colombari, P., Sagon, G. and Faurel, X. *J. Raman Spectrosc.* 2001, **32**, 351.
20. Colombari, P., Milande, V. and Le Bihan, L. *J Raman Spectrosc.* 2004, **55**, 527.
21. Hwa, L-G., Hwang, S-L. and Liu, L-C. *J. Non-crystalline Solids.* 1998, **238**, 193.
22. Turner, W.E.S. and Rooksby, H.P. *Glastechnische B.* 1959, **32**, 17.
23. Roy, A. and Berrie, B.H. In: *New Lead-based Yellow in the Seventeenth Century; Painting Technique: History, Materials and Studio Practise.* International Institute for Conservation of Historic and Artistic Works. Roy, A. and Smith, P. (Eds), 1998, p 160.
24. Ravaut, E., Rioux, J-P. and Loire, S. *Techne.* 1998, **7**, 99.
25. Dik, J., Hermeus, E., Perchar, R. and Schenk, H. *Archaeometry.* 2005, **47**, 593.
26. Burgio, L., Clark, R.J.H. and Theodoraki, K. *Spectrochimica Acta A.* 2003, **59**, 2371.
27. Colombari, P., Robert, I., Roche, C., Sagon, G. and Milande, V. *Rev. Archeometrie.* 2004, **28**, 153.
28. www.chem.ucl.ac.uk/resources/raman/; accessed: January 2008.
29. www.minerals.caltech.edu/files/raman/; accessed: January 2008.
30. www.rruff.geo.arizona.edu/rruff/; accessed: January 2008.
31. www.ens-lyon.fr/LST/Raman/index.php; accessed: January 2008.
32. Correia, A.M., Clark, R.J.H., Ribeiro, M.I.M. and Duarte, L.T.S. *J. Raman Spectrosc.* 2007, **38**, 1390.
33. Clark, R.J.H. *C.R. Chimie.* 2002, **5**, 7.
34. Colombari, P. *J. Non-Cryst. Solids.* 2003, **323**, 180.

University of Pretoria etd – Kock, L.D. (2009)

35. Colombari, P., de Laveaucoupet, R. and Milandé, V. *J. Raman Spectrosc.* 2005, **36**, 857.
36. Ricciardi, P., Colombari, P. and Milandé, V. *J. Raman Spectrosc.* 2008, **39**, 1113.

CHAPTER 2

Literature review

The literature on the technique of Raman spectroscopy and its various applications since the advent of coherent lasers is extensive. However, applications of Raman spectroscopy to ceramic artifacts, including those of archaeological origin is relatively recent. Indeed, some of the earlier work on the characterisation of ceramic artifacts was not done through the application of Raman spectroscopy at all. Several other techniques, ranging from particle-induced X-ray emission (PIXE),¹⁻⁵ which is an elemental analysis technique, have been used to identify fake porcelain.² PIXE has also been used in the elemental characterisation of glass, ancient pottery and porcelain of archaeological origin.^{3,6} Although non-destructive, especially in the study of precious artifacts, PIXE was nevertheless deemed to be of limited use with regard to molecular recognition. The obvious limitation of looking only at ratios of elements in an artifact is that one would be unable to distinguish among rutile (TiO₂), Brookite (TiO₂) and anatase (TiO₂)⁷ – information that is very important in determining, among others, the possible sintering temperatures of the artifact in question.

Other techniques, such as X-ray diffraction, inductively coupled plasma (ICP) and scanning electron microscopy (SEM),^{8,9} have also been used in art analysis. Raman spectroscopy, in particular micro-Raman spectroscopy, where a microscope is coupled to the conventional Raman instrument, presents some very useful advantages over elemental techniques⁹ and as a result it emerged as the technique of choice for art analysis in general and archaeological artifacts in particular. This characterisation includes looking at pigments on or beneath the glaze of ceramic artifacts of historical importance¹⁰⁻¹³ and, in some instances, has been extended to the study of glaze¹⁴ and the ceramic body itself, beginning with ancient unglazed

pottery¹⁵ and ancient glazed Vietnamese porcelain¹⁶ and extending to glazed Chinese Ming porcelain.¹⁷

In an attempt to build a coherent picture of the vast applications of this technique in art analysis, P. Vandenaabeele¹⁸ presented a broad picture of an interdisciplinary group of disciplines from which art is currently drawing benefits.

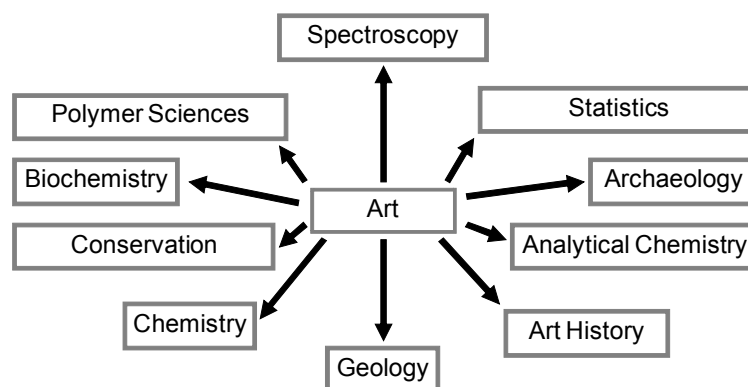


Figure 2.1. Diagram showing the interdisciplinary nature of art analysis and how it relates to a number of research fields (adapted and modified from Vandenaabeele¹⁸)

2.1. Studies of glazed blue and white porcelain

In the case of studies of glazed blue and white porcelain, the work of Colomban and co-workers with regard to micro-Raman applications in studying precious ancient glasses, glazes and glass beads using portable and non-portable instruments generated excellent Raman fingerprint spectra of crystalline and glassy phases.¹⁹⁻²² The portable instruments in some instances produced good results albeit with

difficulty, while laboratory instruments produced excellent results in general. More importantly, however, this work provided information that allowed the researchers to determine the origin and possible date of manufacture of these artifacts where this was in question.

The work of Clark and co-workers, on the other hand, concentrated on ancient pigments (largely inorganic in nature) and their characterisation and identification.²³⁻²⁶ Many researchers, especially in the early applications of the Raman technique to ceramic artifacts, also reported ceramic body studies together with glaze and/or pigment studies in order to build a coherent picture of the artifact. Examples of these studies include the work of Colomban and his co-workers on Vietnamese blue and white ancient Tham Thai porcelain,^{16,19,27,28} as well as the earliest known Meissen porcelain and stoneware.²² This work also includes studies of ancient Vietnamese porcelain and celadon glazes²⁹ by these same authors.

Studies by Edwards and co-workers on a porcelain plaque-mounted table³⁰ and glazed roof tiles³¹ can also be considered as examples of the characterisation of ancient ceramics. Several workers in other laboratories have also contributed to this field, including the work of Vandenabeele and co-workers on porcelain cards.³² Indeed, these authors contributed extensively to the analysis of artifacts using Raman spectroscopy.³³⁻³⁵ In this section, the literature associated with studies of blue and white porcelain will be reviewed and segmented into three subsections dealing with glaze, pigment and porcelain body, in that order. The emphasis on blue and white is due to the fact that most of the shards in this study are blue and white. There is, however, a tile shard with yellow pigments that has also been included in the study due to differences in glaze type with the blue and white samples.

2.1.1. Glaze composition studies

The literature on glaze composition studies of ceramic artifacts using Raman spectroscopy is new and limited. The glaze on blue and white porcelain shows broad bands around 500 cm^{-1} and 1000 cm^{-1} as reported by Colomban and Treppoz.^{36,37} These broad Raman bands are due to the predominance of silicate structure in these types of glaze.³⁸ However, it was not until recently that Colomban and co-workers developed a method to extract composition information from these broad Raman bands.^{39,40}

This method has since been successfully applied to a number of glaze types and also proved useful in not only determining composition, but also processing the temperature of the artifacts at the time of manufacture.^{41,42} The composition information on the artifacts has led to the determination of the manufacturing location,⁴²⁻⁴⁴ thus assisting historians and archaeologists in recognising the manufacturing patterns of specific locations.^{43,44} Iron Age trade patterns have been studied based on the application of this method to glass beads discovered at archaeological sites in South Africa.⁴⁴

2.1.2. Pigment analysis studies

Throughout the centuries, pigments of various kinds have been used in the decoration of porcelain. With regard to blue and white porcelain artifacts, the most common pigment giving the blue colour is cobalt blue.⁴⁵ However, other rare inorganic pigments have been identified on ancient porcelain.⁴⁶ Examples of these include lapis lazuli or lazurite ($\text{Na}_8[\text{Al}_6\text{Si}_6\text{O}_{24}]\text{S}_n$) in 13th century ceramics⁴⁶ and more specifically on an Iranian ewer vessel of the 13th century.⁴⁷ This pigment was also used in place of the more common cobalt blue on medieval ceramic artifacts from Italy,^{48,49} indicating that the blue appearance of archaeological artifacts alone should

not be used to classify these artifacts. Indeed, some researchers contend that lapis lazuli was first used as a pigment as early as 920 AD.⁵⁰ Even further back in history, before 3000 BC in Egypt, one finds the use of another blue pigment, called Egyptian blue ($\text{CaCuSi}_4\text{O}_{10}$), known as “the colour of the eternal sky”, which was used to decorate the bust of queen Nefertete who lived during the reign of Pharaoh Akhenaten in Egypt.⁵¹⁻⁵⁴ The barium analogue of Egyptian blue, called Han blue ($\text{BaCuSi}_4\text{O}_{10}$), has also been identified on painted pottery figurines found in Chinese tombs dating from about 1900 years ago.⁵⁵ With this in mind, it becomes even more important to identify and characterise correctly any blue pigment found on blue and white ceramic artifacts of archaeological origin.

The literature on blue pigment analysis also places emphasis on the hue of the blue underglaze pigment; it has been shown that the hue of Ming porcelain blue pigment was governed by the amount of manganese added.⁵⁵ In some unknown archaeological porcelain samples, however, Raman spectroscopy was used to confirm that amorphous carbon had been added to darken the blue cobalt aluminium oxide.⁵⁶ The colour of the blue pigment in the case of the synthesised cobalt blue can also be varied from blue to green by modifying the Co:Al ratio, thereby producing various inverse spinels.⁵⁷

In all these studies involving various types of blue pigment, cobalt blue is the most common pigment responsible for the blue colour and it is clearly distinguishable from the rest by its Raman fingerprint owing to the structure specificity of the Raman technique. Despite this, it was not until recently⁵⁸ that its Raman signature on porcelain was recorded and identified.

2.1.3 Porcelain body studies

It is said that long before high-temperature fired Chinese blue and white (transparent) glazed porcelain became popular in Europe, white translucent famous porcelain artifacts had already been produced by Iznik Ottomans.⁵⁹ Indeed, the work of Kiefer⁶⁰⁻⁶² is well known in this regard. This work was further complemented by Henderson,⁶³ and it was only recently that Colomban and co-workers⁶⁴ showed that the white colour of these artifacts actually comes from the α -quartz-rich slip deposited just below the glaze to hide or mask the body which was usually pink/yellowish, as was the case with early Vietnamese porcelain stoneware.^{64,65} Colomban and co-workers also showed that the Raman band centre of 500 cm^{-1} related to the lateral displacement of the bridging oxygen (Si-O-Si), whereas the 1000 cm^{-1} Raman band is related to the stretching oxygen (Si-O) vibration. The occurrence of the bands depends on the type of ceramic.^{38,66} The Colomban group also identified correlations between processing temperature and raw materials, and these correlations became helpful in using Raman spectroscopy in the study of processing temperature and the material composition of glazes and glass structures. Although the literature on Raman spectroscopy studies of porcelain body composition is very small, detailed Raman spectroscopic studies have been performed on Vietnamese proto porcelain and celadons of the 13th to 16th century⁶⁷ and also for the dating of excavated Vietnamese shards and celadons,⁶⁸ with good results.

2.2 Pigment analysis on glazed tiles

Glazed tiles are another group of artifacts of historical and archaeological interest. In 1999 post-medieval glazed tiles from Bottesford in Leicestershire, UK, were studied using Fourier Transform (FT) Raman spectroscopy for the first time.³¹ Studies on the Bottesford tiles showed that, to a limited extent, some Raman

pigment signature could be obtained through the tile glaze using near-infrared excitation and that fluorescence under visible excitation prevented successful recording of spectra.³¹

Other studies of similar artifacts using Raman spectroscopy include 19th century porcelain cards³² and an English soft-paste porcelain plaque-mounted table.³⁰ In both these studies, the pigments that were used for decoration were successfully characterised, except in the case of the blue pigment on the porcelain plaque-mounted table.³⁰

2.3. Conclusion

The literature reviewed in this chapter basically shows that the application of Raman spectroscopy in art and archaeology is a very recent field of research. Micro-Raman spectroscopic applications show enormous promise in the study of ceramic/glaze interfacial pigments on porcelain and tiles of archaeological origin. The even narrower subset of this field dealing with applications on blue and white ceramic artifacts of historical and archaeological interest has just begun. Most of the literature is primarily publications of the proof-of-concept type seeking to demonstrate the applicability of Raman spectroscopy in the study of various materials and artifacts. This has been done successfully throughout the literature and the following advantages have been demonstrated:

1. High reproducibility of the Raman spectra
2. High sensitivity (even micro-grains can be studied)
3. Non-destructive (especially important for precious museum artifacts)
4. In situ applications (no sample preparation required)
5. High spatial resolution ($\leq 1 \mu\text{m}^3$)
6. High spectral resolution ($\leq 1 \text{ cm}^{-1}$)

7. Crystalline and amorphous materials of any colour may be studied

The literature reviewed in this chapter therefore shows a wide area of research opportunity that still remains to be explored, while giving a concise picture of what has already been achieved in the field of Raman spectroscopic studies on blue and white ceramic artifacts of archaeological origin.

2.4 References

1. Cheng, H.S., Zhang, Z.Q., Xia, H.N. and Yang, F.J. *Nucl. Instr. and Meth.* 2002, **B190**, 488.
2. Cheng, H.S., Zhang, Z.Q., Zhang, B. and Yang, F.J. *Nucl. Instr. and Meth.* 2004, **B219**, 16.
3. Cheng, H.S., He, W.Q., Tang, J.Y., Yang, F.J. and Wang, J.H. *Nucl. Instr. and Meth.* 1996, **B118**, 377.
4. Johansson, T.B., Akelsson, R. and Johansson, S.A.E. *Nucl. Instr. and Meth.* 1970, **84**, 141.
5. Johansson, S.A.E. and Johansson, T.B. *Nucl. Instr. and Meth.* 1976, **137**, 473.
6. Gihwala, D., Jacobsson, L., Peisach, M. and Pineda, C.A. *Nucl. Instr. and Meth.* 1984, **B3**, 408.; see also Lin, E.K., Wang, C.W., Yu, Y.C., Lin, T.Y., Tan, T.P., Chiou, J.W. and Chin, J. *J. Phys.* 1997, **35**, 880.
7. Linda C. Prinsloo, L.C., Wood, N., Loubser, M., Sabine, M.C.V. and Tiley S. J. *Raman Spectrosc.* 2004; **35**: 527.
8. Padeletti, G. and Fermo, P. *Appl. Phys. A: Mater. Sci. Process.* 2003, **77(1)**, 125.
9. Best, S.P., Clark, R.J.H. and Withnall, R. *Endeavour.* 1993, **16**, 66.
10. Corset, J., Dhamelin Court, P. and Barbillat, J. *Chem. Br.* 1989, **6**, 12.
11. Clark, R.J.H., Cooksey, C.J., Daniels, M.A.M. and Withnall, R. *Endeavour.* 1993, **17**, 191.
12. Clark, R.J.H. *Proc. Int. Conf. on Raman Spectroscopy*, Hong Kong, New York, Wiley, 1994, p 14.
13. Huang, P. V. *Vibrational Spectrosc.* 1996, **11**, 17.
14. MacMillan, B. and Piriou, J. *J. Non-Cryst. Solids.* 1983, **55**, 221.

15. Zuo, J., Wang, C. and Xu, C. *Spectrosc. Lett.* 1998, **31**, 1431.
16. Liem, N.Q., Sagon, G., Quang, V.X., Tan, H.V. and Colomban, P. *J. Raman Spectrosc.* 2000, **31**, 933.
17. Davey, R., Gordimer, D.J., Singer, B.W. and Spokes, M.J. *J Raman Spectrosc.* 1994, **25**, 5318.
18. Vandenabeele, P. *J. Raman Spectrosc.* 2004, **35**, 607.
19. Colomban, P. *Applied Phys. A: Mater. Sci. Process.* 2004, **79**, 167.
20. Colomban, P., Milande, V. and Le Bihan, L. *J. Raman Spectrosc.* 2004, **35**, 527.
21. Colomban, P., Etcheverry, M-P., Asquier, M., Bounichou, M. and Tournié, A. *J. Raman Spectrosc.* 2006, **37**, 614.
22. Colomban, P. and Milande, V. *J. Raman Spectrosc.* 2006, **37**, 606.
23. Correia, A., Clark, R.J.H., Ribeiro, M.I.M. and Duarte, L.T.S. *J. Raman Spectrosc.* 2006, **38**, 1390.
24. Burgio, L. and Clark, R.J.H. *Spectrochim. Acta. Part A.* 2001, **57**, 1491.
25. Clark, R.J.H., *C.R. Chimie.* 2002, **5**, 7.
26. Clark, R.J.H. *J. Mol. Struct.* 2007, **834**, 74.
27. Colomban, P., Sagon, G., Huy, L.Q., Liem, N.Q. and Mazerolles, L. *Archaeometry.* 2004, **46**, 125.
28. Colomban, P., Sagon, G. and Faurel, X. *J. Raman Spectrosc.* 2001, **32**, 351.
29. Liem, N.Q., Thanh, N.T. and Colomban, P. *J. Raman Spectrosc.* 2002, **33**, 287.
30. Edwards, H.G.M., Colomban, P. and Bowden, B. *J. Raman Spectrosc.* 2004, **35**, 656.
31. Brooke, C.J., Edwards, H.G.M. and Tait, J.K.F. *J. Raman Spectrosc.* 1999, **30**, 429.

32. Vandenabeele, P., De Paepe, P. and Moens, L. *J. Raman Spectrosc.* 2008, **39**, 1099.
33. Vandenabeele, P., Edwards, H.G.M. and Moens, L. *Chem. Rev.* 2007, **3**, 675.
34. Vandenabeele, P. *J. Raman Spectrosc.* 2004, **35**, 607.
35. Vandenabeele, P., Bode, S., Alonso, A. and Moens, L. *Spectrochim. Acta, Part A.* 2005, **61**, 2349.
36. Colombari, P. and Treppozz, F. *J. Raman Spectrosc.* 2001, **32**, 93.
37. Colombari, P. *J. Non-Cryst. Solids.* 2003, **322**, 180.
38. Liem, N.Q., Thanh, H. and Colombari, P. *J. Raman Spectrosc.* 2002, **33**, 287.
39. Colombari, P., March, G., Mazerolles, L., Karmous, T., Ayed, N., Ennabli, A. and Slim, H. *J. Raman Spectrosc.* 2003, **34**, 205.
40. Colombari, P. In: *Raman Spectroscopy in Archaeology and Art History*, Edwards, H.G.M., Charmers, J.M. (eds). Royal Society of Chemistry, Cambridge, 2004.
41. Colombari, P., Milande, V. and Lucas, H. *J. Raman Spectrosc.* 2004, **35**, 68.
42. Colombari, P., Sagon, G. and Faurel, X. *J. Raman Spectrosc.* 2001, **32**, 351.
43. Colombari, P. *J. Raman Spectrosc.* 2003, **34**, 420.
44. Prinsloo, L.C. and Colombari, P. *J. Raman Spectrosc.* 2008, **39**, 79.
45. De Waal, D. *Asian Chem. Lett.* 2004, **8**, 57.
46. Smith, G.D. and Clark, R.J.H. *J. Archaeol. Sci.* 2004, **31**, 137.
47. Colombari, P. *J. Raman Spectrosc.* 2003, **34**, 420.
48. Clark, R.J.H., Curri, L.M., Henshaw, G.S. and Laganara, C. *J. Raman Spectrosc.* 1997, **28**, 105.
49. Clark, R.J.H., Curri, L.M. and Laganara, C. *Spectrochim. Acta.* 1997, **53**, 597.
50. Brown, K.L. and Clark, R.J.H. *J. Raman Spectrosc.* 2004, **35**, 181.

51. Wiedemann, H-G., Arpagaus, E., Müller, D., Marcolli, C., Weigel, S. and Reller, A. *Thermochim. Acta.* 2002, **382**, 239.
52. Iverson, E. *Dan. Hist. Fild. Medd.* 1955, **34**, 3.
53. Wiedemann, H-G. and Bayer, G. *Anal. Chem.* 1982, **54(A)**, 619.
54. Zuo, J., Zhao, X., Wu, R., Du, G., Xu, C. and Wang, C. *J. Raman Spectrosc.* 2003, **34**, 121.
55. Young, W.J. *Far Eastern Ceram. Bull.* 1949, **8**, 20.
56. Kock, L.D. and de Waal, D. *J. Raman Spectrosc.* 2007, **38**, 1480.
57. Mwenesongole, A. MSc Dissertation, University of Pretoria, 2008.
58. De Waal, D. *J. Raman Spectrosc.* 2004, **35**, 646.
59. Colomban, P., Milande, V. and Le Bihan, L. *J. Raman Spectrosc.* 2004, **35**, 527.
60. Kiefer, W. *Cah. Céram.* 1956, **4**, 15.
61. Kiefer, W. *Bull. Soc. Fr. Céram.* 1956, **30**, 3.
62. Kiefer, W. *Bull. Soc. Fr. Céram.* 1956, **31**, 17.
63. Henderson, J. In: *The Pottery of Ottoman Turkey*, Y. Petsopoulos, Y. (ed.), London, Alexandria Press, 1989, p 65.
64. Colomban, P. In: *Arts du Vietnam – La Fleur du Pecher et l'Oiseau d' Azur*, Noppe, C., Hubert, J-F. (eds), Tournai, La Renaissance du Livre, 2002, p 100.
65. Colomban, P., Sagon, G., Louhichi, A., Binous, H. and Ayed, N. *Rev. Archaeom.* 2001, **25**, 101.
66. Liem, N.Q., Sagon, G., Quang, V.X., Tan, H.V. and Colomban, P. *J. Raman Spectrosc.* 2000, **31**, 933.
67. Zuo, J., Xu, C., Wang, C. and Yushi, Z. *J. Raman Spectrosc.* 1999, **30**, 1053.
68. Tri, B.M., Tin, T.T., Liem, N.Q. and Colomban, P. *Taoci.* 2001, **2**, 105.

Chapter 3

Synthesis and analysis techniques

The information that is generally sought from studying archaeological samples requires that these samples be studied non-destructively. For this reason, Raman spectroscopy, for its versatility with regard to the wide spectrum of samples that can be studied without any sample preparation, emerges as the single most desirable technique of choice. However, depending on the nature of the sample, it is usually necessary to employ other complementary techniques in order to verify reference samples and/or for use as control techniques for verification purposes. In this work, powder X-ray diffraction (XRD) and energy dispersive X-ray spectrometry (EDX) were used as complementary techniques to the Raman studies. In the following sections, these techniques are discussed, beginning with Raman spectroscopy, followed by X-ray diffraction and concluding with EDX studies.

3.1 Theory of Raman spectroscopy

The Raman Effect was discovered by C.V. Raman in 1927 and the first publication came by way of a letter submitted by C.V. Raman and K.S. Krishnan in *Nature*, 31 March 1928¹. This discovery was followed by a flurry of papers in which confirmations of Raman's discovery were reported,²⁻⁴ culminating in a review by Pringsheim, in which he labelled Raman's discovery "the Raman Effect".⁵ It was, however, not until 1974 that additional intense Raman scattering from pyridine molecules adsorbed at electrochemically roughened silver electrodes⁶ was reported, thereby setting off the developments of surface-enhanced Raman spectroscopy (SERS), in addition to normal Raman scattering.⁷⁻⁹ Today, more than 27 different effects are known as variants of the Raman Effect.¹⁰ These include, but are not limited to, coherent anti-Stokes Raman spectroscopy (CARS),¹¹ which is well suited

to the study of molecular species in flames, and surface-enhanced resonance Raman scattering (SERRS),¹² a very powerful technique combining the SERS and resonance effects of the Raman technique. There are also novel applications for chiral molecules such as Raman optical activity (ROA),¹³ sensitive enough to discriminate between molecular mirror images.

The Raman Effect is basically a scattering phenomenon. When light (monochromatic) is irradiated onto a molecule, the scattered radiation will have the same frequency as the incident radiation (Rayleigh), but will also be accompanied by frequency-shifted radiation on either side of the incident radiation (Stokes and anti-Stokes). This shifted radiation is unique to the scattering media, being dependent on the molecular or crystal structure of the scattering medium.

It is possible to develop a time-dependent quantum mechanical (semi-classical) description of the Raman Effect by considering the phenomenon as a two-photon process.^{10,14} However, a classical view also predicts the three types of scattered radiation mentioned above (Rayleigh, Stokes and anti-Stokes). By starting with the equation that relates the electric field (\vec{E}) and the induced dipole moment ($\vec{\mu}$) to a first approximation as:

$$\vec{\mu} = \alpha \vec{E} \quad 3.1$$

where α is the polarisability (second-order tensor). Using the classical electric field equation for \vec{E} ,

$$\vec{E} = \vec{E}_0 \sin 2\pi \nu t \quad 3.2$$

where \vec{E}_0 is the incident electric field, ν is the frequency of the field and t is the time defining the evolution of the electric field.

Substituting equation 3.2 into equation 3.1, we obtain the induced dipole moment as a function of the frequency of the incident radiation, ν , and the polarisability, α :

$$\bar{\mu} = \alpha \bar{E}_o \sin 2\pi \nu t \quad 3.3$$

Because the perturbation of the molecular electron cloud depends on the relative position of the atoms, the polarisability is also a function of the relative position of the constituent atoms.¹⁵ Considering the quantisation of molecular vibrational energy levels, similar to electronic energy levels, the vibrational energy of a particular mode may be written as:

$$\bar{E}_v = (j + \frac{1}{2})h\nu_v \quad 3.4$$

where j is the vibrational quantum number ($j = 0, 1, 2, \dots$), ν_v is the frequency of the vibrational mode, and h is the Planck constant. Since the normal coordinate, Q , also varies periodically and is a function of ν_v described in equation 3.4, we can also write

$$Q = Q_o \sin 2\pi \nu_v t \quad 3.6$$

where Q_o is constant. We also know that in general the polarisability α depends on the molecular normal coordinates Q such that

$$\alpha = \alpha_o + \left(\frac{\partial \alpha}{\partial Q} \right) Q + \dots \quad 3.7$$

where α_o is the equilibrium polarisability.

Using equations 3.6 and 3.7 and neglecting the higher-order terms of 3.7, we can write the polarisability α as:

$$\alpha = \alpha_o + \left(\frac{\partial \alpha}{\partial Q} \right) Q_o \sin 2\pi \nu_v t \quad 3.8$$

and subsequently, the induced dipole moment ($\bar{\mu}$) from equation 3.3 becomes:

$$\bar{\mu} = \alpha_o + \left(\frac{\partial \alpha}{\partial Q} \right) Q_o \sin 2\pi \nu_v t \bar{E}_o \sin 2\pi \nu t \quad 3.9$$

Simplifying equation 3.7 and using the trigonometric identity:

$$\sin(2\pi \nu_v t) \sin(2\pi \nu t) = \left\{ \frac{1}{2} \cos(2\pi \nu_v t - 2\pi \nu t) - \cos(2\pi \nu_v t + 2\pi \nu t) \right\} \quad 3.10$$

we obtain an equation that contains the difference and sum of the two frequencies (ν and ν_v) of the incident radiation and that of the normal coordinate vibration of the scattering molecule:

$$\bar{\mu} = \alpha_o \bar{E}_o \sin 2\pi \nu t + \frac{1}{2} \left(\frac{\partial \alpha}{\partial Q} \right) Q_o \bar{E}_o \left\{ \cos 2\pi [\nu - \nu_v] t - \cos 2\pi [\nu + \nu_v] t \right\} \quad 3.11$$

Inspection of equation 3.11 shows that the induced dipole moment, $\bar{\mu}$, varies with three scattered component frequencies:

1. ν The frequency of the incident radiation (Rayleigh scattering)

2. $\nu - \nu_v$ The incident frequency less the frequency of the normal coordinate vibration (Stokes radiation)
3. $\nu + \nu_v$ The incident frequency plus the frequency of the normal coordinate vibration (anti-Stokes radiation)

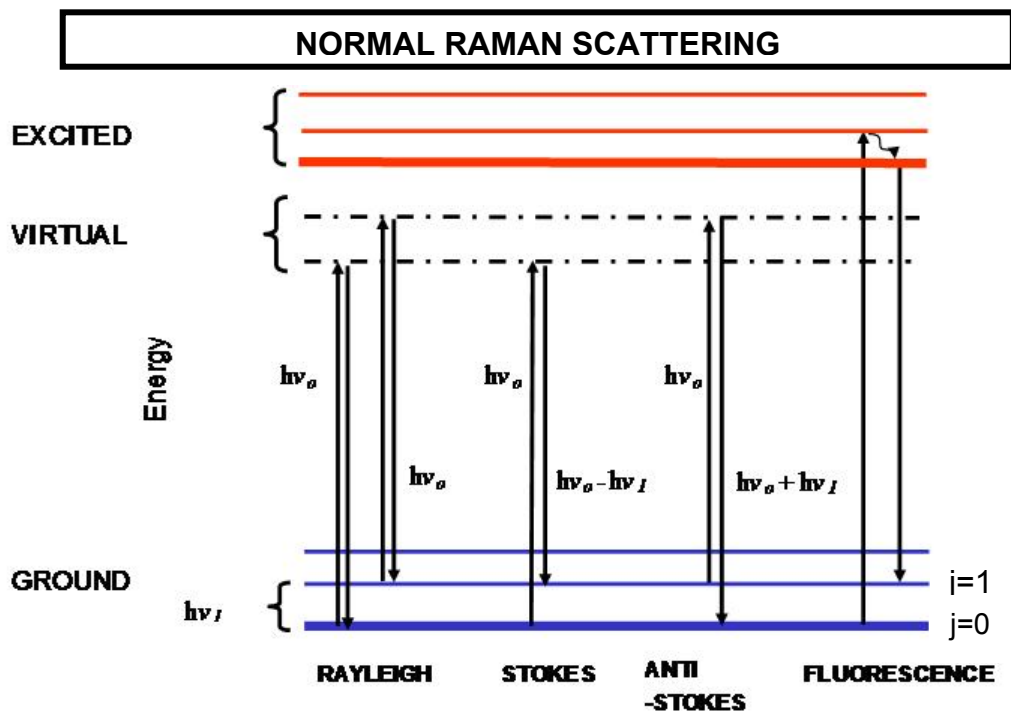


Figure 3.1.1. Illustration of the normal Raman scattering showing Rayleigh, Stokes and anti-Stokes components. The far right depicts fluorescence radiation that, when present, often swamps the Raman signal

Also, looking at equation 3.11, if $\left(\frac{\partial\alpha}{\partial Q}\right)$ is zero and there is no change in the polarisability α with respect to a change in the normal coordinate Q , then there will be no Stokes or anti-Stokes scattering and therefore that particular normal coordinate of vibration will be Raman silent. Clearly, if $\left(\frac{\partial\alpha}{\partial Q}\right) \neq 0$, then the normal coordinate of vibration will be Raman active.

Although the variation of the induced dipole moment with respect to the three types of scattered frequency correctly predicts Rayleigh, Stokes and anti-Stokes radiation, the difference in intensities seen between the Stokes and anti-Stokes radiation emanating from the same normal coordinate of vibration is not predicted by this treatment.

Since the ratio of intensity of the Raman anti-Stokes (L_{AS}) and Stokes (L_S) radiation is predicted to be:

$$\frac{L_{AS}}{L_S} = \left\{ \frac{(\nu_i + \nu_v)}{(\nu_i - \nu_v)} \right\}^4 \exp \left\{ - \left(\frac{h \nu}{kT} \right) \right\} \quad 3.12$$

where ν_i and ν_v are the incident frequency and the frequency of the normal coordinate vibration, respectively, h is Planck's constant, k is the Boltzmann constant and T is the temperature, then the Boltzmann exponential factor in equation 3.12 guarantees that the anti-Stokes radiation intensity is smaller than the Stokes radiation intensity. Hence a weaker signal from the anti-Stokes radiation is observed when measured.

With reference to Figure 3.1.1., the population of molecules in the $j = 0$ (energetically most stable) state is larger than that in the $j = 1$ state. Since the Stokes lines arise from the larger population states ($j = 0$) of the molecules, the Stokes lines are always stronger than the anti-Stokes lines. It is precisely for this reason that, experimentally, we measure the Stokes rather than the anti-Stokes radiation for easier detection and measurement.

3.2. Applications of the techniques used in the study

This section deals primarily with the various experimental applications of techniques that were used in this study. The major technique, Raman spectroscopy, will be explained first, followed by the complementary techniques of XRD and EDX. The synthesis of reference compounds will also be explained in this section, mainly by way of detailed descriptions of synthetic methods, the results of the syntheses and the purposes for which these compounds were synthesised.

3.2.1. Raman experiments

The Raman experiments were carried out with a Dilor XY multi-channel spectrometer equipped with a liquid-nitrogen-cooled charge coupled device (CCD, model 2000) detector. The system was coupled to an Olympus confocal microscope for the micro studies, with a backscattering (180°) configuration¹⁶ as indicated in Figure 3.2.1.1.

Throughout this work, three types of long-focal-length objective lens (10X, 50X and 100X) were used depending on the sample type and the immediate intent. The 10X objective was used for quick testing and viewing of a sample, while the 50X was used for data collection. The third (100X) was used only in cases where a high degree of spatial resolution and particle discrimination were needed, such as for the detection of mullite in powdered ceramic samples.¹⁶

Operating conditions included system calibration on a daily basis using the 520.7 cm^{-1} silicon mode. Work proceeded only if this line was within $\pm 0.5\text{ cm}^{-1}$ of the silicon line. This procedure is particularly important when changes in closely related Raman band positions are to be discerned. In addition, the day-to-day

consistency of results in Raman band positions is guaranteed. This procedure also enables small shifts in a specific Raman band to be identified.

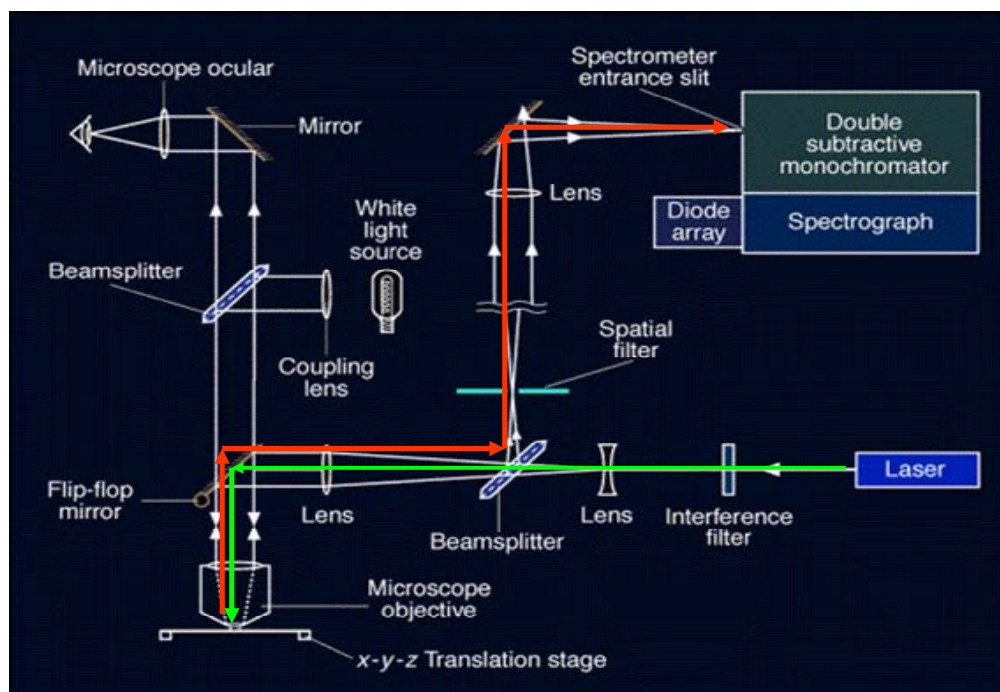


Figure 3.2.1.1. Schematic view of the micro-Raman 180° back-scattering configuration [adapted from: www.ens-lyon.fr/LST/Raman; accessed 20/7/2008]. See also Clark, R.J.H., *C. R. Chimie* 2002, **5**, 7.

The excitation radiation was provided by an Innova 300 Ar⁺ laser operating at 514.5 nm wavelength radiation. A Kr⁺ laser operating at 568.2 nm wavelength radiation was also used for the Citadel tile studies to observe any excitation frequency dependence of the pigments on the tile. The power outputs of these lasers were optimised to suit the sample under study. For the blue shards, typically between 20 and 40 mW was used, depending on the glaze thickness and whether only a surface spectrum or a ceramic/glaze interface spectrum was acquired. Integration times on blue shards, intact plates and the Citadel tile were typically between 120 and 300 seconds, with three accumulations in each spectral window.

Data acquisition and processing were carried out with Labspec[®] software version 3.01 provided by Jobyn Yvon of the Horiba group.¹⁷ An Olympus camera (Model Camedia C7070WZ) mounted on top of the microscope was used to acquire the high-resolution pictures. This camera was mounted with an Olympus NFK eyepiece and all the glaze depth profiles were captured with a 50X objective lens on the microscope.

3.2.2. Powder X-ray diffractometry (XRD)

The basic concept of the origin and application of XRD for characterisation purposes is the diffraction of electromagnetic radiation (X-ray) from crystalline solid materials, thereby yielding a diffraction pattern.¹⁸ The resulting diffraction data are then interpreted for purposes of characterising the diffracting material. In this work the powder XRD technique, in which the diffracting sample is composed of randomly oriented crystalline domains, was used. Figure 3.2.2.1 shows a schematic view of an in-phase scattered beam of X-ray radiation.

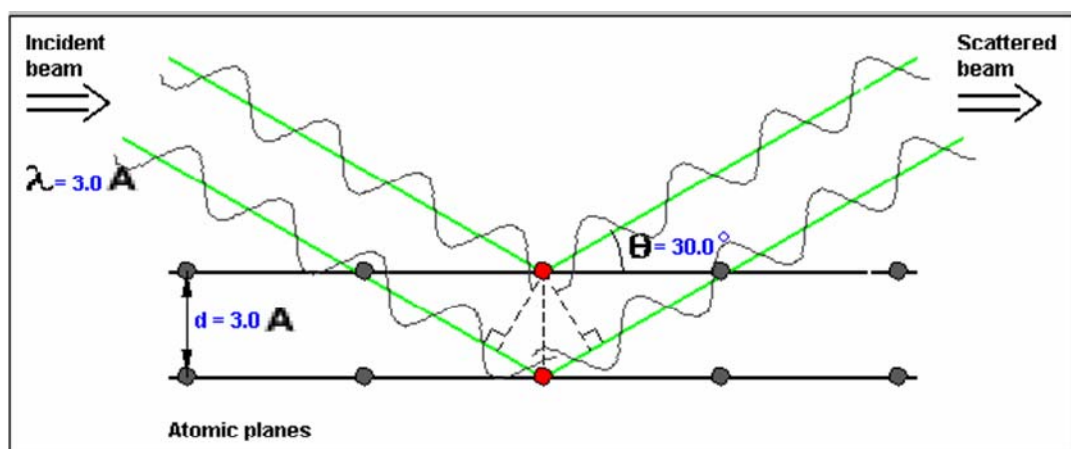


Figure 3.2.2.1. Schematic view of X-ray diffraction from the sample. The scattered radiation contains information on the type and spacing of the atoms in the sample. [adapted from: www.eserc.stonybrook.edu/ProjectJava/Bragg/; accessed 1/4/2009]

This phenomenon, discovered by Sir W.H. Bragg, describes the relationship between the angle, θ , at which a beam of X-rays of wavelength λ can diffract from a crystalline surface given by:

$$2d\sin\theta = n\lambda \quad 3.13$$

where

λ = wavelength of the X-rays

θ = scattering angle of the beam

n = the order of the diffraction peak.

d = atomic inter-plane distance

Since the detected beam is that for which the Bragg condition was met, information on the inter-plane distance can be obtained from X-ray diffraction experiments. This technique has gone through many technical modifications, leading to very accurate material characterisation techniques using modern instrumentation. The technique of X-ray diffraction is widely applied in material characterisation studies.^{19,20} Excellent reviews on X-ray diffraction^{21,22} are also available.

Powder XRD studies were used in this study whenever pigment references were synthesised in order to verify the structure and purity of the synthesised compounds. The results of these studies are discussed in the various subsections under Section 4.3 dealing with each pigment. Table 3.2.2.1 shows the data collection parameters from the instrument that was used in all the work done in these studies (at the University of Pretoria's XRD Laboratory).

Table 3.2.2.1. The Instrument and data collection parameters for the Siemens D 501 XRD instrument that was used to collect XRD data on reference samples are given in this table. The samples were prepared using standard Siemens sample holders and the powder was pressed into the holder using a glass slide

Instrument	Siemens D-501
Radiation	Cu K α (1.5418 D)
Temperature	25 ° C
Specimen	Flat-plate, rotating (30RPM)
Power Setting	40 kV, 40 mA
Monochromator	Secondary, graphite
Detector	Scintillation counter
Range of 2 θ	20-70X10 ²²
Step width	0.04X10 ²²
Time per step	1.5 s

3.2.3. Energy dispersive X-ray spectrometry

EDX was used to obtain elemental ratios on the surface. The depth of penetration of the surface in determining selected element ratios was not more than 20 μm . Various positions were selected per sample in order to obtain representative atom ratios.

A JEOL JSM-5800LV model scanning electron microscope was used for the measurements. Since for these types of study a conductive surface is required, gold sputtering on the surface is usually used in the absence of an ultra-high vacuum. However, in this case, since a high vacuum was used, it was not necessary also to use gold sputtering to provide a conducting medium. The recorded range of

between 1.3 and 1.6 for X^2 square values for all EDX measurements in this study was considered to be within the norm.

3.3. Synthesis of selected reference compounds

The following subsections deal with the synthesis of selected reference compounds. These compounds were selected according to the need for verification purposes and were synthesised according to standard literature methods where available. They were analysed using XRD, EDX and Raman spectroscopy. The results are compared and contrasted with those of the pigments identified on the samples under study for positive sample pigment identification and characterisation.

3.3.1. Cobalt aluminium oxide or cobalt blue (CoAl_2O_4)

Cobalt aluminium oxide was synthesised in a high-temperature furnace (1 400 °C). The method used for this purpose involved using research-grade starting materials (Merck). Two identical samples were treated as follows: cobalt oxide (CoSO_4) was intimately mixed with stoichiometric amounts of $\text{Al}_2(\text{SO}_4)_3$ and dried in the furnace for three hours. The mixture was then fired at 1 000 °C for 24 hours in an alumina crucible.²³ At the end of the 24 hours, the furnace was turned off and one of the samples (Figure 3.3.1.1.(a)) was quenched rapidly, while the other sample (Figure 3.3.1.1.(b)) was left in the furnace and allowed to cool slowly to room temperature in the furnace. Figure 3.3.1.1. shows the Raman spectra of the two cobalt blue samples that were prepared and Figure 3.3.1.2. shows the XRD patterns of the final products.

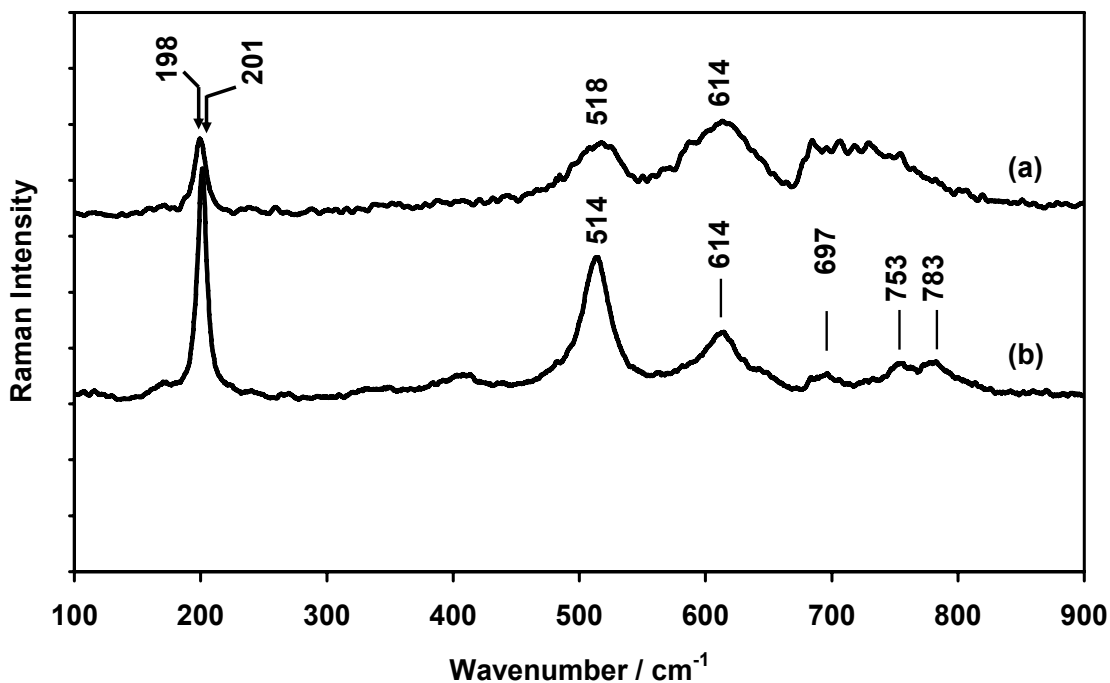


Figure 3.3.1.1. (a-b). Raman spectra of two samples of cobalt blue that were cooled at different rates: (a) cooled slowly and (b) cooled rapidly, at a wavenumber resolution of 2 cm⁻¹.

There seemed to be no difference between the two methods of cooling in the XRD patterns of the cobalt blue samples. However, a slightly less intense Raman band at 198 cm⁻¹ was present for the slowly cooled samples. For the rapidly cooled batch it appears at 201 cm⁻¹.

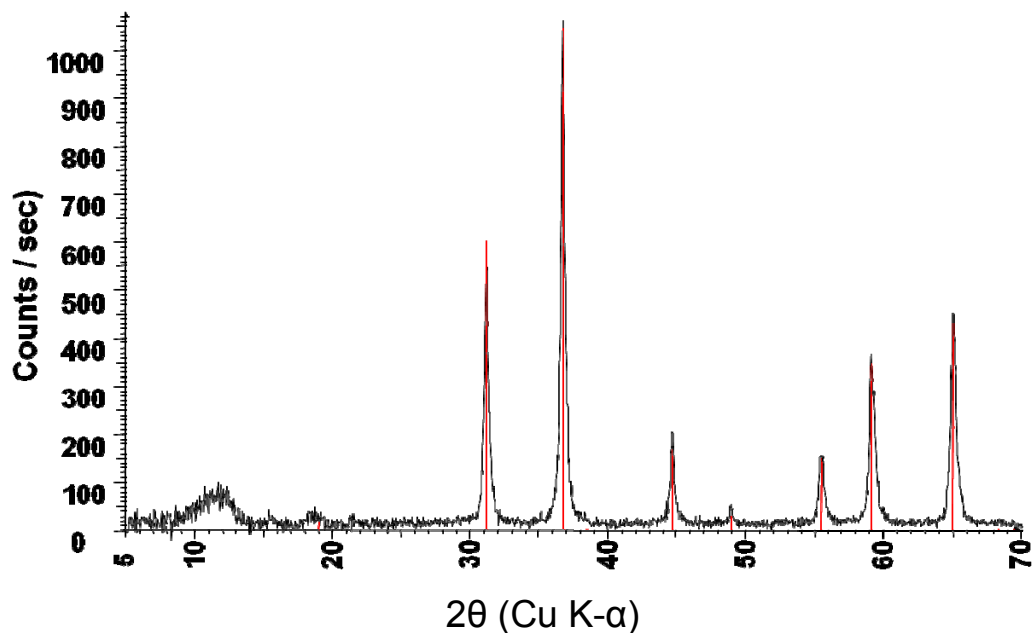


Figure 3.3.1.2. The XRD pattern in this figure is representative of the cobalt blue samples that were cooled rapidly by immediate removal from the furnace.

This same Raman band appears at 195 cm^{-1} on the porcelain shards, which, it is assumed, may have been left in the kiln for slow cooling over several days.²⁴ However, there are still other differences between the cobalt blue on the porcelain shards and the synthesised free pigment. This will be discussed in Section 4.3.1.

3.3.2. Ternary (Pb-Sn-Sb) oxide ($\text{Pb}_2\text{SnSbO}_{6.5}$)

For the preparation of the ternary pyrochlore system, $\text{Pb}_2\text{SnSbO}_{6.5}$, the methods employed by Cascale and co-workers²⁵ were followed as closely as possible. Stoichiometric mixtures of Pb, Sn and Sb in the form of PbO , SnO_2 and Sb_2O_3 obtained from Merck Chemicals²⁶ were thoroughly mixed in an alumina crucible and fired in a high-temperature furnace at a temperature of $900\text{ }^\circ\text{C}$ for 24 hours.

The furnace was then turned off and the products were allowed to cool to room temperature within twenty four hours before XRD and Raman studies could be undertaken. Several samples were prepared in which the ratio Pb:Sn:Sb was varied. Table 3.3.1.2 shows the different samples and the various elemental ratios during preparation.

Table 3.3.2.1. The various samples that were prepared for the purpose of identifying the pigments on the Citadel tile

Sample	(a)	(b)	(c)	(d)	(e)
Pb:Sn:Sb	2:1:1	2:1:2	2:2:1	2:1:0	2:0:1
Ratio		(Excess:Sb)	(Excess:Sn)	(No Sb)	(No Sn)

3.3.3. Preparation of lead (II) stannate (Pb₂SnO₄).

The preparation of lead (II) stannate, or lead tin yellow type II, followed closely that of Clark and co-workers.²⁷ Stoichiometric amounts of Pb₃O₄ and SnO₂ were thoroughly mixed and ground into a fine powder. This mixture was then heated to 900 °C for three hours in a high-temperature furnace and the resulting powder was left to cool in the furnace after the furnace had been switched off. Reaction equation 3.3.3.1. shows the open-air formation of the product:



The solid product in reaction equation 3.3.3.1. was then analysed using powder XRD and the results are shown in Figure 3.3.3.1. The Raman spectrum of lead (II) stannate is shown in Figure 3.3.3.2. The strong Raman band 129 cm⁻¹ and medium

band at 196 cm^{-1} was deemed sufficient to identify this compound as lead (II) stannate, and this is also consistent with literature assignments.^{28,29}

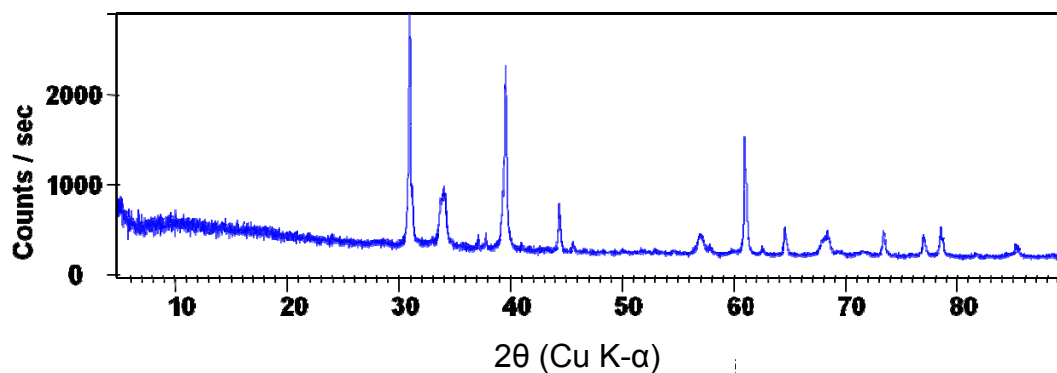


Figure 3.3.3.1. The XRD pattern in this figure is representative of the product in equation 3.1 and has been identified as lead tin yellow type I or lead stannate

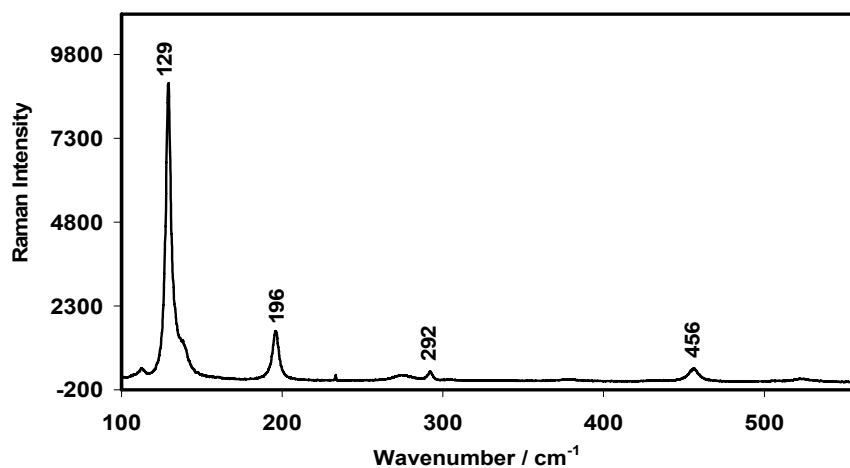


Figure 3.3.3.2. The Raman spectrum of lead (II) stannate (lead tin yellow type I). Incident radiation was 514.5 nm wavelength radiation, with 0.3 mW laser power at the sample. Integration time was 10 seconds and 1 accumulation with wavenumber resolution of 2 cm^{-1}

The results of these analyses were then used in further studies to characterise and identify pigments on the tile shard from the Citadel of Algiers, as discussed in Chapter 5.

3.4. Conclusion

This chapter summarised the techniques that were used in this study (Raman spectroscopy, XRD and EDX). The summary was followed by a description of the synthetic methods that were employed. It was necessary to discuss these aspects in order to clarify the ensuing research, which involved the identification and characterisation of pigments on the blue and white porcelain shards, the intact Ming dynasty plates and the tile shard from the Citadel of Algiers. EDX results for the Citadel tile are discussed in Section 6.2.2.

It is concluded in this chapter that since the field of Raman spectroscopy as applied to samples of archaeological origin is still recent, it is essential that reference compounds are prepared to aid in pigment identification and the building of a coherent body of chemical information for use by archaeologists.

In the case of the blue pigment, differences between porcelain pigment spectra and synthesised references could be investigated as a new line of research. An example would be a detailed study of the structural changes in cobalt blue with changes in pressure, temperature and chemical environment, similar to that found for the ceramic/glaze interfacial region.

The yellow and other pigments on the Citadel tile also presented a unique challenge that required synthesis of reference pigments to aid in the characterization of all the various shades of yellow pigments on the tile. Since the various types of pigments on the tile are lead based, various combinations of Pb,Sn,Sb pigments were

prepared, characterised and comparisons made with results of pigments on the Citadel tile.

3.5 References

1. Raman, C.V. and Krishnan, K.S. *Nature*. 1928, **121**, 501.
2. Rocard, Y. *Comptes Rendus*. 1928, **186**, 1107.
3. Rocard, Y. *Comptes Rendus*. 1928, **186**, 1201.
4. Wood, R.W. *Nature*. 1928, **122**, 349.
5. Pringsheim, P. *Die Naturewissenschaften*. 1928, **16**, 44.
6. Fleischmann, M., Hendra, P.J. and McQuillan, A. *J. Chem. Phys. Lett.* 1974, **26**, 163.
7. Jeanmaire, D.P. and van Duyne, D.P. *J. Electroanal. Chem.* 1977, **84**, 1.
8. Albrecht, M.G. and Creighton, A. *J. Am. Chem. Soc.* 1977, **99**, 5215.
9. Otto, A. In: *Light Scattering in Solids IV*, Cardona, M., Guntherodt, G. (eds), New York, Springer-Verlag, 1984.
10. Long, D.A. *The Raman Effect*. New York, Wiley, 2002.
11. Vestin, F., Afzelius, M., Berger, H., Chaussard, F., Saint-Loup, R. and Bengtsson, P. E. *J. Raman Spectrosc.* 2007, **38**, 963.
12. Carron, K.T. PhD Thesis, Northwestern University, Evanston, Illinois, USA, 1985.
13. Barron, L.D. *Molecular Light Scattering and Optical Activity*, 2nd edition. Cambridge, Cambridge University Press, 2004.
14. Schatz, G.C. and Ratner, M.A. *Quantum Mechanics in Chemistry*. Mineola, New York, Dover Publications, 1993.
15. Colthup, N.B., Daly, L.H. and Wiberley, S.E. *Introduction to Infrared and Raman Spectroscopy*, Academic Press, 1990.
16. Kock, L.D. and de Waal, D. *J. Raman Spectrosc.* 2007, **38**, 1480.

17. Labspec, version 3.01, distributed by Dilor SA and Université de Reims, France, 2004.
18. <http://www.eserc.stonybrook.edu/ProjectJava/Bragg/>; accessed: April 2009.
19. Ristić, M., Ivanda, M., Popović, S. and Musić, S. *J. Non-Cryst. Solids*, 2002, **303**, 270.
20. Yu, K.N., Xiong, Y., Liu, Y. and Xiong, C. *Phys. Rev. B*, 1997, **55**, 2666.
21. Birks, L.S. *X-ray Spectrochemical Analysis*, 2nd edition. New York, Wiley, 1969.
22. Ebsworth, E.A.V., Rankin, D.W.H. and Cradock, S. *Structural Methods in Inorganic Chemistry*. Oxford, Blackwell Scientific, 1987.
23. King, H.P. and Alexander, L.E. *X-ray Diffraction Procedures*, New York, Wiley, 1954.
24. De Waal, D. *Asian Chem. Lett.* 2004, **8**, 57.
25. Young, J.J. *The Ceramic Art: A Compendium of the History and Manufacture of Pottery and Porcelain*. New York, Harper, 1898.
26. Cascales, C., Alonso, J.A. and Rasines, I. *J. Mater. Sci. Lett.* 1986, **5**, 675.
27. Merck Chemicals, Inc. Johannesburg, South Africa.
28. Clark, R.J.H. *C.R. Chimie*. 2002, **5**, 7.
29. Clark, R.J.H., Cridland, L., Kariuki, B.M., Harris, K.D.M. and Withnall, R.J. *J. Chem. Soc. Dalton Trans.* 1995, **2577**.
30. De Faria, D.L.A., Venancio Silva, S. and de Oliveira, M.T. *J. Raman Spectrosc.* 1997, **28**, 873.

Chapter 4

Underglaze pigments on shards and plates

This chapter deals with the study of underglaze pigments on blue and white shards originating from a museum, as well as those excavated in and around the city of Tshwane, South Africa. The museum and excavated shards (of known and unknown origin) are from the National Cultural History Museum (NCHM) of South Africa. Two intact Ming plates provided by the J.A. van Tilburg Museum at the University of Pretoria were also studied for comparison. This chapter concludes by highlighting the major results and the implications of these results for art and archaeological research. Some of the work in this chapter has recently been published in the *Journal of Raman Spectroscopy*.¹

4.1 Glaze depth profiling

The objective was to obtain clear Raman spectra from the ceramic/glaze interfacial region by focusing the laser beam through the glaze for excitation, while collecting the Raman scattered radiation from that interface in the 180° scattering configuration. Since the bulk of the fluorescence emanates from the intervening glaze, the focus point was systematically varied by 4 µm in the vertical axis (Z-axis) starting at the glaze surface, while keeping both the X and Y-axis positions constant and acquiring a spectrum at each position. In this way, a vertical profile of the glaze was generated.¹ Figure 4.1 shows a schematic view of the focus positions for both the glaze surfaces and the ceramic/glaze interface, with the laser powers required for the various thicknesses of the glazes that were studied.

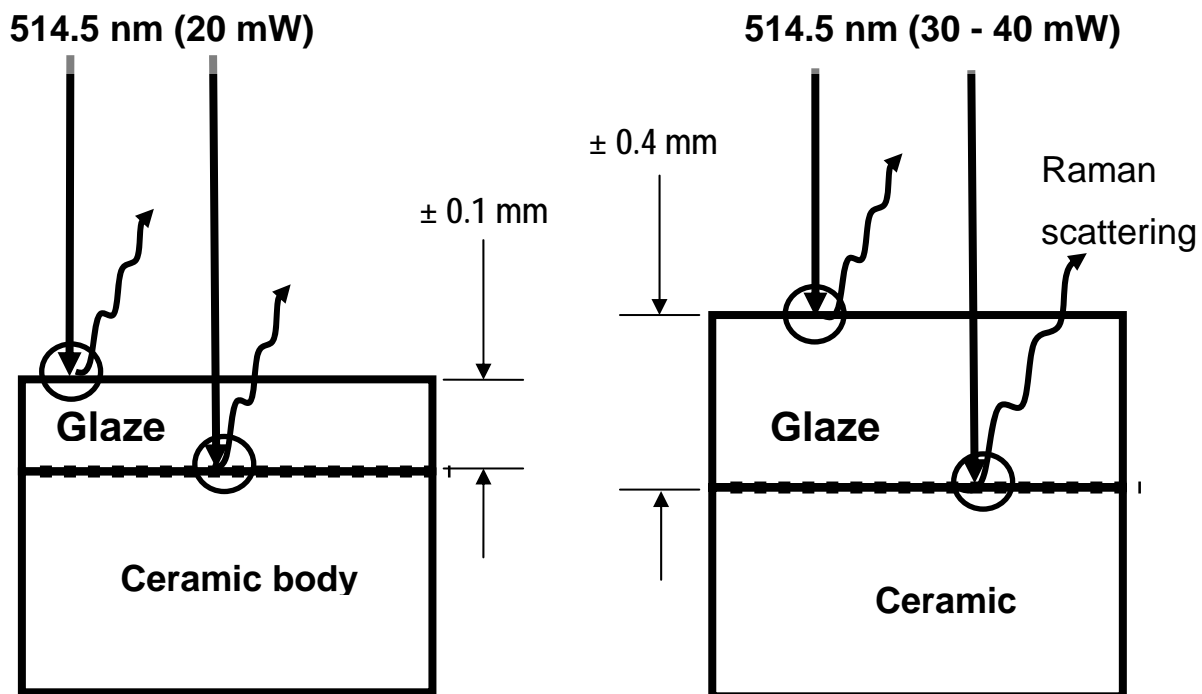


Figure 4.1.1. Schematic view of the focus positions for both the glaze surfaces and the ceramic/glaze interface

Figure 4.1.1 shows that for glaze thicknesses of up to 100 μm , 20 mW was sufficient to obtain ceramic/glaze interfacial spectra, while for thicker glazes of up to 400 μm , higher laser powers (40 mW) were required.

Obtaining spectra through the glaze in this way permits the study of underglaze pigments on intact glazed ceramic artifacts where the pigment is not exposed to the surface for direct study. Figure 4.1.2 shows a typical positioning of an intact museum artifact (in this case a plate) in order to generate a glaze depth profile on an intact museum sample. Figure 4.1.3 shows the first set of samples that were chosen for Raman analysis of underglaze pigments by focusing the excitation radiation through the glaze.



Figure 4.1.2. Typical positioning of a precious porcelain museum piece for glaze depth profile studies using micro-Raman spectroscopy (unknown plate from the J.A. van Tilburg Museum, University of Pretoria)

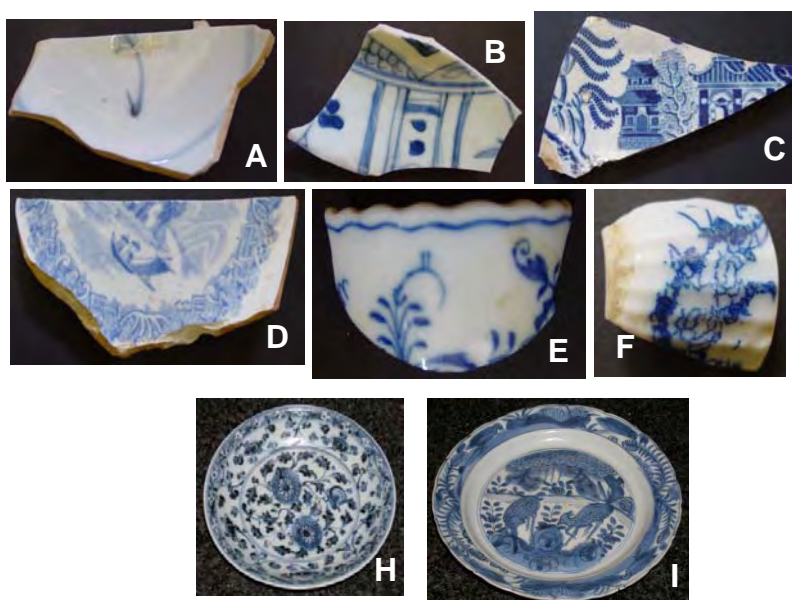


Figure 4.1.3. The set of samples chosen for this study is shown. Samples A and B are of Ming dynasty origin; samples C, D and F are archaeological samples; sample E is of Meissen origin; and samples H and I are intact Ming plates

4.2. Ceramic/glaze interfacial structure

The structure of the ceramic/glaze interfaces is sometimes difficult to characterise by directing the beam at broken surfaces (in the case of broken artifacts) as often the layers are extremely thin and it is therefore difficult to distinguish the order in which the materials were applied on the surface at the time of manufacture, if one can detect them at all. In the case of intact ceramic artifacts where the pigment is not exposed to the surface, this task becomes impossible without going through the glaze using regular techniques. However, using the glaze depth profiling method, one can easily characterise the ceramic/glaze interfacial region. Figure 4.2.1. and Figure 4.2.2.) shows the raw (no filtering or baseline corrections) Raman spectra, illustrating the incremental interval profile needed to characterise the interface.

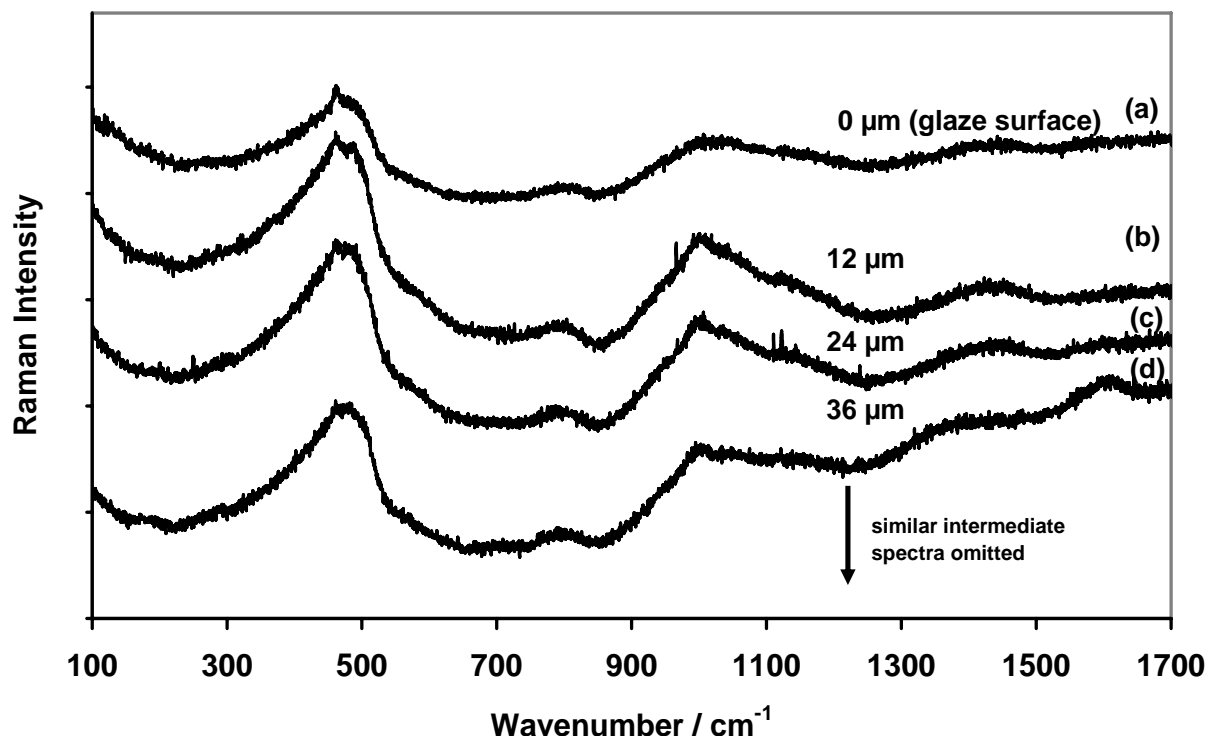


Figure 4.2.1 Typical raw Raman spectra. The surface spectrum in (a) at 0 μm shows only the glaze, while going deeper into the glaze shows a clear pigment spectrum from (f) to (h) as illustrated in Figure 4.2.2. on the following page.

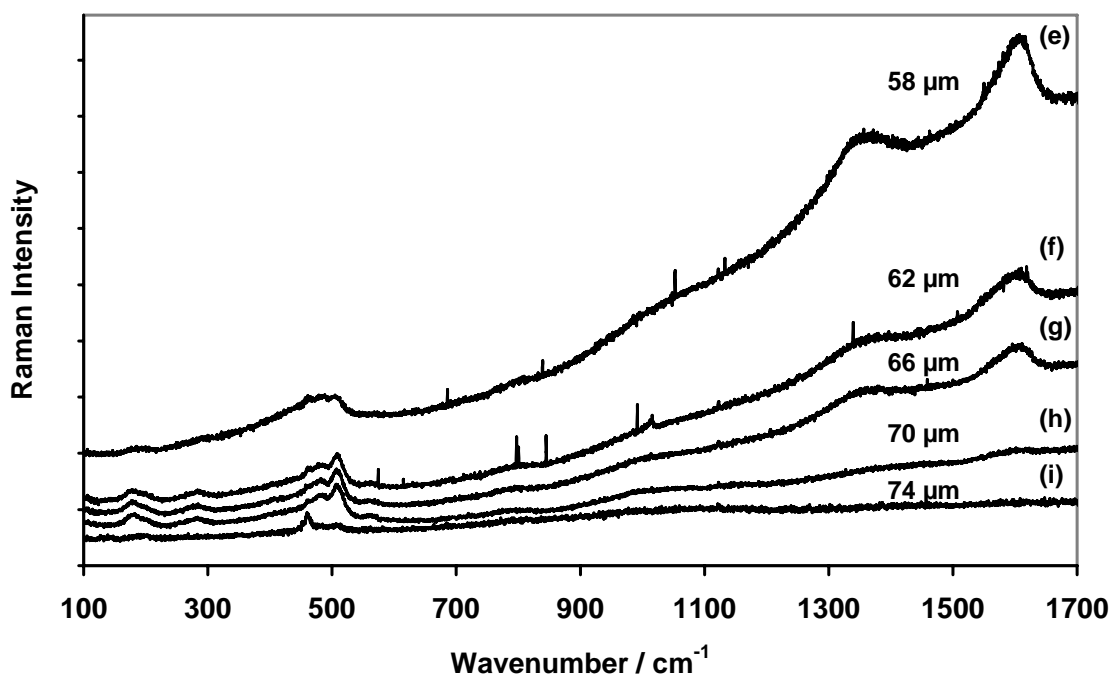


Figure 4.2.2. The spectra from (e) to (i) is a continuation from Figure 4.2.1. This part shows spectra deeper into the glaze from 58 μm to 74 μm at same vertical position. Note the amorphous carbon bands around 1300 and 1600 cm^{-1} from (e) to (g)

From spectra in Figure 4.2.1 and Figure 4.2.2, one can easily construct the structure of the interface. Firstly, the top layer shows the Raman spectra emanating from the glaze [(a) to (d)]. Note that many more spectra collected from the glaze as the interface is approached are not included. Secondly, just as the laser beam strikes the pigment layer [Figure 4.2.2(e) to (h)], strong amorphous carbon bands are observed around 1300 cm^{-1} and 1600 cm^{-1} , indicating a mixture of pigments (cobalt blue and amorphous carbon). As the beam passes the pigment layer and strikes the quartz-dominated ceramic surface, a strong band at 461 cm^{-1} appears. One of the key features of these spectra is the fluorescence intensity that is clearly higher in the glaze layer as well as in this particular pigment layer, but dies off as the laser beam reaches the quartz layer. Figure 4.2.3 illustrates the interfacial structure for this sample (unknown sample C).

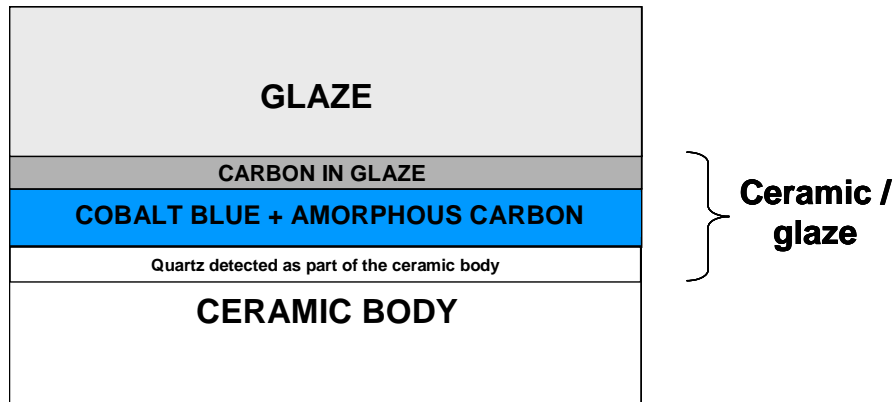


Figure 4.2.3. Schematic view of the ceramic/glaze interfacial region as determined through generating a typical glaze profile with micro-Raman spectroscopy on dark blue sections of sample C (see Figure 4.1.3)

Figure 4.2.4 shows the Raman glaze depth profile from which the schematic view of the ceramic/glaze interfacial region in Figure 4.2.5 was generated.

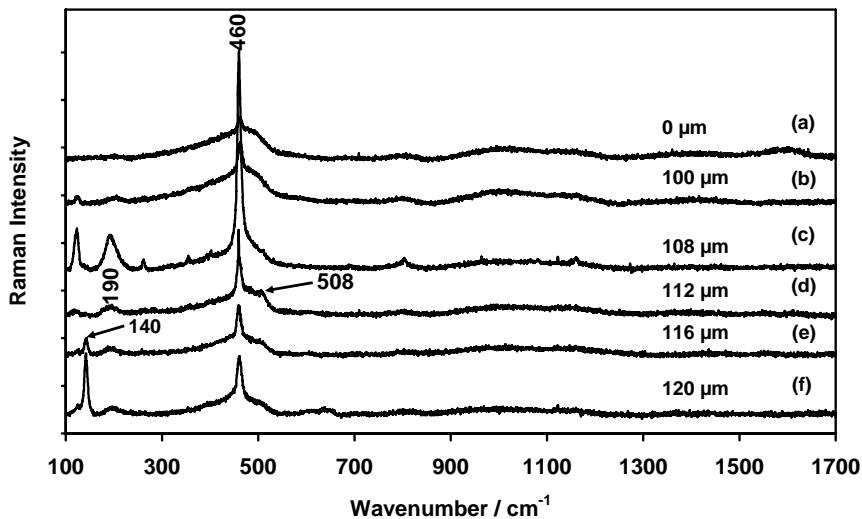


Figure 4.2.4. Raman spectra in which the glaze surface spectrum in (a) at 0 μm shows only the glaze. The spectra shown from 100 to 120 μm for this sample D (unknown shard) typically show the spectral evolution of the interfacial region

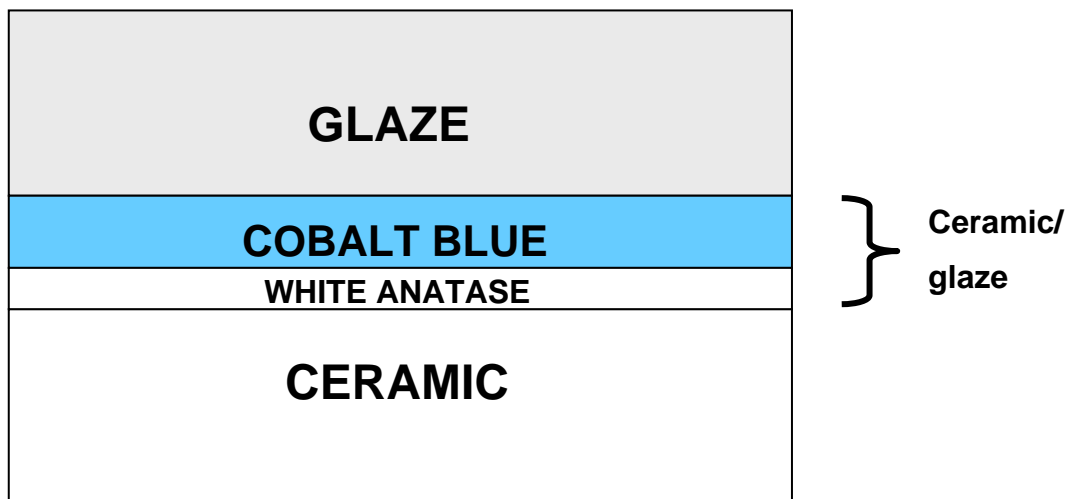


Figure 4.2.5. Schematic view of the ceramic/glaze interfacial region as determined from the Raman glaze profile in Figure 4.2.4

Figure 4.2.5 shows the order in which the pigments were applied on the artifact [sample D (of unknown archaeological origin)] at the time of manufacture. The order shown here suggests that the white anatase was applied first before the blue pigment. This suggests a deliberate intention to whiten the artifact before decorations with cobalt blue pigment were undertaken in order to create better pigment and surface background contrast, thus giving some insight into the methods used by the manufacturers of the artifact.

The identification of the white anatase itself on this artifact tells its own story. First, since white anatase is known to have been manufactured² for the first time during the 1920s, this artifact could not be of ancient Ming or non-Ming origin. The implication for the site where the artifact was excavated is that it is unlikely to be

older than the oldest piece found in it. This line of reasoning should then add value to work done by archaeologists in dating archaeological sites.

4.3. Identification of pigments, characterisation and implications

A description of the identified pigments will be given in this section. This will be accompanied by a detailed analysis of each pigment as it is found on the artifacts. The implications of its presence in relation to art and archaeology will also be discussed. It should be noted, for example, that a new synthetic pigment that is found on an artifact presented as an invaluable ancient artifact immediately raises questions,³ especially when these artifacts are traded at high prices. Also, the correct dating of ancient artifacts invariably benefits discussions on history and archaeology.⁴

4.3.1. Cobalt aluminium oxide (CoAl_2O_4)

Cobalt aluminium oxide (CoAl_2O_4) also known as cobalt blue, is the origin of the blue colour on all the shards studied. Cobalt blue belongs to a class of compounds generally characterised by a cation in an octahedral position (A) and another cation in a tetrahedral position [B], such that they can be represented as $(\text{A}_{1-x}\text{B}_x)[\text{A}_x\text{B}_{2-x}]\text{O}_4$ and $0 \leq x \leq 1$. For the normal spinels, $x = 0$, such that we obtain $(\text{A})[\text{B}_2]\text{O}_4$. For all other $0 < x \leq 1$, we get many different types of inverse spinel.¹

Cobalt blue finds applications as a colorant in a variety of industries such as plastics, paint, fibres, paper, rubber, glass and cement.⁵ Other applications include glazes, ceramic bodies, porcelain enamels and as contrast-enhancing luminescent pigment in TV tubes.^{1,5,6} It is a very stable pigment with a long history of use in ceramic artifacts, both ancient and modern. Spinel such as cobalt blue belong to a ceramic oxide family with wide applications in geophysics,⁴ magnetism,⁵ irradiated

environments,^{6,7} as well as colour enhancers.^{8,9} Yet, until recently,¹⁰ the cobalt blue Raman spectrum within ceramic artifacts had not been determined.

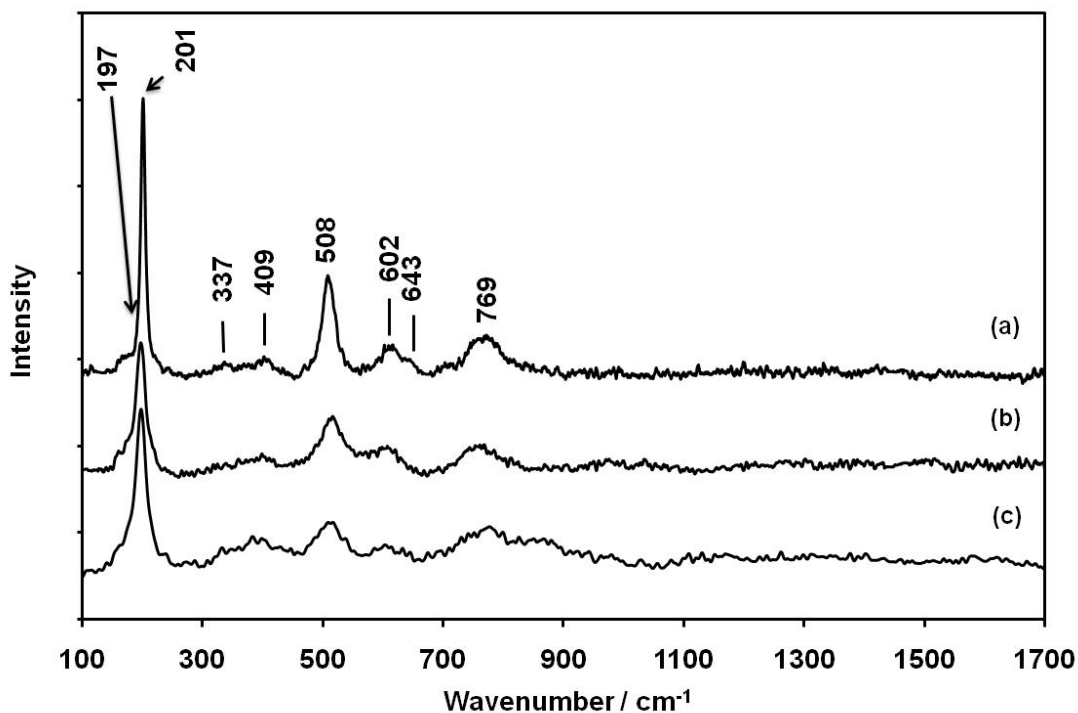


Figure 4.3.1.1. The Raman spectra of cobalt blue cooled rapidly (a), cooled slowly (b) and a commercial sample (c); the commercial sample was supplied by *Farbmühle Kraemer* in Germany and was used as received

Figure 4.3.1.1. shows the Raman spectra of cobalt blue cooled rapidly (a), cobalt blue cooled slowly (b), and a commercial sample of cobalt blue used as received (*Farbmühle Kraemer*, Germany) is shown in (c).

As a normal spinel structured pigment, cobalt blue belongs to space group $Fd3m$ O_h^7 with 56 atoms per unit cell ($Z = 8$).^{11,12} Group theory, which is a branch of abstract mathematics, is applied widely in the physical sciences. This theory is used here to develop vibrational selection rules for the blue pigment (CoAl_2O_4), thereby determining the number of expected vibrations within the pigment crystal. The

application of group theory will be focused on obtaining vibrational information as it relates to Raman and infrared spectroscopy. It may be noted here that group theory can also be applied in chemistry to obtain other physical properties such as parity, chirality of molecules and the construction of molecular orbitals.¹³ In the study of Raman and infrared spectroscopy, point groups are used to determine the normal modes of vibration and the relevant selection rules. A well-defined and well-known correlation method, clearly documented by Fateley and co-workers¹³ is used to derive the total number of vibrational modes for cobalt aluminium oxide (CoAl₂O₄).

The procedure of the correlation method begins by determining the degrees of vibrational freedom (f^{γ}) in each site species for γ of an equivalent set of atoms using:

$$f^{\gamma} = t^{\gamma} \cdot n \quad 4.1$$

where t^{γ} = number of translations in site species γ
 n = number of atoms in an equivalent set

The degrees of vibrational freedom (f^{γ}) from each site species γ that are calculated are then used to determine the degrees of freedom (a_{γ}) that are contributed by each site species γ to the factor group ζ , as follows:

$$f^{\gamma} = a_{\gamma} \sum_{\zeta} C_{\zeta} \quad 4.2$$

where C_{ζ} is the degeneracy of the species ζ of the factor group.

Table 4.3.1.1 lists the values of C_{ζ} .

Table 4.3.1.1. The values of the species that are chosen are shown below and depend on the type of crystal or molecule being considered.

Species	Value of C_z
A	1
B	1
E	2
T	3
G	4
H	5

It is from this list that specific values for a particular symmetry species are chosen, depending on the type of crystal under consideration. The use of these symbols (known as Mulliken symbols) and the symmetry properties that they represent are well known.¹⁴

The degrees of freedom contributed from each site species (a_γ) to the degrees of freedom (a_z) of the factor group may now be written directly as:

$$a_z = \sum_{\gamma} a_{\gamma} \quad 4.3$$

The construction of the irreducible representation for each equivalent set of atoms ($\Gamma_{\text{equivalent set}}$), in this case cobalt (Co), aluminium (Al) and oxygen (O), follows directly by summing the product of the factor group and its degrees of freedom obtained from equation 4.3:

$$\Gamma_{\text{equivalent set}} = \sum_{\zeta} a_{\zeta} \zeta \quad 4.4$$

The total irreducible representation (Γ^{crystal}) is simply the sum of irreducible representations for each equivalent set:

$$\Gamma^{\text{crystal}} = \Gamma_{\text{equivalent set (Co)}} + \Gamma_{\text{equivalent set (Al)}} + \Gamma_{\text{equivalent set (O)}} \quad 4.5$$

By subtracting the acoustic modes, Γ^{acoustic} , we obtain the total irreducible representation of the pigment crystal:

$$\Gamma_{\text{Vibration}}^{\text{CoAl}_2\text{O}_4} = \Gamma^{\text{crystal}} - \Gamma^{\text{acoustic}} \quad 4.6$$

The crystal structure of CoAl_2O_4 belongs to space group $Fd\bar{3}m (O_h^7)$ with 56 atoms per unit cell ($Z = 8$)^{11,12} where Z is the number of molecular units per unit cell. The number of molecular units per Bravais cell (Z^B) is $Z^B = Z / \text{L.P.}$, where L.P. is the number of lattice points in $Fd\bar{3}m (O_h^7)$ that can be determined. This is done in order to reduce the number of Bravais cells in the crystallographic cell, thereby ensuring that the obtained irreducible representations do not contain multiples of the set of vibrations needed to describe the crystal. From this information, it follows that the number of equivalent atoms may be listed as Co = 2, Al = 4 and O = 8.

Using information from site symmetry tables for the Bravais space cell, character tables and correlation tables,¹⁴ it was possible to derive an equation for the expected number of normal modes in the crystalline cobalt aluminium oxide. The Bravais space cell site symmetries are all the possible kinds of site for the particular crystal symmetry (for example, O_h^7). Table 4.3.1.2 gives a list of the O_h^7 site symmetry species that have been used for the CoAl_2O_4 crystal.

University of Pretoria etd – Kock, L.D. (2009)

Table 4.3.1.2. The distinct kinds of T_d , D_{3d} and C_{3v} sites and the number of equivalent atoms that can occupy each distinct site within the same distinct kind of site

Bravais cell site symmetry	Number of equivalent atoms on this site of the Bravais cell	Number of kinds of site of this symmetry
$2T_d(2)$	2	2
$2D_{3d}(4)$	4	2
$C_{3v}(8)$	8	1

From Table 4.3.1.2, only two distinct kinds of T_d site can accommodate two equivalent atoms. We therefore conclude that the site symmetry for Co (cobalt) is T_d ($n = 2$) where n is the number of atoms in an equivalent set. Similarly, site symmetry for Al (aluminium) is D_{3d} ($n = 4$) and that for O (oxygen) is C_{3v} ($n = 8$).

Table 4.3.1.3. Aluminium atom site D_{3d} , with the degree of vibrational freedom for each species ($n = 4$ atoms / equivalent set)

D_{3d} species	Translations	t^y	Degree of vibrational freedom: $f^y = n.t^y$
A_{1g}		0	0
A_{2g}		0	0
E_g		0	0
A_{1u}		0	0
A_{2u}	T_z	1	4
E_u	T_x, T_y	2	8

Table 4.3.1.4. Cobalt atom site T_d , with the degree of vibrational freedom for each species ($n = 2$ atoms / equivalent set)

T_d species	Translations	t^Y	Degree of vibrational freedom: $f^Y = n.t^Y$
A_1		0	0
A_2		0	0
E		0	0
T_1		0	0
T_2	T_x, T_y, T_z	3	6

Table 4.3.1.5. Oxygen atom site C_{3v} , with the degree of vibrational freedom for each species ($n = 8$ atoms / equivalent set)

C_{3v} species	Translations	t^Y	Degree of vibrational freedom: $f^Y = n.t^Y$
A_1	T_z	1	8
A_2		0	0
E	T_x, T_y	2	16

Once the degrees of vibrational freedom have been determined in this manner, the correlation table can be completed from T_d , D_{3d} and C_{3v} to O_h^7 . Tables 4.3.1.6, 4.3.1.7 and 4.3.1.8 complete these correlations using abbreviated tables dealing only with species that are involved in the $CoAl_2O_4$ crystal.

Table 4.3.1.6. Correlation between the D_{3d} site group and the O_h^7 factor group for the aluminium atoms ($n = 4$ atoms / equivalent set). Note that italicised T in the t^Y column designates translations, while the non-italicised T designates the degeneracy of a particular symmetry species

Aluminium (Al – D_{3d} ($n=4$))							
f'	t^Y	D_{3d} Site symmetry species containing translations	correlations	O_h^7 - Factor group species	C_ζ	a_ζ	a_Y $\frac{a_{A_{2u}} + a_{E_u}}$
4	1(T_z)	A_{2u}		A_{2u}	1	1	1+0
8	2($T_{x,y}$)	E_u		E_u	2	1	0+1
				$T_{1u}(T_{x,y,z})$	3	2	1+1
				T_{2u}	3	1	0+1
$\Gamma_{Al} = A_{2u} + E_u + 2T_{1u} + T_{2u}$							

Table 4.3.1.7. Correlation between the T_d site group and the O_h^7 factor group for the cobalt atoms ($n = 2$ atoms / equivalent set). Note that italicised T in the t^Y column designates translations, while the non-italicised T designates the degeneracy of a particular symmetry species

Cobalt (Co – T_d ($n = 2$))							
f'	t^Y	T_d Site symmetry species containing translations	correlations	O_h^7 - Factor group species	C_ζ	a_ζ	a_Y $\frac{a_{T_2}}$
6	1(T_z)	T_2		T_{2g}	3	1	1
				$T_{1u}(T_{x,y,z})$	3	1	1
$\Gamma_{Co} = T_{2g} + T_{1u}$							

Table 4.3.1.8. Correlation between the C_{3v} site group and the O_h factor group for the oxygen atoms ($n = 8$ atoms / equivalent set). Note that italicised T in the t^Y column designates translations, while the non-italicised T designates the degeneracy of a particular symmetry species

Oxygen ($O - C_{3v}$ ($n = 8$))							
f'	t^Y	C_{3v} Site symmetry species containing translations	correlations	O_h - Factor group species	C_z	a_z	a_y $a_{A_{2u}} +$ a_{E_u}
8	$1(T_z)$	A_1		A_{1g}	1	1	1+0
16	$2(\bar{T}_{x,y})$	E		T_{2g}	3	2	1+1
				A_{2u}	1	1	1+0
				$T_{1u}(\bar{T}_{x,y,z})$	3	2	1+1
				E_g	2	1	0+1
				T_{1g}	3	1	0+1
				E_u	2	1	0+1
				T_{2u}	3	1	0+1
$\Gamma_O = A_{1g} + 2T_{2g} + A_{2u} + 2T_{1u} + E_g + T_{1g} + E_u + T_{2u}$							

When equation 4.6 is applied to the results in Tables 4.3.1.6, 4.3.1.7 and 4.3.1.8 and taking into account that acoustical modes need to be subtracted, the same character as the translations listed in the character tables results in the total irreducible representation of $CoAl_2O_4$:

$$\Gamma_{\text{Vibration}}^{CoAl_2O_4} = \Gamma^{CoAl_2O_4} - \Gamma^{\text{acoustic}} \quad 4.7$$

$$\Gamma_{\text{Vibration}}^{CoAl_2O_4} = \Gamma_{Co} + \Gamma_{Al} + \Gamma_O - \Gamma^{\text{acoustic}} \quad 4.8$$

Substituting with information from Tables 4.3.1.6, 4.3.1.7 and 4.3.1.8, and collecting terms, using the character tables,¹³ to determine which modes will be active in Raman and/or infrared and which will be inactive in both, the required equation is readily obtained as:

$$\begin{aligned} \Gamma_{\text{Vibration}}^{\text{CoAl}_2\text{O}_4} &= \{T_{2g} + T_{1u}\} + \{A_{2u} + E_u + 2T_{1u} + T_{2u}\} + \{A_{1g} + 2T_{2g} \\ &+ A_{2u} + 2T_{1u} + E_g + T_{1g} + E_u + T_{2u}\} - T_{1u} \end{aligned} \quad 4.9$$

or

$$\Gamma_{\text{Vibration}}^{\text{CoAl}_2\text{O}_4} = A_{1g} (\text{R}) + 3T_{2g}(\text{R}) + E_g(\text{R}) + 4T_{1u} (\text{IR}) + T_{1g} + 2A_{2u} + 2E_u + 2T_{2u} \quad 4.10$$

This predicts five Raman active modes ($A_{1g} + E_g + 3T_{2g}$). Both the synthesised pigment and that on the shards (Figure 4.3.1.1 (A and B)) show more Raman bands than the number predicted by group theory.

However, it is well known that cationic disorder in spinel compounds lowers the symmetry, thereby increasing the vibrational modes.⁹ This may account in part for the additional bands observed for the cobalt blue spectrum from the shard. X-ray diffraction patterns (Figure 4.3.1.2) also show the spinel structured cobalt blue to be the only phase present in the pure synthesised cobalt blue samples (see also reference 7), and therefore it is expected that all the observed Raman bands from the pure synthesised samples will be those of cobalt blue. Figure 4.3.1.1 (B) is a typical spectrum of cobalt blue on the shard samples. The shoulder at about 410 cm^{-1} in Figure 4.3.1.1 (B) is due to cobalt blue.

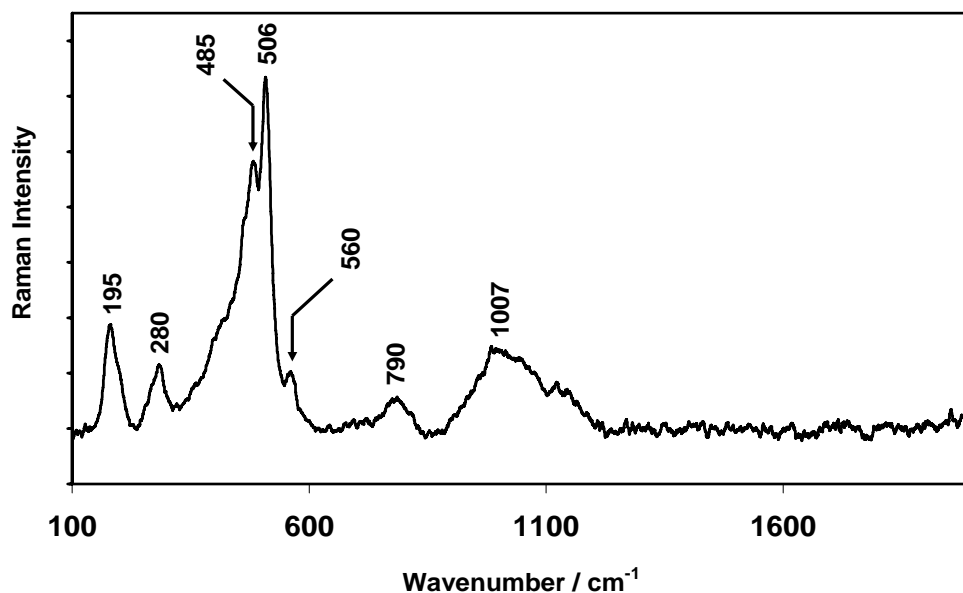


Figure 4.3.1.1. (B) A representative Raman spectrum of an underglaze blue pigment at the ceramic/glaze interface showing all the identified Raman bands. The broad band at 1007 cm^{-1} is due to the silicate glaze, while the shoulder at around 410 cm^{-1} (not labelled) is due to cobalt blue

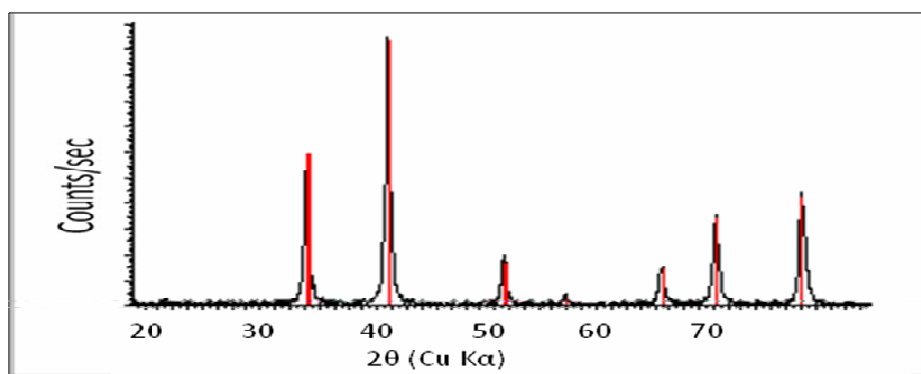


Figure 4.3.1.2. The figure shows an XRD pattern of synthesised cobalt blue showing cobalt blue as the only phase present in the sample. This sample was removed from the furnace and allowed to cool slowly

However, when a comparison is made between cobalt blue and a similar spinel (MgAl_2O_4) for which assignments have already been made,^{11,15-17} a likely Raman band assignment for the cobalt blue is predicted to be as follows: 197 cm^{-1} ($T_{2g}(1)$), 508 cm^{-1} ($T_{2g}(2)$), 643 cm^{-1} ($T_{2g}(3)$), 409 cm^{-1} (E_g) and 769 cm^{-1} (A_{1g}) for the pure isolated pigment. The corresponding Raman bands of the blue pigment on the shards (Figure 4.3.1.1 (B)) are 195 cm^{-1} ($T_{2g}(1)$), 506 cm^{-1} ($T_{2g}(2)$), 690 cm^{-1} ($T_{2g}(3)$), 410 cm^{-1} (E_g) and 790 cm^{-1} (A_{1g}).

The additional Raman bands at 560 cm^{-1} and 485 cm^{-1} could be the result of differential cooling between the ceramic body and the glaze. Indications of tensile stress imposed on the interface by this phenomenon have been indicated by interfacial quartz in studies of glazed porcelain.¹⁷ Figure 4.3.1.3 shows representative surface (glaze) and interfacial (ceramic/glaze) Raman spectra for the Meissen sample (the broken cup shown in Figure 4.1.3 (E)).

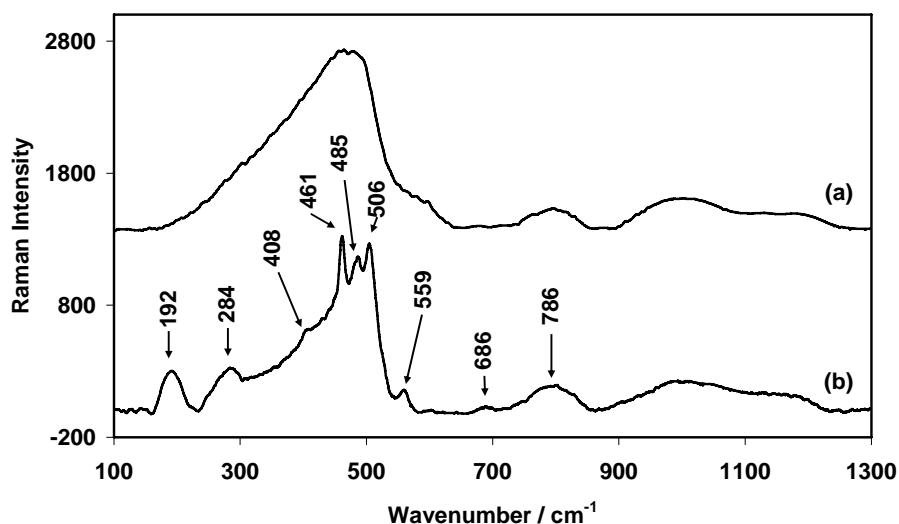


Figure 4.3.1.3. The surface (a) and interface (b) spectra for the Meissen sample E (Figure 4.1.3 (E)), is typical for all the blue and white porcelain blue pigment in our possession. The 461 cm^{-1} Raman band is attributed to α -quartz which is similar to all the blue and white porcelain in our study

4.3.2. Amorphous carbon

The Raman spectra of several samples show the presence of broad Raman bands around 1300 cm^{-1} and 1600 cm^{-1} , and these are attributed to amorphous carbon.¹⁸ In considering a single crystal of graphite, factor group analysis¹⁹ shows that this system belongs to the D_{6h}^4 symmetry group and that the Brillouin zone centre modes can be decomposed into the following irreducible representation:²⁰

$$\Gamma = A_{2u} + 2B_{2g} + E_{1u} + 2E_{2g} \quad 4.11$$

The separation of these modes into Raman, infrared and inactive modes is shown in Table 4.3.2.1.

Table 4.3.2.1. The Raman, infrared and inactive modes of a single graphite crystal as compiled from the literature

Raman active	IR active	Silent in both ²³	Observed mode ^{21,22} (cm^{-1})
$E_{2g}(1)$	-	-	42
$E_{2g}(2)$	-	-	1581
	A_{2u}		867
	E_{1u}		1588
		$B_{2g}(1)$	127**
		$B_{2g}(2)$	Not observed

**Observed by neutron scattering.

The amorphous carbon that is found on the sample is present due to contact with the samples, either unintentionally through contamination or intentionally through its use as a black pigment on the artifact. Ancient black pigments that have been used on artifacts come from two broad categories, lamp black and ivory black. The latter

is being so called due to its origin from calcined bone or ivory.^{24,25} Ivory black can usually be distinguished from lamp black in its Raman spectrum by a phosphate (PO_3^{2-}) feature at 960 cm^{-1} as a result of collagen from animal remains.²⁴ However, other work¹⁹ has shown that some samples of ivory black often fail to show the phosphate Raman band. Therefore, the absence of the 960 cm^{-1} band cannot be used to exclude ivory black as the black pigment that is often found on ancient artifacts and also the samples under study in this work.

Typically, blue and white ceramic samples also show the presence of amorphous carbon on the surfaces of the glaze but not in the interior of the sample glaze (Figure 4.3.1.3).

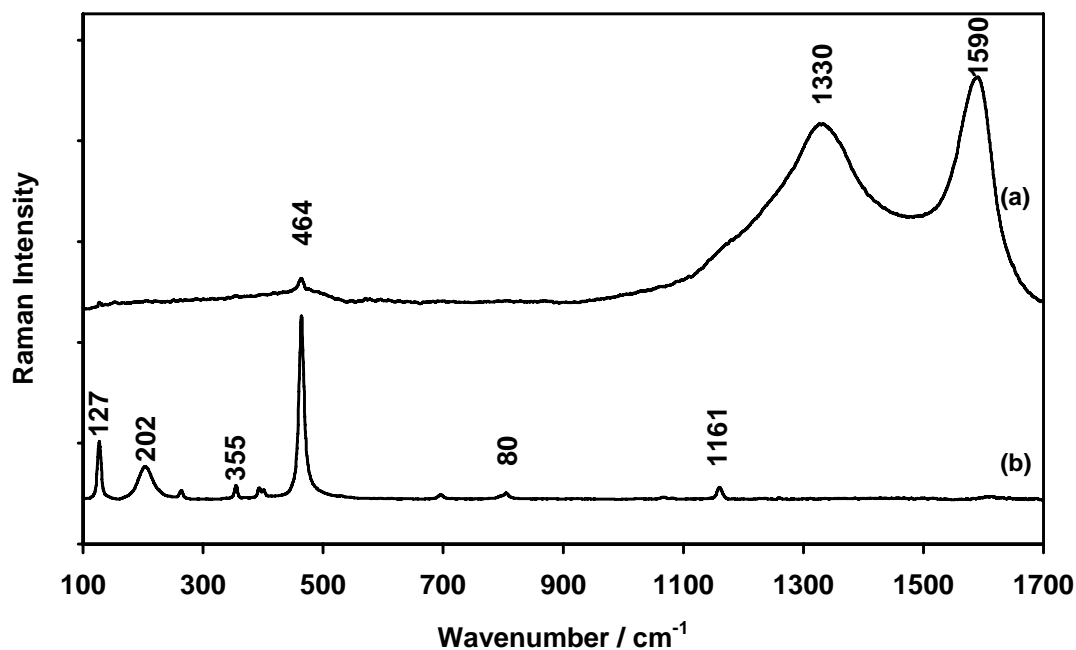


Figure 4.3.1.4. The surface of sample F (excavated cup) shows a thin layer of amorphous carbon (a) ($0\text{ }\mu\text{m}$), while less than $4\text{ }\mu\text{m}$ below the surface, the carbon disappears completely. This phenomenon is typical of all the samples in this study

The presence of amorphous carbon on the surfaces of these samples could be due to surface contamination during manufacturing. The amorphous carbon contamination is also predominant towards the bottom side of the artifact (dish, cup or plate), suggesting that the origin of the contaminated draft or gas may have been from the bottom of the saggar where the kiln fire is more likely to be located.

4.3.3. Anatase (TiO₂)

Anatase was detected on the surfaces of two of the shards of archaeological origin (Figure 4.1.3, (C and D)), as well as on the ceramic body of the Meissen shard sample (Figure 4.1.3, (E)). On samples C and D, anatase was detected at the interface below a thin layer of cobalt blue pigment presumed to have leached out of the blue glaze. A schematic view of the ceramic/glaze interface on the white background of samples C and D is shown in Figure 4.2.4.

Anatase is one of the three polymorphic forms of TiO₂; the other two are brookite and rutile.^{26,27} However, all three have very distinct Raman band fingerprints. Only anatase and rutile were detected on these samples. However, brookite and its Raman band positions are discussed here for comparison with the other two TiO₂ polymorphs (anatase and rutile). While anatase shows a strong Raman band at 140 cm⁻¹, brookite shows a strong band at 153 cm⁻¹ and rutile shows no such band.²⁸

The anatase form is identified by Raman band assignments at 140 cm⁻¹ (E_g), 197 cm⁻¹ (E_g), 394 cm⁻¹ (B_{1g}), 517 cm⁻¹ (B_{1g}) and 637 cm⁻¹ (E_g).^{29,30} Figure 4.3.3.1(b) shows the full anatase Raman spectrum as identified on the body of the Meissen shard sample E. In other situations, once a full spectrum can be identified, it is usually sufficient to look for the intense 140 cm⁻¹ (E_g) Raman band in and around the

same sample for positive identification of anatase. This is seen, for instance, for sample D in Figure 4.2.3(e) and (f) where anatase occurs with α -quartz¹.

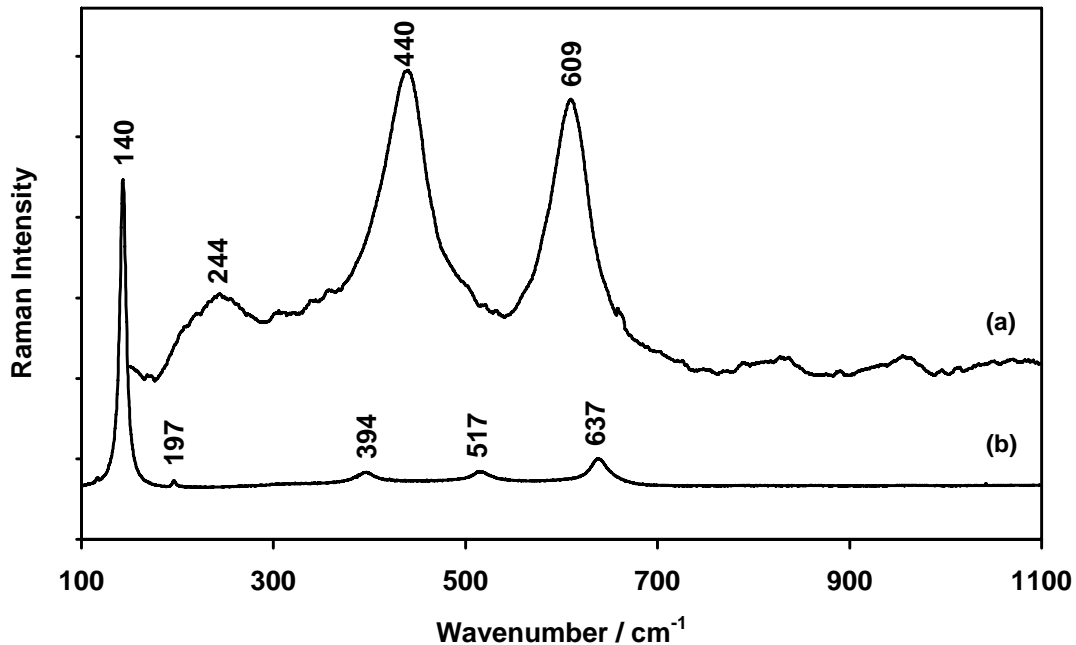


Figure 4.3.3.1. (a) Rutile (TiO₂) spectrum, with characteristic Raman bands at 244 cm⁻¹ (A_{1g}), 440 cm⁻¹ (E_g) and 609 cm⁻¹ (B_{1g}), and (b) anatase (TiO₂) spectrum, with bands at 140 cm⁻¹ (E_g), 197 cm⁻¹ (E_g), 394 cm⁻¹ (B_{1g}), 517 cm⁻¹ (B_{1g}) and 637 cm⁻¹ (E_g). Both (a) and (b) are recorded from the ceramic body of sample E (Meissen)

4.3.4 Rutile (TiO₂)

Rutile was also detected in the ceramic body of the Meissen sample E (Figure 4.3.3.1(a)). This TiO₂ polymorph was identified by its characteristic Raman bands at 244 cm⁻¹ (A_{1g}), 440 cm⁻¹ (E_g) and 609 cm⁻¹ (B_{1g}). Anatase-to-rutile phase transformation^{31,32} occurs between 800 °C and 1 100 °C. The presence of rutile in

the ceramic body of sample E suggests that temperatures of at least 800 °C were reached during the manufacture of the artefact.

However, what is interesting about the ceramic body of the Meissen sample (E) is that anatase (TiO₂), rutile (TiO₂) and mullite co-exist in the same ceramic body sample. The mullite (2Al₂O₃·SiO₂ or 3Al₂O₃·2SiO₂) detected in the ceramic body indicates the use of kaolinite minerals as starting materials since temperatures above 1 200 °C are required for these kaolinite/mullite transformations.

Also, Meissen ceramic body samples have already been confirmed to have been sintered at these high temperatures.³³ However, at these temperatures, it is expected that anatase (TiO₂) should be converted to rutile (TiO₂), its high-temperature polymorphic form.

The answer to this may lie in the mechanism of anatase/rutile phase transformation itself. It has already been shown that the reduced nucleation probability of anatase could impede the anatase-to-rutile phase transformation past the critical temperature.³⁴ It should be noted that this phase transformation can also be influenced by the presence of other materials in the sample.¹ This point needs further investigation as this work continues.

4.3.5 Hematite (α-Fe₂O₃)

Hematite was detected only as part of the brown line at the bottom of one of the Ming shard samples, B (Figure 4.3.4.1). This pigment was identified through some of its characteristic Raman bands and their assignments³⁵ at 221 cm⁻¹ (A_{1g}), 294 cm⁻¹ (E_g), 409 cm⁻¹ (E_g) and 601 cm⁻¹ (E_g) (Figure 4.3.4.2).

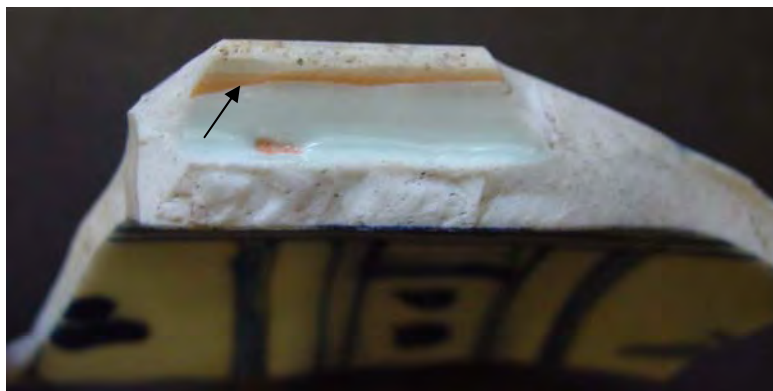


Figure 4.3.5.1. The brown line at the bottom of Ming sample B is indicated with an arrow. This line is more prominent on the inside bottom than the outside bottom where it appears to have been scraped off

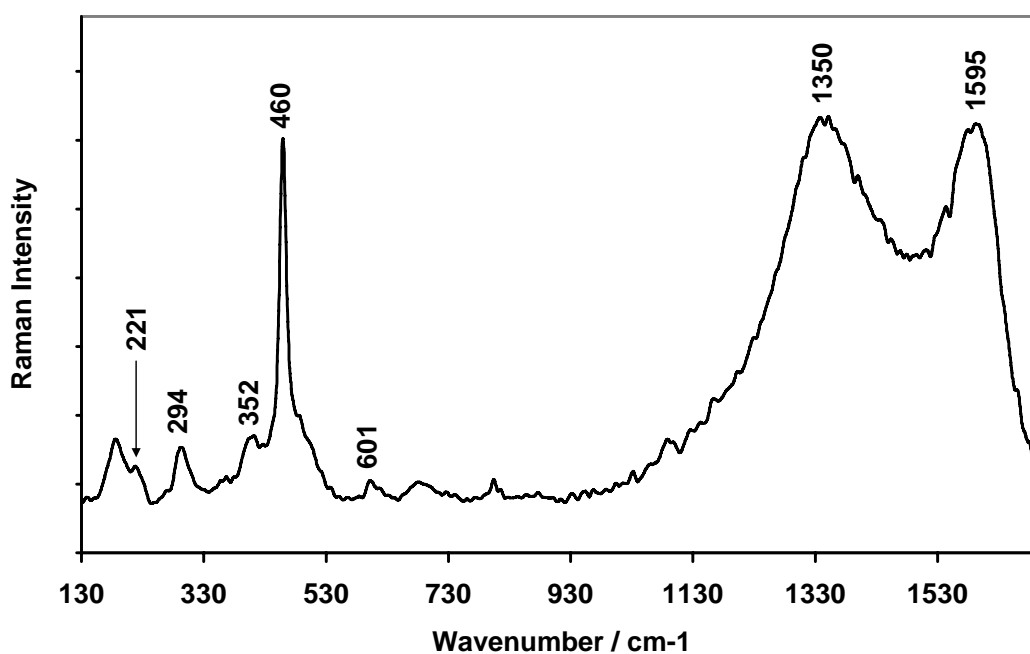


Figure 4.3.5.2. Spectrum showing typical $\alpha\text{-Fe}_2\text{O}_3$ Raman bands at 221 cm^{-1} (A_{1g}), 294 cm^{-1} (E_g), 409 cm^{-1} (E_g) and 601 cm^{-1} (E_g) as collected directly from the brown line of sample B, indicated with an arrow in Figure 4.3.4.1

In this case it was found mixed with amorphous carbon appearing as broad Raman bands at 1350 cm^{-1} and 1595 cm^{-1} . The intense band at around 460 cm^{-1} is attributed to $\alpha\text{-SiO}_2$.

This brown line is similar to what has been called “the chocolate bottom” on Vietnamese porcelain.³⁶ Many explanations have been put forward as to its existence. It is believed that these could be deliberate markings or an adhesion substance to prevent the item from sticking to the sagger.³⁶ In this case, the brown line could be contamination, as it appears that it was scraped off the outside of the artifact.¹

4.3.6 Mullite ($2\text{Al}_2\text{O}_3\cdot\text{SiO}_2$ or $3\text{Al}_2\text{O}_3\cdot 2\text{SiO}_2$)

Mullite is part of a broader group of materials that have recently gained attention due to the possibility of their application in solid oxide fuel cells,³⁷ oxygen sensors and gas separation membranes,^{38,39} in addition to their traditional ceramics applications. The detection of mullite in the ceramic body of the Meissen sample is consistent with studies in other laboratories.⁴⁰ A representative mullite spectrum as collected from the Meissen sample (sample shown in Figure 4.1.3 (E)) is shown in Figure 4.3.5.1. The large number of Raman bands on this spectrum does not come as a surprise. Vibrational analysis of mullite, using group theory, shows that as many as 42 Raman-active vibrational modes are possible,⁴¹ as shown in equation 4.12:

$$\Gamma_{\text{Raman}} = 12A_g + 12B_{1g} + 9B_{2g} + 9B_{3g} \quad 4.12$$

Mullite was also detected in the ceramic body of Ming samples A and B, but only after a piece of the ceramic body had been ground into powder and moulded into a

smooth surface; a 100X objective lens was used to collect the spectra as has been successfully done elsewhere.⁴²

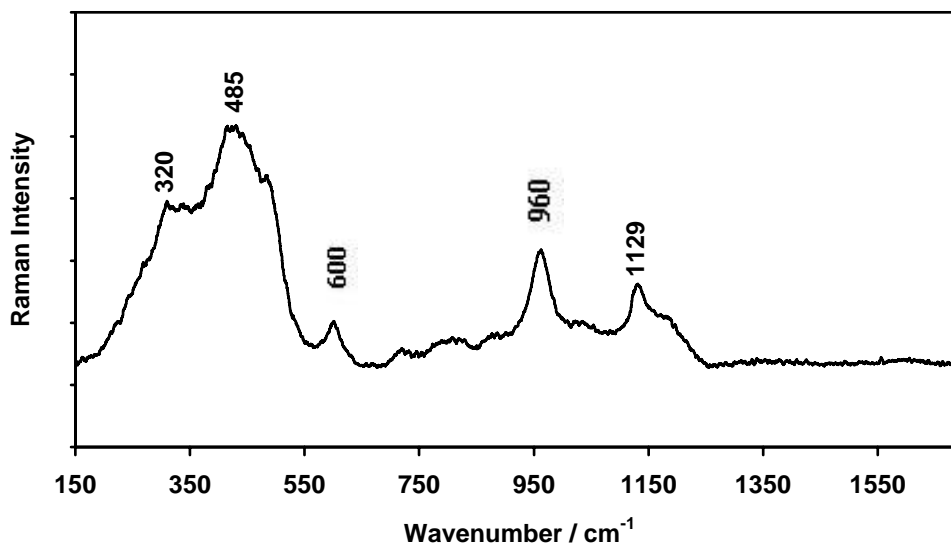


Figure 4.3.6.1. Spectrum of mullite in the ceramic body of the Meissen sample (Figure 4.1.3 (E)) with Raman bands at 320 cm^{-1} , 485 cm^{-1} , 600 cm^{-1} , 960 cm^{-1} and 1129 cm^{-1}

4.4 Intact plates

This section deals with the studies on the intact plates. These include two known museum intact plates of Ming dynasty origin and an unknown museum intact plate that appears to have gone through quite substantial restoration recently. The artifacts will be discussed in that order.

4.4.1 Ming dynasty plates Hongzhi (1488–1505) and Wanli (1573–1620)

The glaze depth profiling method that was used to study the Ming and Meissen artifacts and those of unknown origin was also applied to intact Ming dynasty plates

from the J.A. van Tilburg Museum of the University of Pretoria. The plates are of the Ming dynasty but from two distinct periods (Hongzhi (1488–1505) and Wanli (1573–1620)) within the Ming dynasty and are shown in Figure 4.1.3, (H) and (I) respectively.

Figures 4.4.1.1 and 4.4.1.2 show the Raman spectra collected from the ceramic/glaze interface of the two plates compared with those collected from the glaze surfaces. The blue pigment was then identified as CoAl_2O_4 in these Ming plates without the pigment being exposed to the surface.

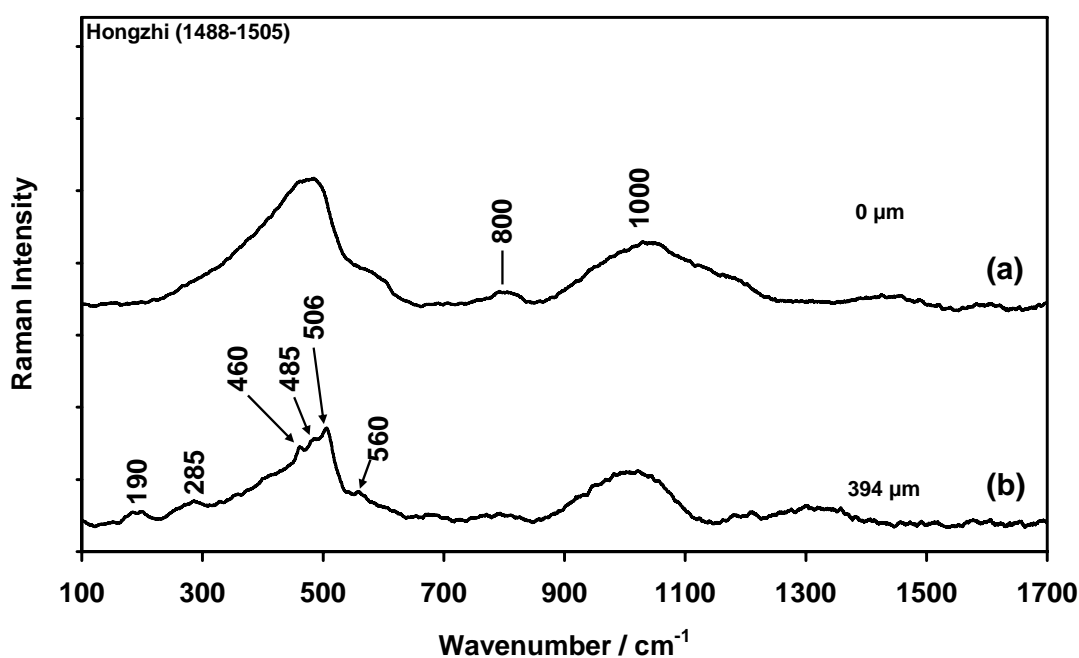


Figure 4.4.1.1. Surface (a) and interface (b) spectra for the Ming plate (Hongzhi (1488 – 1505)) shown also in Figure 4.1.3 (H). Note the glaze thickness of about 390 μm

Cobalt blue or cobalt aluminium oxide (CoAl_2O_4) is the origin of the blue colour in the Ming plates. The blue pigment on these plates was not mixed with amorphous

carbon as was the case with the other Ming shards. This is in contrast to the blue pigment on the archaeological shards which was mixed with amorphous carbon.

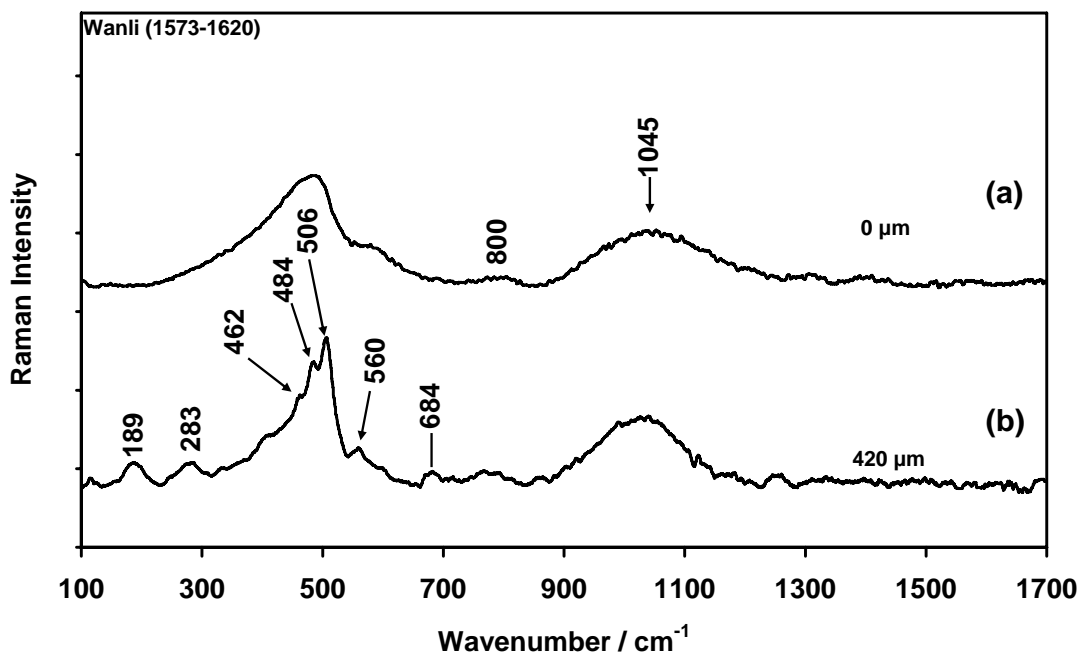


Figure 4.4.1.2. Surface (a) and interface (b) spectra for the Ming plate (Wanli (1573–1620)) shown also in Figure 4.1.3 (I). Note the glaze thickness of about 420 μm on this plate

Many more micro-Raman studies of Ming plates need to be undertaken in order to establish whether the lack of amorphous carbon in the blue pigment of these Ming samples was commonplace during the Ming period, or whether the samples under study in this work are exceptions.

4.4.2 Unknown intact plate

Unlike the Ming plates, this plate (Figure 4.4.2.1), although similar to the Ming dynasty plates, seemed to have been extensively restored and repainted.

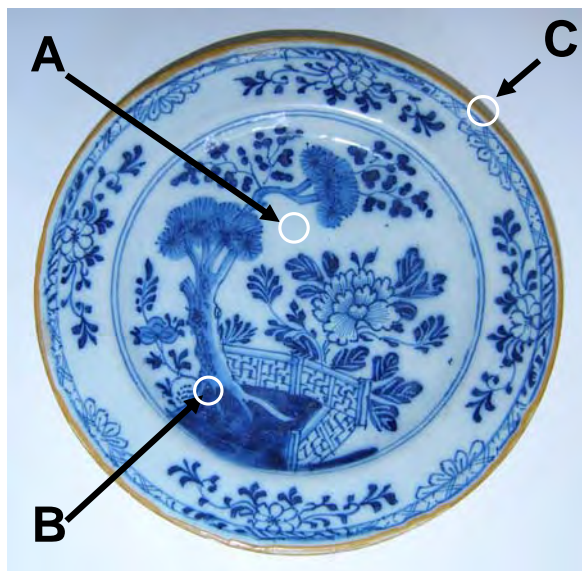


Figure 4.4.2.1. Unknown intact plate, showing the various positions chosen for study

Figure 4.4.2.2 shows the glaze depth profile Raman spectra on the white background of the unknown plate (position A in Figure 4.4.2.1). The white background clearly reveals a white SnO_2 ; the broad Raman bands around 500 cm^{-1} and 1000 cm^{-1} are attributed to the silicate glaze.

The presence of amorphous carbon on the surface of the glaze, as indicated by the doublet at around 1300 cm^{-1} and 1600 cm^{-1} , was noted. The presence of amorphous carbon is typical of all the ceramic artifacts that were chosen for study,

both the known or unknown museum specimen artifacts and those of archaeological origin.

A dark blue background (position B in Figure 4.4.2.1) was chosen for the glaze depth profile studies.

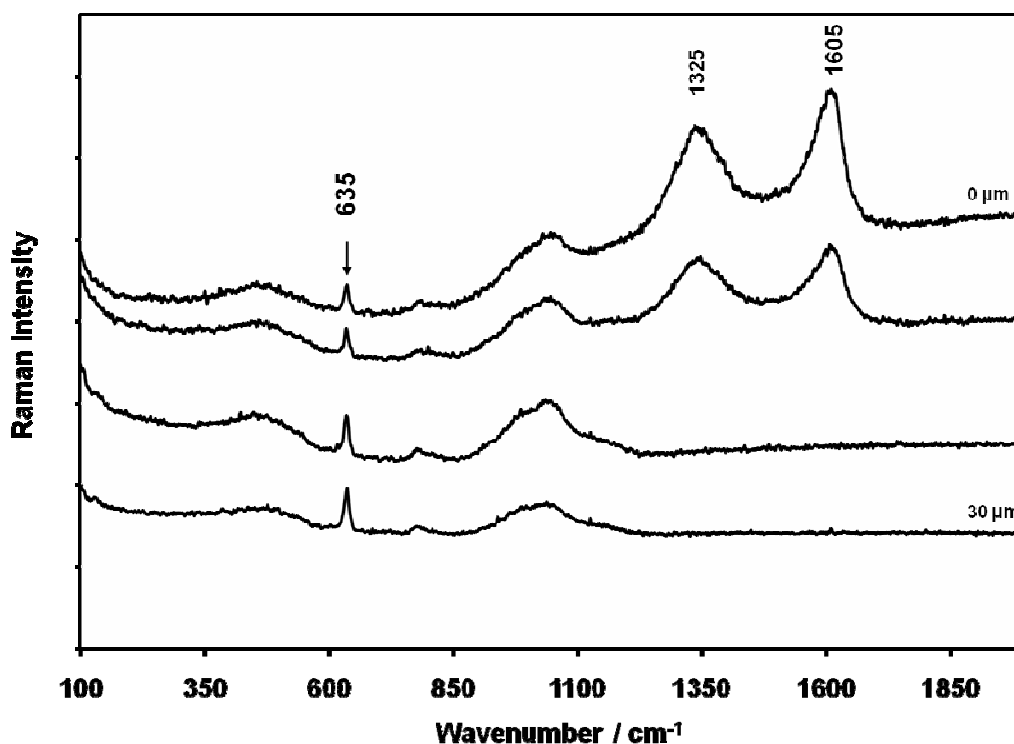


Figure 4.4.2.2. Glaze depth profile showing a predominantly cassiterite (SnO₂) glaze (position A in Figure 4.4.2.1). The blue pigment is not detected here despite the visibly blue glaze

The results (Figure 4.4.2.3) reveal a pigment that is spread from the surface to the interior of the glaze rather than at the ceramic/glaze interface. This pigment is

similar to the olivine/willemite type ($\text{Co}_x\text{Zn}_{2-x}\text{SiO}_4$ with $0 \leq x \leq 2$) pigments with a strong Raman band at 823 cm^{-1} , as reported in the literature.^{41,43} The spectrum also shows three less intense Raman bands in the region 300 cm^{-1} to 500 cm^{-1} (Figure 4.4.2.3).

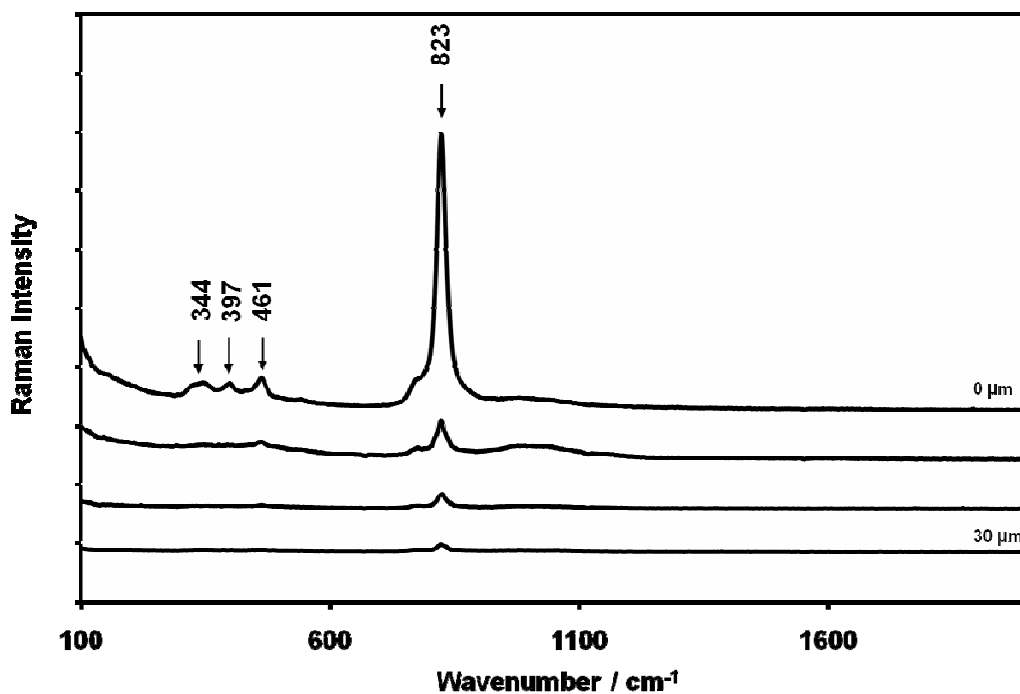


Figure 4.4.2.3. Glaze depth profile for the unknown plate (position B in Figure 4.4.2.1). The blue pigment on this plate shows that it has an olivine-type pigment and is more intense on the glaze surface rather than the glaze interior

Position C in Figure 4.4.2.1 consists of a “golden” or brown-yellow pigment laid on the surface of the artifact’s rim. Raman spectroscopy consistently shows this “golden” rim to be composed of the rutile phase of TiO_2 , trace amounts of calcite (CaCO_3) and the anatase phase of TiO_2 . These pigments point to a more modern restoration effort on this unknown museum piece. Firstly, should one argue that the rutile on the rim is due to an originally applied naturally occurring anatase, which

was then sintered at temperatures of between 800 °C and 1100 °C, other impurities associated with natural anatase should still be present. No other impurity (other than traces of CaCO_3) was detected in the rim.

Secondly, it was only early in the last century that industrial processes were developed²⁹ for the manufacture of pure anatase (1923) and rutile (1947).

More studies will have to be conducted to obtain more detailed chemical information on this artifact, including the correct identification of the type of olivine pigment. Nevertheless, the depth profiling method applied in this work opens a new avenue for research in the area of art and archaeology.

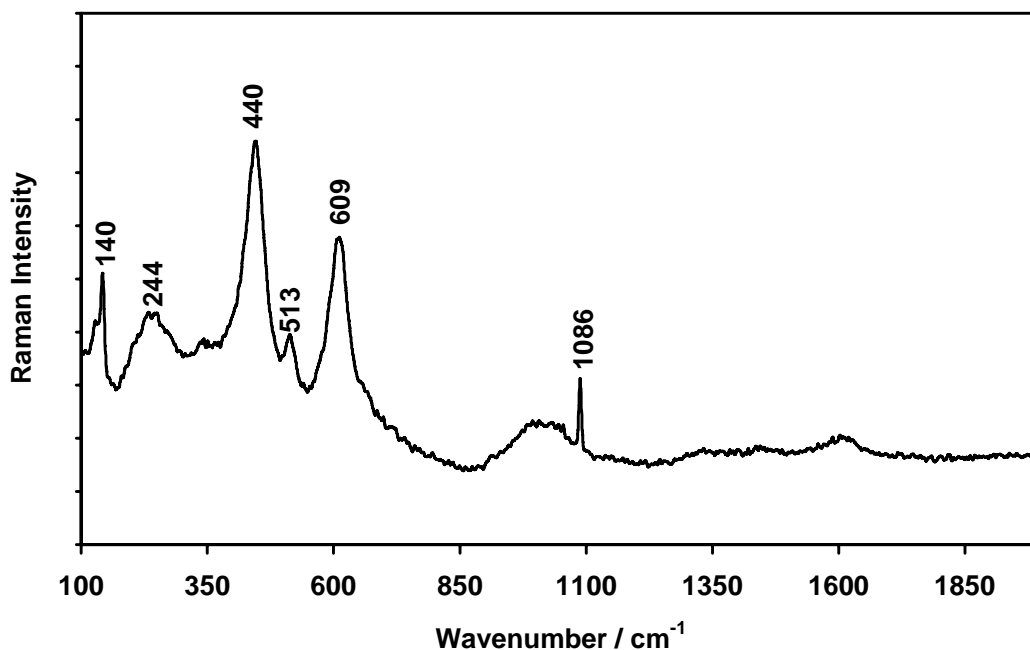


Figure 4.4.2.4. Raman spectrum of the “golden” rim, showing rutile as the main component as indicated by the main Raman bands with traces of anatase (140 cm^{-1}) and CaCO_3 . (1086 cm^{-1})

4.5 Conclusion

The porcelain glaze depth profile studies on intact plates that have been presented in this chapter provide a unique method for probing ceramic/glaze interfacial pigments by focusing the laser beam through the glaze. Laser powers of about 20 mW to 40 mW were used to probe porcelain glazes of 0.1 mm to about 0.4 mm. Interfacial layer structure was constructed from the Raman spectra obtained directly from the interface. Pigment identification and characterisation were therefore possible and in some cases the type and composition of these pigments may lead to conclusive cut-off dates for manufacturing.

In the case of the discovery of pure white anatase, the manufacturing date was placed after the 1920s, which is the date of first manufacture of pure white anatase. Cobalt blue (CoAl_2O_4), anatase (TiO_2), rutile (TiO_2), hematite ($\alpha\text{-Fe}_2\text{O}_3$), mullite ($2\text{Al}_2\text{O}_3\cdot\text{SiO}_2$ or $3\text{Al}_2\text{O}_3\cdot 2\text{SiO}_2$), amorphous carbon and an olivine/willemite type of compound were identified on the blue ceramic shards and plates that were studied. This study has established a benchmark on the study of ceramic/glaze interfacial pigments by focusing visible laser radiation through the glaze using confocal micro-Raman spectroscopy.

However, the success of this method on silicate-based glazes, such as the blue and white shards that have already been studied, does not necessarily extend to the SnO_2 -based glazes that were also commonly used in ancient times. A study on a tile shard from the Citadel of Algiers with a predominantly SnO_2 -based glaze will be presented in Chapter 5. This is expected to validate or invalidate the use of the glaze depth profile method on samples of this type, while gathering information that could be used in reconstruction and preservation work on ancient objects of cultural significance.

4.6 References

1. Kock, L.D. and de Waal, D. *J. Raman Spectrosc.* 2007, **38**, 1480.
2. Clark, R.J.H., Wang, Q. and Correia, A. *J. Archaeol. Sci.* 2007, **6**, 1.
3. Colomban, P., Milande, V. and Lucas, H. *J. Raman Spectrosc.* 2004, **35**, 68.
4. Baraldi, P. and Tinti, A. *J. Raman Spectrosc.* 2008, **39**, 963.
5. Luchesi, S. and Delta Guista, A. *Miner. Petrol.* 1997, **59**, 91.
6. Schiessl, W., Poltz, W., Karzel, H., Steiner, M. and Kalvius, G.M. *Phys. Rev. B.* 1991, **53**, 9143.
7. Yu, N., Sickafus, K.E. and Nastasi, M. *Phil. Mag. Lett.* 1994, **70**, 235.
8. Zinkle, S.J. *J. Nucl. Mater.* 1995, **219**, 113.
9. Melo, D.M.A., Cunha, J.D., Fernandes, J.D.G., Bernardi, M.I., Melo, M.A.F. and Martinelli, A.E. *Mater. Res. Bull.* 2003, **38**, 1559.
10. De Waal, D. *J. Raman Spectrosc.* 2004, **35**, 646.
11. Li, W., Li, J. and Gua, J. *J. Eur. Ceram. Soc.* 2003, **23**, 2289.
12. Thibaudeau, P. *J. Phys.: Condens. Matter.* 2002, **14**, 3543.
13. Fateley, W.G., Dollish, F.R., McDevitt, N.T. and Bentley, F.F. *Infrared and Raman Selection Rules for Molecular and Lattice Vibrations: The Correlations Method*, New York, Wiley-Interscience, 1971.
14. Borel, A. *Linear Algebraic Groups, Graduate Text in Mathematics*, 2nd edition. Berlin, New York, Springer-Verlag, 1971.
15. Wang, Z., Schiferl, D., Zhao, Y. and O'Niell, H.St.C. *J. Phys. Chem. Solids.* 2003, **64**, 2517.
16. Malezieux, J.M. and Birious, B. *Bull Mineral.* 1988, **111**, 649.

17. Thibaudeau, P. and Gervais, F. *J. Phys.: Condens. Matter.* 2002, **14**, 3543.
18. Kawashima, Y. and Katagiri, G. *Phys. Rev. B.* 1995, **14**, 53.
19. Mani, K.K. and Ramani, R. *Phys. Status. Solidi.* 1974, **B61**, 659.
20. Kawashima, Y. and Katagiri, G. *Phys. Rev. B* 1995, **14**, 52.
21. Nemanich, R.J. and Solin, S.A. *Phys. Rev. B.* 1979, **20**, 392.
22. Nemanich, R.J., Lucovsky, G. and Slin, S.A. *Mater. Sci. Eng.* 1977, **31**, 157.
23. Nieklow, R., Wakabayashi, N. and Smith, H.G. *Phys. Rev. B.* 1972, **5**, 4951.
24. Smith, G.D. and Clark, R.J.H. *J. Archaeol. Sci.* 2004, **31**, 1137.
25. Edwards, H.G.M. *J. Raman. Spectrosc.* 2000, **31**, 407.
26. Clark, R.J.H., Cridland, L., Kariuki, M.B., Harris, K.D.M. and Withnall, R. *J. Chem. Soc. Dalton Trans.* 1995, 2577.
27. Clark, R.J.H. *The Chemistry of Titanium and Vanadium.* Amsterdam, Elsevier, 1968.
28. Cassaignon, S., Koelsch, M. and Jolivet, J-P. *J. Mater. Sci.* 2007, **42**, 6689.
29. Burgio, L. and Clark, R.J.H. *J. Raman Spectrosc.* 2000, **31**, 395.
30. Miao, L., Tanemura, S., Toh, S., Kaneko, K. and Tanemura, M.J. *J. Crystal Growth.* 2004, **264**, 246.
31. Colomban, P. and Mazerolles, L. *J. Mater. Sci.* 1991, **26**, 3503.
32. Kim, D-W., Kim, T-G, and Hong, K.S. *J. Am. Ceram. Soc.* 1998, **81**, 1692.
33. Colomban, P. *J. Non-crystalline Solids.* 2003, **323**, 180.
34. Zhang, H. and Banfield, J. F. *J. Mater. Res.* 2000, **15**, 437.
35. De Faria, D.L.A., Venancio, S. and de Oliviera, M.T. *J. Raman Spectrosc.* 1997, **28**, 873.

36. Colomban, P., Liem, N.Q., Sagon, G., Tinh, H.X. and Hoah, T.B. *J. Cult. Herit.* 2003, **4**, 187.
37. Beran, A., Libowitzky, E., Burianek, M., Muhlberg, M., Percharroman, C. and Schneider, H. *Cryst. Res. Technol.* 2008, **43**, 1230.
38. Zha, S., Cheng, J., Liu, Y., Liu, X. and Meng, G. *Solid State Ionics.* 2003, **156**, 197.
39. Goodenough, J.B. *Ann. Rev. Mater.* 2003, **33**, 91.
40. Colomban, P. and Milande, V. *J. Raman Spectrosc.* 2006, **37**, 606.
41. Cui, H., Zayat, M. and Levy, D. *Chem. Mater.* 2005, **17**, 5562.
42. Liem, N.G., Sagon, G., Quang, V.X., Tan, H.V., Colomban, P. *J. Raman Spectrosc.* 2000, **31**, 933.
43. Fores, A., Llusar, M., Badenes, J.A., Calbo, J., Tena, M.A. and Monros, G. *Green Chem.* 2000, **2**, 93.

CHAPTER 5

Pigments on a tile from the Citadel of Algiers

The analysis and detailed characterisation of pigments on artworks and other materials of archaeological origin has become increasingly indispensable in the identification, authentication and restoration of these important artifacts and can lead to more effective conservation plans, thus preserving the artifacts for posterity. In the case of the tile from the Citadel of Algiers, the information could also be used to rebuild and restore the Citadel to its former pre-colonial state. This chapter therefore deals with the study of pigments on this tile shard. This tile shard was selected because, apart from its obvious historical significance, it has a predominantly SnO₂-based glaze. The glaze depth profile method that allows for the study of ceramic/glaze interfacial pigments on intact porcelain artifacts, as successfully used in Chapter 4, was applied to this tile shard as well, partly to validate the method and also to gather useful information on the shard. Some of the information presented in this chapter has been published in *Spectrochimica Acta Part A: Molecular and Biomolecular Spectroscopy*.¹

5.1 Tile history and description

The multi-coloured tile shard under study (see Figure 5.1.1) was obtained from the Citadel of Algiers.² The various colours are defined qualitatively for discussion purposes starting with the heterogeneous shades of yellow (bright yellow, orange yellow and brown yellow). The other colours are blue, white, reddish brown (line) and brown-black (line).



Figure 5.1.1. The different views of the Citadel tile highlight the different colours (above) and the relative thickness of the tile body (below) with respect to the glaze thickness

The tile shard body is composed mainly of brown material which will also be discussed in detail in this chapter. The white pigment on the tile forms the base on which all the other pigments are spread, in addition to the white surface sections which form part of the decoration (Figure 5.1.1).

The following is an extract from a French translation describing the origin of the tile and giving a short history of the Citadel of Algiers, obtained from the donor of the tile shard.²

THE CITADEL OF ALGIERS

TRANSLATION FROM THE FRENCH

“Situated at 118 metres above sea level, the Citadel of Algiers stood above the Medina (Temple) of El Djezair on the south-western side and formed the sloping angle from where the ramparts of the Medina ran downwards towards the sea.

“Started in 1516 on the instructions of Aroudj Barbarossa and enlarged by Mustapha Pasha, the Citadel was originally a military fortress until 1817, the year in which the second-last Dey (ruler) Ali Khodja decided to turn it into his residence and the seat of his government.

“On the arrival of the Dey Hussein as the head of government, the Citadel was rearranged in terms of its new function – that of seat of administration, justice and finance. It consisted of:

- The Palace of the Dey and its outbuildings, at the time divided into a wing reserved for women, apartments for the Dey, meeting halls for the council, kitchens and store rooms
- The mosque of the Dey, reserved for the Dey and his officials
- The palace and baths of the agha
- The palace of the Beys (regional rulers?) and its outbuildings reserved for the Beys of Constantinople, Medea and Oran, who came every three years for the Douches (tribute payable to the Beylik (Chief Dey) by these three provinces)
- The mosque of the guards
- The gunpowder room, which served for the manufacturing of saltpetre and which today is the only architectural example of its kind in Algeria
- The distribution of water

- The gardens (winter and summer)
- The ostrich park
- Five sets of cannons
- The bunkers housing the guards

“Converted into barracks from the start of the French colonisation in 1830, the Citadel was inhabited by the generals of this army until 1840, during which year certain sectors were changed into a military hospital. Classified as a historical monument as from 1887, a section of the Citadel (the palace of the Dey, the mosque of the Dey and the gunpowder room) was converted into a colonial military museum in 1930. With the independence of Algeria in 1962, the entire contents of the museum were removed by the French.

“Today the Citadel is being restored and developed in order to return this historical complex, symbol of the Algerian state before colonisation, to its erstwhile importance”.²

(Supplied by the donor of the tile shard from the Citadel of Algiers)

5.2 Pigment analysis on the Citadel tile

The method of tile pigment analysis that was followed included micro-Raman spectroscopy, X-ray powder diffraction (XRD), Energy dispersive X-ray spectrometry (EDX) and a separate synthesis of related reference compounds to aid in the Raman band assignments and XRD studies.

5.2.1 Yellow pigments

It must be noted that lead-based yellow pigments have been in use³ since 1600. Among the earliest that are known to have been used are the following: lead (II) stannate (Pb_2SnO_4), lead (II) antimonate, often called Naples yellow ($\text{Pb}_2\text{Sb}_2\text{O}_7$), and lead (II) oxides (orthorhombic and tetragonal).³ Despite the fact that these pigments were widely manufactured and used, some of the ancient recipes are not well understood or even known. The detailed study of these ancient pigments is further complicated by the use of less-than-pure starting materials that were peculiar to the areas from which the raw materials were obtained. Table 5.2.1.1 is a summary of these ancient yellow pigments as adapted from the work of Clark.³

Table 5.2.1.1. Summary of the ancient yellow pigments and some of the Raman band assignments (adapted from Clark³)

Compound	λ_o / nm	Wavenumber / cm^{-1}
Pb_2SnO_4	514.5	35wm, 58w, 80m, 129vs, 196m, 274w, 291wm, 379w, 454wm, 524w, 613w,
Pb_3O_4	647.1	121vs, 152m, 223w, 232w, 313w, 391w, 477w, 549s.
$\text{PbSn}_{1-x}\text{Si}_x\text{O}_3$	514.5	40m, 66m, 85(sh), 138vs, 324wm(br), 444w (br).
$\text{Pb}_2\text{Sb}_2\text{O}_7$	514.5	76s, 147vs, 343s, 464m, 513wm,
PbO (massicot orthorhombic, yellow)	647.1	87s, 144vvs, 171(sh), 217vw, 289vs, 385m, 424w.
PbO (Litharge tetragonal, reddish)	647.1	81s, 147vvs, 322vw, 338s

It has been noted that the most common of these yellow pigments have a dominant Raman band at ca 127-145 cm^{-1} and differ from each other by the position of this dominant band (DB) which has been attributed to a Pb-O stretching mode.³ The following differences in the position of this dominant Raman band can be found in these common pigments: lead tin yellow [type I (DB at 129 (vs) cm^{-1} and 196 cm^{-1} (s)) and type II (DB at 138 cm^{-1} (vs) and broad bands at 324 cm^{-1} (m)], lead (II) antimonate [DB at 140 cm^{-1} and broad bands at 329 cm^{-1} (m) and 442 cm^{-1} (w)], two lead (II) oxides [orthorhombic (143 cm^{-1} (vs), 289 cm^{-1} (s) and 385 cm^{-1} (w)) and tetragonal [145 cm^{-1} (vs), 285 cm^{-1} (vw) and 336 cm^{-1} (vw)] crystals.³

On the basis of this introductory information, the yellow pigment on the tile has been studied, identified and characterised.

5.2.1.1 Ancient rediscovered yellow pigment ($\text{Pb}_2\text{SnSbO}_{6.5}$)

Representative Raman spectra of the yellow pigment on the Citadel tile were acquired at many different locations on the tile. The three distinct spectra that were obtained all differed from well-known ancient yellow pigments such as lead tin yellow types I and II, lead antimonate yellow, Naples yellow and other related pigments.^{3,4-6} Interest was not focused exclusively on the Pb-O dominant Raman vibration since it had already been shown that these compounds by and large differ by the position of this band.³ Instead, interest was focused on the entire Raman spectrum within the collected region of 100 cm^{-1} to 1300 cm^{-1} .

It was found that the yellow pigment on the tile is fairly similar to another ancient yellow pigment (pyrochlore type) which was recently identified on Italian paintings of the 16th century by G.B. Langetti (“Lot and his daughters”) and Luca Giordano (“Entrance of Christ in Jerusalem”)⁷ and on Italian pottery of the 16th century.^{8,9} This

pigment can be described as a pyrochlore-type ternary system represented by the formula $\text{Pb}_2\text{SnSbO}_{6.5}$.

Figure 5.2.1.1.1 shows the Raman spectra collected from the yellow sections according to the shade of yellow pigment, using 568 nm wavelength radiation. It is also noted that a similar trend was observed using the 514.5 nm wavelength radiation, showing that the 127 cm^{-1} Raman band is associated with the ternary compound $\text{Pb}_2\text{SnSbO}_{6.5}$.

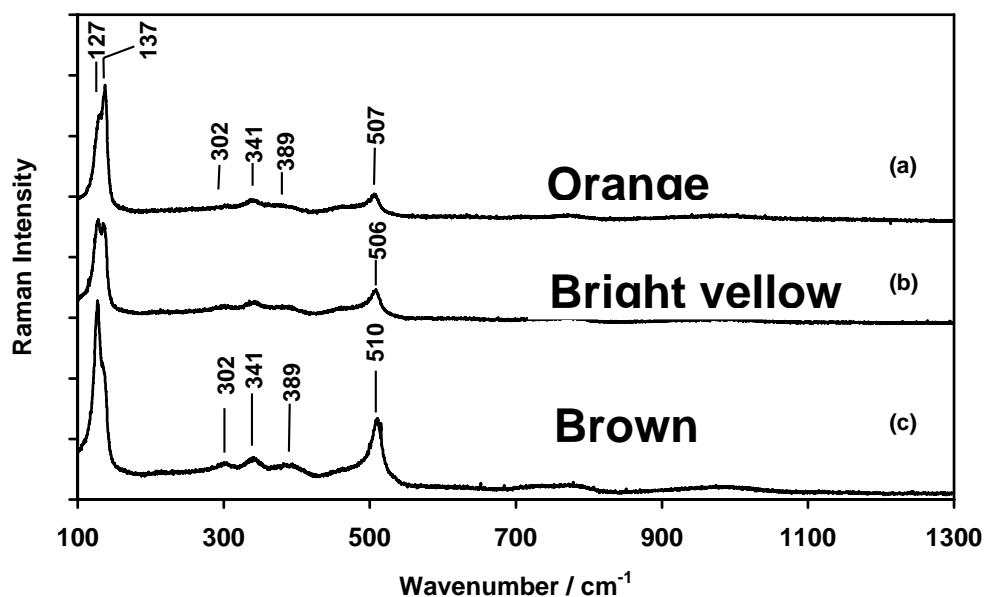


Figure 5.2.1.1.1. This Figure shows spectra of the various shades of yellow pigment with 568 nm wavelength radiation at 0.5 mW at the sample. The wavenumber resolution is 2 cm^{-1}

Since these spectra are similar to the literature assignments but not conclusive, the first task was to determine which spectra among them correspond to this ternary compound and to which pigments the other spectra correspond.

It must also be noted that the literature assignment for the Pb-O Raman band for this ternary yellow pigment ($\text{Pb}_2\text{SnSbO}_{6.5}$) is placed at 132 cm^{-1} ; it is sometimes indicated as $127\text{ cm}^{-1} - 137\text{ cm}^{-1}$ and is shown as a doublet in this region.⁷⁻¹⁰ In this study, three distinct phases (by colour) corresponding to bright yellow, brown-yellow and an orange-yellow making up the yellow section of the Citadel tile were observed. Using the synthesis methods described by Cascales and co-workers¹⁰ for these types of pyrochlore system, several reference samples were synthesised, as described in Chapter 3. XRD data were collected for these samples, as shown in Table 5.2.1.1.1.

Table 5.2.1.1.1. XRD results for synthesised samples, labelled from (a) to (e) according to the ratio of Pb to Sn to Sb (Pb:Sn:Sb)

Sample	Ratio Pb:Sn:Sb	XRD results
(a)	2:1:1	$\text{Pb}_2\text{SnSbO}_{6.5}$ (dominant) PbSb_2O_6 (trace) SnO_2 (starting material)
(b)	Excess Sb	$\text{Pb}_{3+x}\text{Sb}_2\text{O}_{8+x}$ Sb_2O_4 (starting material) PbSb_2O_6
(c)	Excess Sn	$\text{Pb}_2\text{SnSbO}_{6.5}$ (trace) Pb_2SnO_4 SnO_2 (starting material)
(d)	2:1:0	Pb_2SnO_4 (dominant)
(e)	2:0:1	PbSb_2O_6 (dominant)

The following discussion relates the synthesised pigments to those on the Citadel tile. The use of Raman spectra in conjunction with XRD data for samples (a) and (e) revealed that the dominant Pb-O Raman band for the ternary pyrochlore-type pigment ($\text{Pb}_2\text{SnSbO}_{6.5}$) is at 127 cm^{-1} rather than at the 132 cm^{-1} reported in the literature.⁷⁻⁹ Figure 5.2.1.1.2 is the Raman spectrum of the synthesised pigment resulting from starting materials containing Pb:Sn:Sb = 2:1:1.

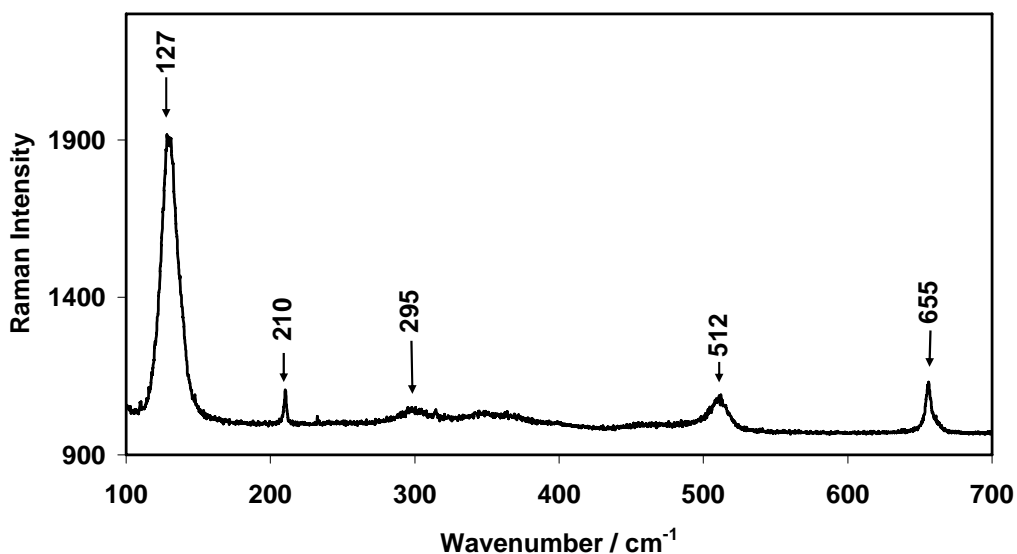


Figure 5.2.1.1.2. Raman spectrum of sample (a) in Table 5.2.1.1.1. The Raman bands at 210 cm^{-1} and 655 cm^{-1} are assigned to trace amounts of rosielite (PbSb_2O_6). A 514.5 nm wavelength radiation, 0.3 mW laser power at the sample, with 2 cm^{-1} wavenumber resolution was used

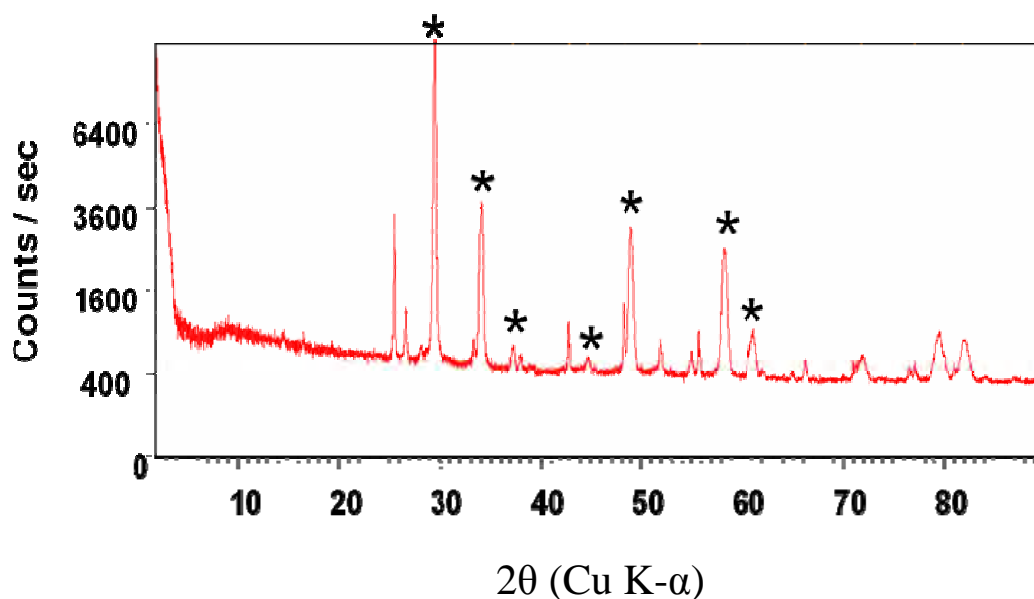


Figure 5.2.1.1.3. The XRD pattern of sample (a) in Table 5.2.1.1.1, shows the ternary pyrochlore as the dominant product. The asterisks are used to show the ternary compound ($\text{Pb}_2\text{SnSbO}_{6.5}$)

This spectrum was compared with those of the various yellow pigments on the tile shard (Figure 5.2.1.1.1). The literature spectrum of the ternary pigment ($\text{Pb}_2\text{SnSbO}_{6.5}$) is reported by Ruiz-Moreno and co-workers⁷ and Sandalinas and co-workers^{8,9} to sometimes have a doublet at 127 cm^{-1} and 137 cm^{-1} . A comparison with the product prepared in this laboratory, with a ratio of $\text{Pb}:\text{Sn}:\text{Sb} = 2:1:1$ presumed to be this ternary pigment, shows only one single band at 127 cm^{-1} .

In order to verify whether the prepared pigment is indeed the ternary compound $\text{Pb}_2\text{SnSbO}_{6.5}$, an XRD spectrum was obtained and indeed the XRD data for the synthesised sample shown in Figure 5.2.1.1.3. do indicate that the ternary pigment $\text{Pb}_2\text{SnSbO}_{6.5}$ is the dominant component, with small amounts of rosielite (PbSb_2O_6).

The Raman bands at 210 cm^{-1} and 655 cm^{-1} that are also present in Figure 5.2.1.1.2. are attributed to PbSb_2O_6 (rosiaite). A compound prepared with $\text{Pb}:\text{Sn}:\text{Sb} = 1:0:2$, as in Table 5.2.1.1.1 row (e), was confirmed to yield PbSb_2O_6 (rosiaite) as a dominant product. The Raman spectrum of the synthesised rosiaite (Table 5.2.1.1.1 row (e)) is shown in Figure 5.2.1.1.4. As expected, the two Raman bands attributed to rosiaite at 210 cm^{-1} and 665 cm^{-1} are now most intense, confirming that the product in Table 5.2.1.1.1 row (e) is indeed PbSb_2O_6 (rosiaite). The XRD results of the synthesised rosiaite as shown in Figure 5.2.1.5 also confirm that the dominant compound in the synthesised sample of Table 5.2.1.1.1.(e) is indeed rosiaite.

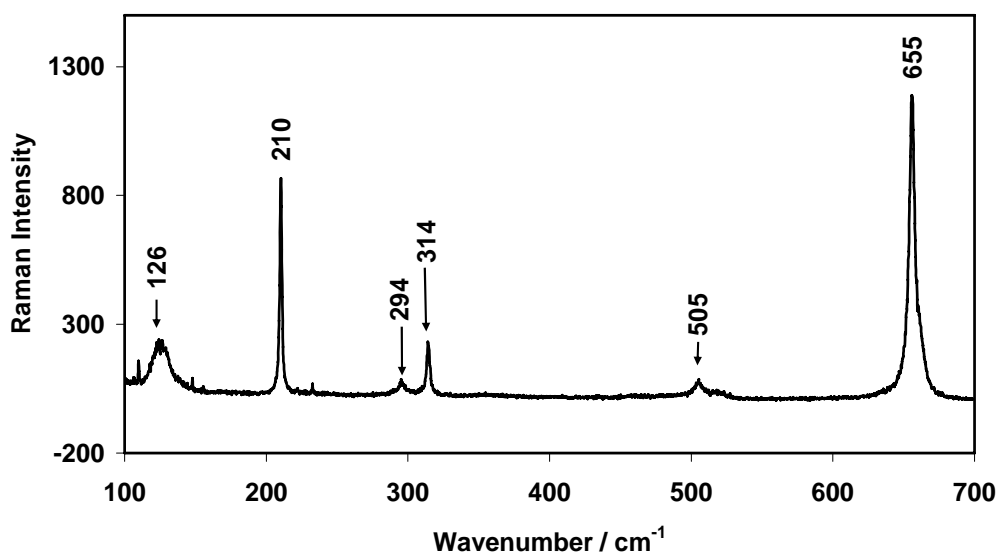


Figure 5.2.1.1.4. The Raman spectrum of sample (e) in Table 5.2.1.2. is consistent with the XRD data. This sample shows two sharp Raman bands at 210 cm^{-1} and 655 cm^{-1} characteristic of PbSb_2O_6 , in addition to the other Raman bands.

In addition to rosiaite (PbSb_2O_6), an unknown component ($\text{Pb}_{3+x}\text{Sb}_2\text{O}_{8+x}$) was also detected in the product (see also sample (b), Table 5.2.1.1.1). The XRD pattern (Figure 5.2.1.1.5) is also consistent with the Raman results

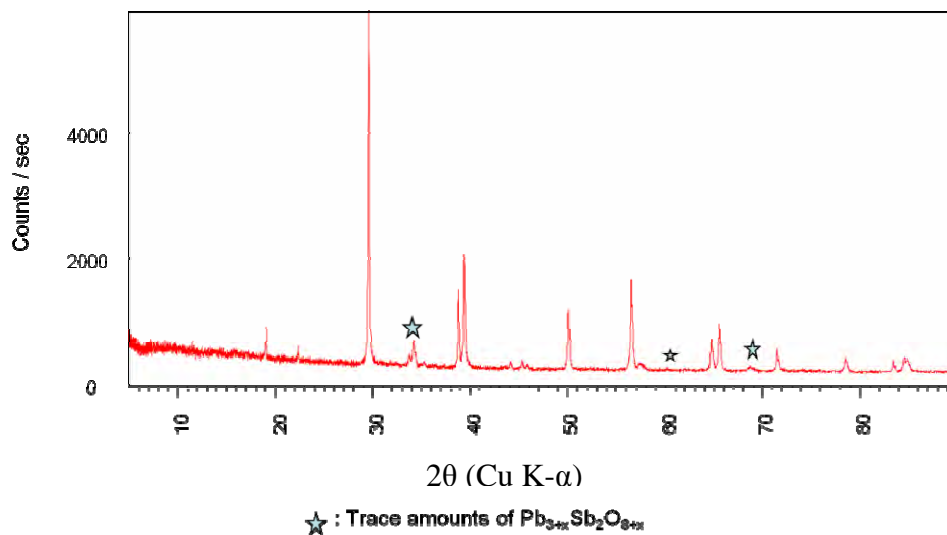


Figure 5.2.1.1.5. XRD pattern of the synthetic rosiate (PbSb_2O_6) with trace amounts of the unknown compound $\text{Pb}_{3+x}\text{Sb}_2\text{O}_{8+x}$ indicated with a star

Figure 5.2.1.1.6 shows the Raman spectrum of a compound prepared with a ratio of Pb:Sn:Sb = 2:1:0 (no antimony), identified as Pb_2SnO_4 .

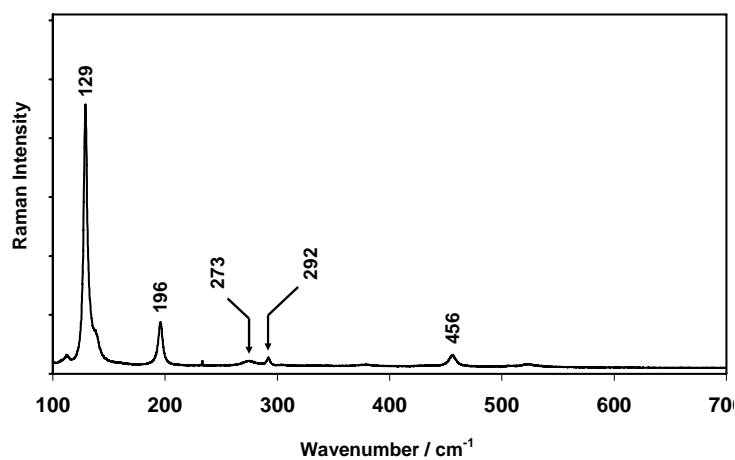


Figure 5.2.1.1.6. Raman spectrum of sample (d) in Table 5.2.1.2, consistent with Pb_2SnO_4 (see also row one of Table 5.2.1.1 from Clark³ for the Raman band assignments for this compound)

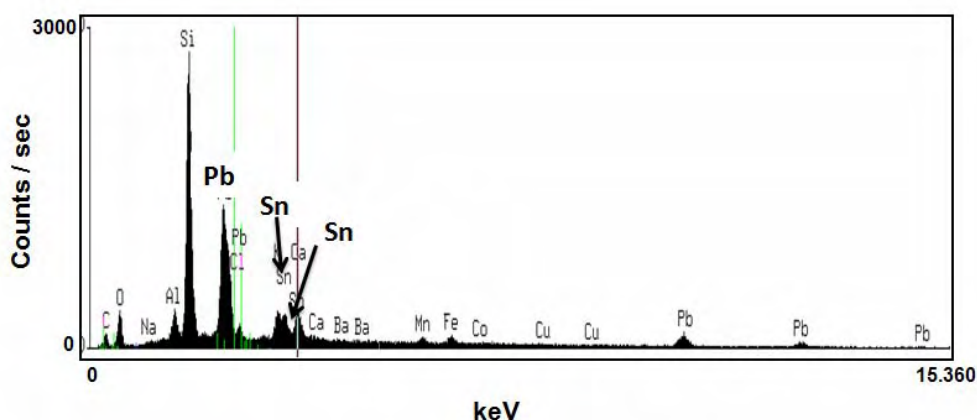


Figure 5.2.1.1.7. EDX spectra of the brown line on the Citadel tile. The ratio of Pb:Sn = 2.19 is close to that of Pb_2SnO_4 . The sample penetration depth is in the order of 20 μm

This compound also appears as the dominant component in a sample prepared with an excess of tin over antimony (see Figure 5.2.1.1.1). The ternary compound ($\text{Pb}_2\text{SnSbO}_{6.5}$) and the starting material (SnO_2) also appear as trace components. This information points to the dominant Pb-O Raman band for this sample being around 129 cm^{-1} .

It is therefore concluded that the compound prepared according to a Pb:Sn ratio of 2:1 in Table 5.2.1.1.1(c) is lead (II) stannate (Pb_2SnO_4). It must be noted that the EDX results also depend on the beam penetration into the glaze and may give larger errors due to underlying material. The large amount of silicon in Figure 5.2.1.1.7 is due to the underlying glaze. The Raman results for lead (II) stannate on the Citadel tile show a mixture of pigments that can be assigned to the lead tin yellow type II ($\text{PbSn}_{1-x}\text{Si}_x\text{O}_3$) shown in Figure 5.2.1.1.8.

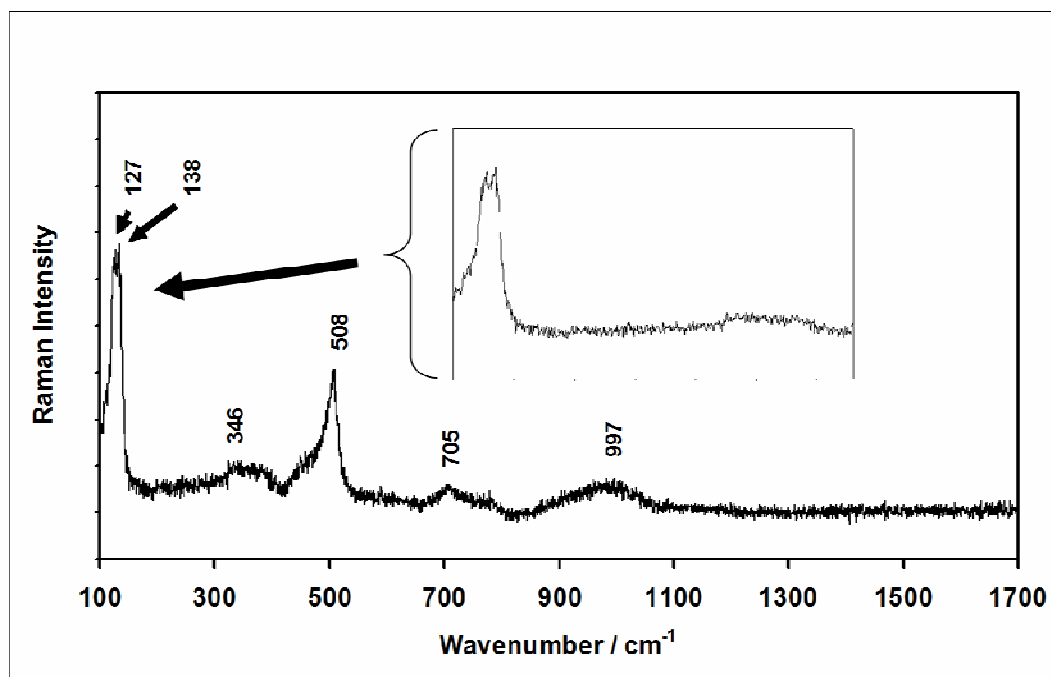


Figure 5.2.1.1.8. Raman spectrum of the tile pigment showing the presence of lead tin yellow type II ($\text{PbSn}_{1-x}\text{Si}_x\text{O}_3$) on the tile shard

It is therefore concluded that the ternary pyrochlore ($\text{Pb}_2\text{SnSbO}_{6.5}$) on the tile shard is the brownish yellow pigment with the dominant Pb-O vibration at 127 cm^{-1} and not the bright yellow pigment normally found on Italian paintings of the 16th century with its dominant Pb-O Raman band at 132 cm^{-1} . It appears that this bright yellow pigment consisted of mixtures of pigments, including the ternary pyrochlore structure ($\text{Pb}_2\text{SnSbO}_{6.5}$) and tin-rich lead stannate (Pb_2SnO_4). These mixtures sometimes contained silica and even rock salt as flux to produce the desired hue.⁷

EDX data were obtained for the different sections of the tile pigments. Although EDX data may not be accurate due to the possibility of including up to $20\text{ }\mu\text{m}$ of underlying sections, they can nevertheless, be an estimate of the element ratios on the various colour backgrounds on the Citadel tile. Typical EDX results are shown in Appendix 5.1.

5.2.1.2 Naples yellow or lead antimonite ($\text{Pb}_2\text{Sb}_2\text{O}_7$)

Naples yellow or lead antimonate yellow ($\text{Pb}_2\text{Sb}_2\text{O}_7$) is the most common of the yellow pigments used by the western European artists¹¹ from about 1500 to 1850. The identification of this pigment on a tile from the Citadel of Algiers produced in 1516 indicates the availability and use of this pigment in the Mediterranean region very early on during this period. This may support the assertion that this pigment originates from the Middle Eastern ceramic and glass industries of the 15th century and that the know-how on the production of lead antimonite yellows was transferred via the migration of glass artists from the eastern Mediterranean to Venice during the 15th century.¹¹ Figure 5.2.1.2.1 shows the Raman spectrum of the reddish-brown yellow pigment on the tile shard. The two strong Raman bands at 140 cm^{-1} and 510 cm^{-1} are consistent with literature assignments for Naples yellow.¹²

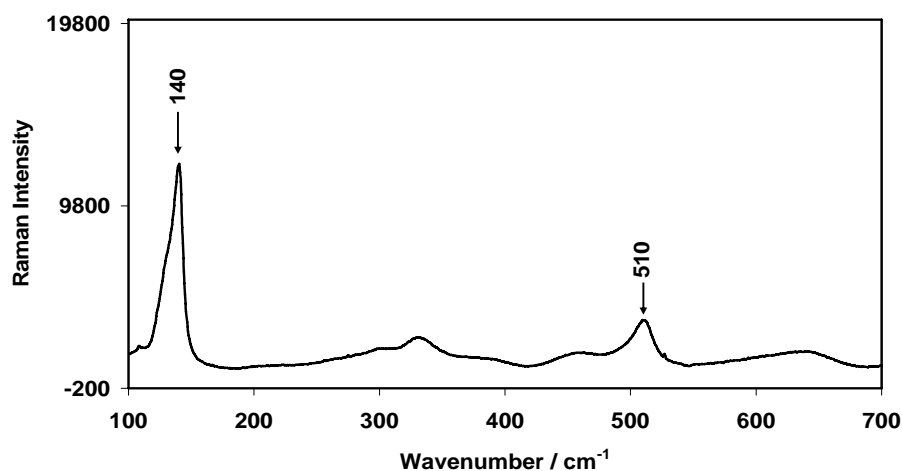


Figure 5.2.1.2.1. Naples yellow Raman spectrum as identified on the Citadel tile. The wavelength of the excitation line was 514.5 nm and the power at source was 0.5 mW

The EDX results obtained directly on this pigment from the tile shard also show ratios of $\text{Pb}:\text{Sb} = 1:1$. These ratios are determined by noting that the weight

percentages given by EDX results are simply averages of atomic concentrations in the path of the beam and can therefore be used to determine the approximate ratios of atoms using the same data set. These results are also consistent with the formula $\text{Pb}_2\text{Sb}_2\text{O}_7$ that has been determined for Naples yellow.³ Figure 5.2.1.2.2 is representative of the EDX spectra that were used to generate the table in Appendix 5.1, in this case for the white section of the tile shard.

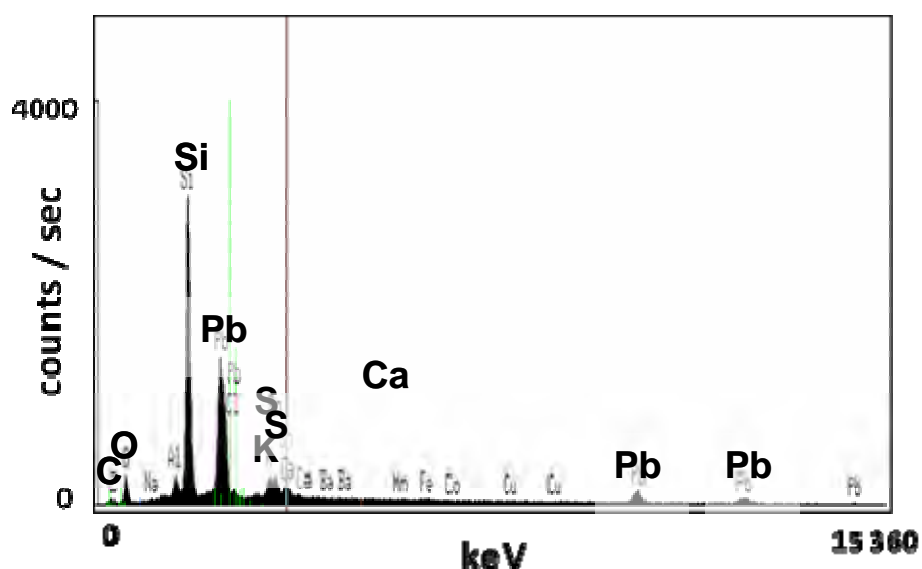


Figure 5.2.1.2.2. Representative EDX spectra on the white section of the tile. Similar EDX spectra and associated information were used to generate tables, such as that of Appendix 5.1

5.2.1.3 White pigment: cassiterite (SnO_2)

The glaze on the Citadel tile is composed largely of cassiterite (SnO_2). Raman spectra from this white pigment shown in Figure 5.2.1.3.1(a) were compared with those of a reference compound (Figure 5.2.1.3.1(b)) purchased from Merck, Johannesburg. The cassiterite structure belongs to the tetragonal crystal system with two molecules per unit cell, $P_{4/2mm}$ (D_{2h}^{14}) space group.¹³⁻¹⁴

From consideration of group theory, four Raman-active bands are given as A_{1g} , B_{1g} , B_{2g} and E_g . Two of the Raman bands that are observed (Figure 5.2.1.3.1) may be assigned as the 635 cm^{-1} (A_{1g}) and 799 cm^{-1} (B_{2g}) Raman bands.¹⁵ Due to the broad bands around 500 cm^{-1} and 1000 cm^{-1} , the cassiterite Raman band around 513 cm^{-1} observed in the reference spectrum is not observed in the tile spectrum. However, the two Raman bands observed and their relative intensity are sufficient to identify this white pigment as cassiterite (SnO_2).

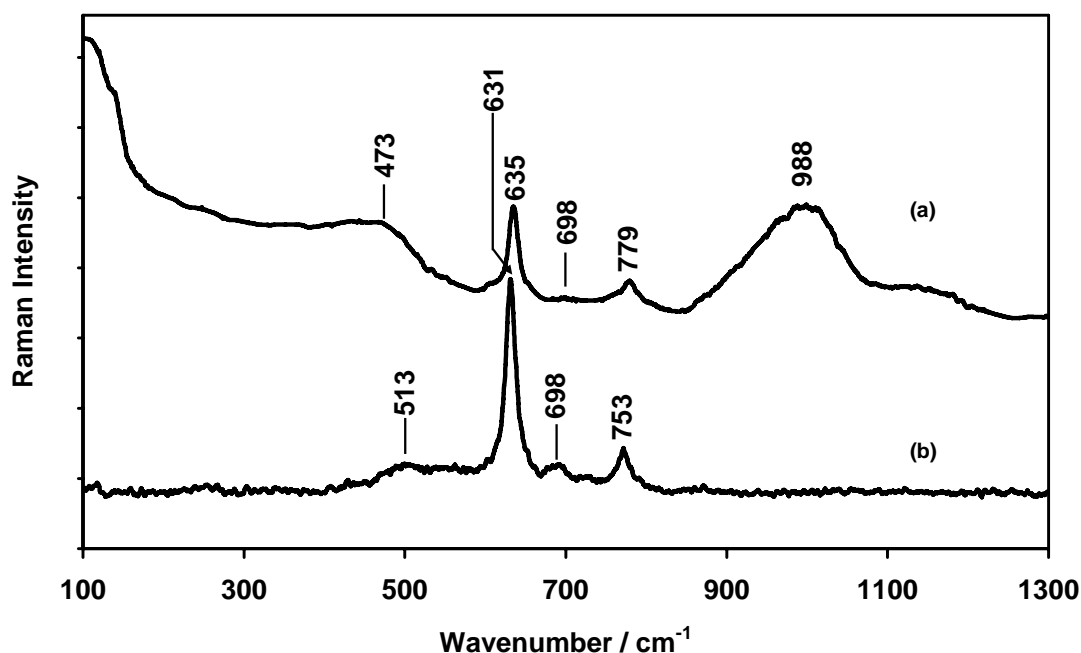


Figure 5.2.1.3.1. Two Raman bands for white pigment: the spectrum in (a) is that from the white pigment on the Citadel tile and (b) is that of a reference compound SnO_2

Historically, cassiterite was used as an opacifier¹⁵ and in some instances it has been found mixed in with α -quartz in ceramic materials from the period 1510–1530 in Iznik (former Nicaea).¹⁶ It is conceivable that this was also the intention here since the Citadel of Algiers was built in 1516. Using the glaze depth profiles generated by

Raman spectra, it was possible to show that some amorphous carbon is found inside the glaze of the tile and not on the surface of the tile as indicated in Figure 5.2.1.3.2. In this figure, the top spectrum (a) is that collected at the surface of the glaze (0 μm), while the bottom spectrum (e) was collected at 30 μm inside the glaze. It is also concluded that this amorphous carbon may be due to contamination at the time of manufacture of the Citadel tile.

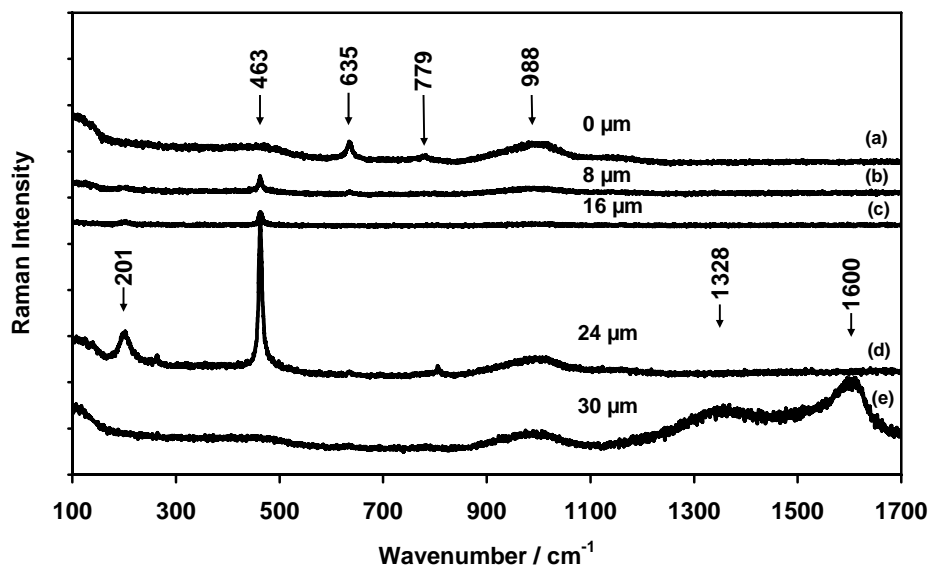


Figure 5.2.1.3.2. Glaze depth profile spectra generated on the white background of the Citadel tile, also showing amorphous carbon at a depth of 30 μm

5.2.1.4 Blue pigment: cobalt aluminium oxide (CoAl_2O_4)

Figure 5.2.1.4.1 shows a high-resolution picture (100X magnification) of the blue background on the glaze of the Citadel tile shard. The blue pigment is seen to be spread homogeneously through the glaze. However, repeated glaze depth profile Raman spectra on the blue background did not reveal the identity of the blue pigment. Figure 5.2.1.4.2 shows this profile and reveals only cassiterite and quartz.

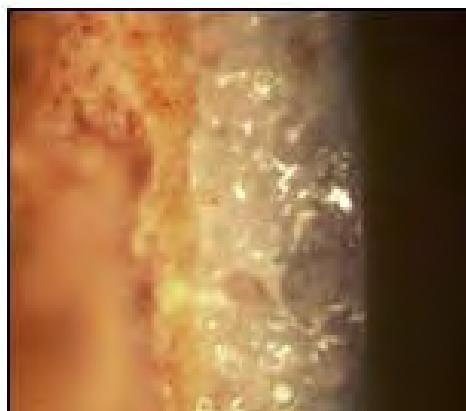


Figure 5.2.1.4.1. The cross-section of the blue background from the tile shard is shown. The blue pigment is shown spread homogeneously through the top section of the tile shard and could be the result of dissolved cobalt

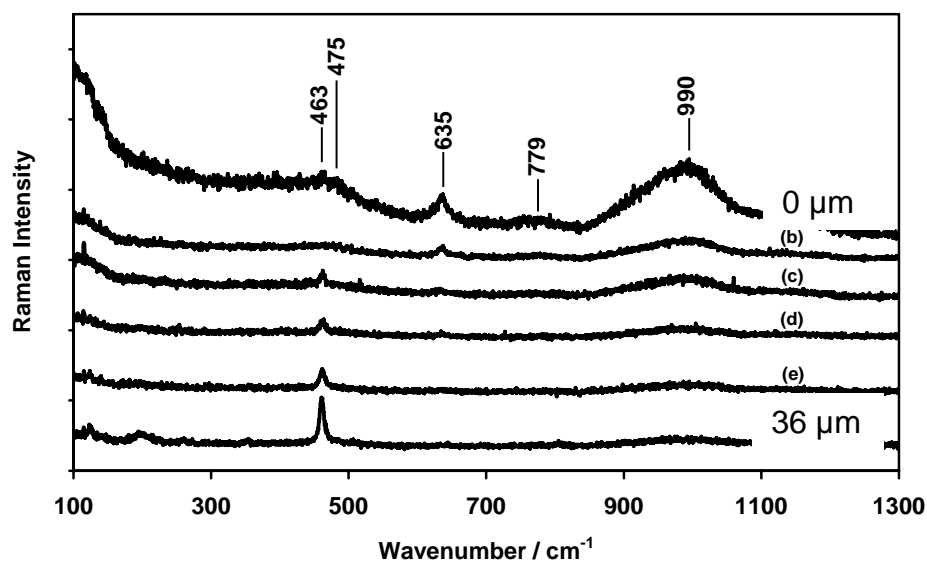


Figure 5.2.1.4.2. Glaze depth profile Raman spectra, which does not show the identity of the blue colour but shows that cassiterite and quartz form part of the glaze. However, it has been shown elsewhere¹⁷ that dissolved cobalt can give a distinct blue colour while remaining undetected.

It is customary to use the concept of scattering cross-section when scattering efficiencies are considered. In the case of the cobalt entity in the glaze of the tile, we sought only to show that due to low scattering efficiency and the small scattering cross-section, this cobalt entity in the tile glaze may be undetected. The Raman signal intensity depends on a number of factors, among which are the following: molecular density (ρ); sample thickness; and the first differential Raman cross-section ($d\sigma/d\Omega$), which is itself dependent on the excitation radiation to the inverse fourth power ($1/\lambda^4$), where $d\Omega$ is the solid angle defining the scattered photon flux.

The proportionality of the Raman signal intensity can be represented by the following expression:^{18,19}:

$$\frac{d\sigma}{d\Omega} \times \rho \times \int_0^D 10^{-(\alpha_e + \alpha_R)} dr \quad 5.1$$

where

- $\frac{d\sigma}{d\Omega}$ ■ differential Raman cross-section
- α_e ■ absorptivity at a reference wavelength
- α_R ■ absorptivity at the Raman line
- ρ ≡ molecular density
- D ■ sample thickness

where the triple lines indicate equivalency.

Firstly, despite the intense bright blue colour on the tile, the molecular density could be very low. Secondly, sample thickness in the glaze is in the order of $< 1 \mu\text{m}$ due to the use of confocal Raman configuration. Thirdly, the first differential Raman cross-sections ($d\sigma/d\Omega$) are in the order of $\approx 10^{-31} - 10^{-28} \text{ cm}^2 \text{ sr}^{-1}$ and there are therefore lower limits of detection for Raman spectroscopy.²⁰ Therefore, if the pigment concentration in the glaze is orders of magnitude smaller than the lower limits, for example comparable to molecular mono-layers within the sampled volume, then the pigment in the glaze will be undetectable without any form of signal enhancement such as surface enhanced Raman spectroscopy (SERS) or resonance effects. For instance, silver nanocrystals could have been spread on the surface of the glaze to come into contact with the surface, in which case a Raman spectrum of the surface in contact with the silver particles would be obtained. Alternatively, the transparency to Raman spectroscopy of the blue colour in this glaze could be the result of dissolved cobalt ions in the glass structure.¹⁷

However, a small amount of pigment was detected in crevices in the glaze and a spectrum was recorded and identified as cobalt blue or cobalt aluminium oxide.²¹ Due to the fact that cobalt blue was not directly observed in the bulk of the glaze using Raman spectroscopy, it may be advisable to conduct further research using other techniques to identify conclusively the exact cobalt structure that is giving rise to this beautiful blue colour in the glaze (Figure 5.2.1.4.1).

5.3 Tile body analysis

The body of the tile appears red/brown in colour but appears to be rather heterogeneous with black, red/brown and white particles showing under the microscope. These particles were analysed directly using low-power radiation (5 mW of 514.5 nm radiation at the source). The chemical composition of the tile body will now be discussed.

5.3.1 Iron oxides

5.3.1.1 Hematite ($\alpha\text{-Fe}_2\text{O}_3$)

Figure 5.3.1.1.1 (a) shows the Raman spectrum collected from the black/brown particles on the tile body. The observed spectrum is shown to be that of hematite. All seven Raman-active bands of hematite that are predicted by group theory ($2A_{1g} + 5E_g$) were observed. The assignment of these Raman bands follows directly from the literature²² as 226 cm^{-1} (A_{1g}), 247 cm^{-1} (E_g), 292 cm^{-1} (E_g), 411 cm^{-1} (E_g), 607 cm^{-1} (E_g) and 496 cm^{-1} (A_{1g}), and the magnon band observed at 1330 cm^{-1} . The 298 cm^{-1} (E_g) is seen only as a shoulder on the 292 cm^{-1} band (Figure 5.3.1.1.1(a)), consistent with observations in other studies.^{22,23}

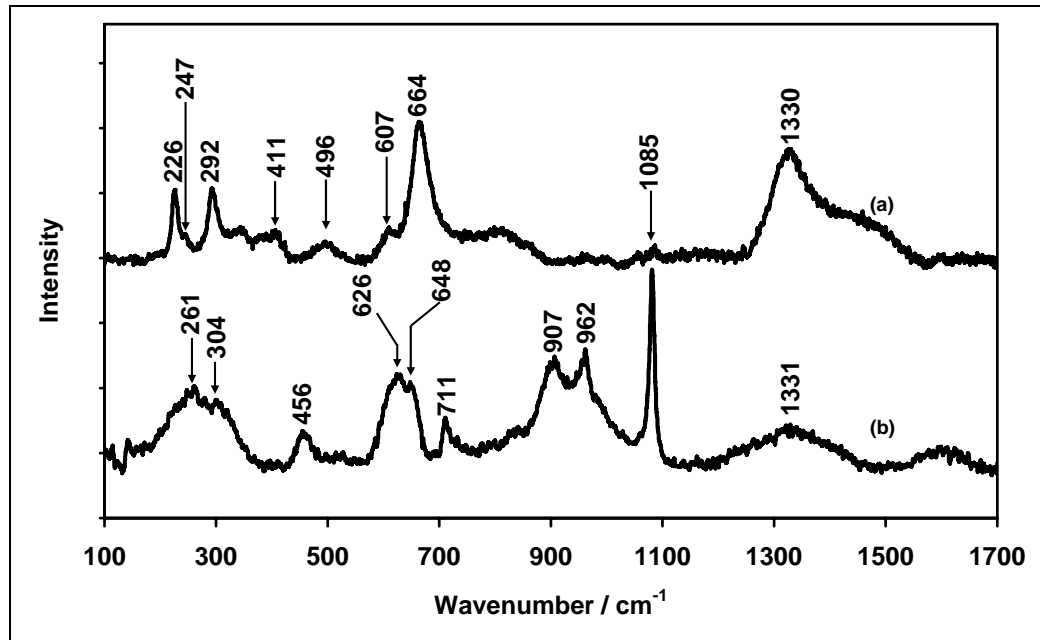


Figure 5.3.1.1.1. The presence of hematite ($\alpha\text{-Fe}_2\text{O}_3$) is indicated by the observation of all the hematite Raman bands in Figure 5.3.1.1.1(a)

5.3.1.2 Maghemite ($\gamma\text{-Fe}_2\text{O}_3$)

Maghemite ($\gamma\text{-Fe}_2\text{O}_3$) has an inverse spinel structure which appears as an Fe-deficient form of magnetite.¹⁶ However, its Raman spectrum is not well defined²⁴ and it is known to be characterised by broad features around 350 cm^{-1} , 500 cm^{-1} and 700 cm^{-1} as can also be seen in this study (Figure 5.3.1.1.1(b)). It must be noted that the broad features identified in the maghemite spectrum are not present in any of the other iron oxides or oxyhydroxides²⁵ that are usually found in clays.

5.3.1.3 Magnetite (Fe_3O_4)

The presence of magnetite (Fe_3O_4) in the body of the tile could have come from the raw material that was used. Magnetite occurs naturally in clay bodies²⁵ and its presence in the tile would not be a surprise if it is assumed that the raw material was a naturally occurring clay. Indeed, Figure 5.3.1.1.1(a) shows a relatively strong Raman band at 664 cm^{-1} that is not part of the $\alpha\text{-Fe}_2\text{O}_3$ spectrum. No other iron oxide shows this Raman band, except würozite (FeO), in which it is usually broad and shifted to lower wavenumbers.²³ This phase is therefore attributed to magnetite.²⁶

5.3.2 Quartz ($\alpha\text{-SiO}_2$)

Two forms of quartz were identified on the tile. Figure 5.3.4.1(b) shows a strong A_{1g} mode of $\alpha\text{-SiO}_2$ at 464 cm^{-1} and a broad Raman band attributed to glassy silica at 459 cm^{-1} .

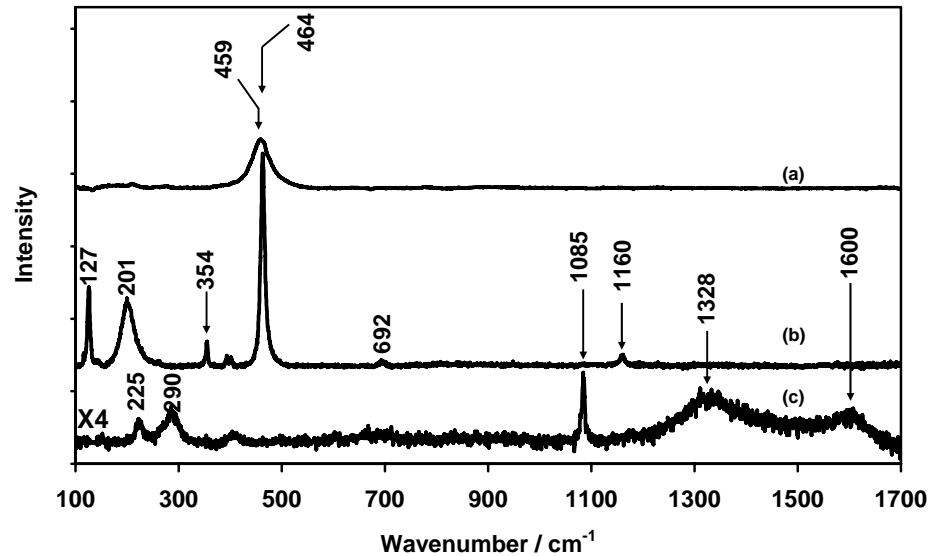


Figure 5.3.4.1. Both glassy silica (a) and quartz (b) were detected on the body of the tile. Amorphous carbon and traces of calcite were also detected as shown in (c)

These phases appear as white crystalline materials embedded in the body of the tile and may have been part of the original material of manufacture of the tile.

5.3.3 Calcite (CaCO₃)

Calcite (CaCO₃) was detected in the body of the Citadel tile and is identified by the two Raman bands at 1085 cm⁻¹ (A_{1g}) and 711 cm⁻¹ (E_g)^{27,28} (see Figure 5.3.1.1.1(b)). There are two other forms of CaCO₃ and both show a strong Raman band around 1085 cm⁻¹. However, these two other phases (aragonite and vaterite) also show additional Raman bands at 700 cm⁻¹ and 750 cm⁻¹, respectively.²⁷ Therefore the phase in the body of the tile is positively identified as calcite.

5.3.4 Amorphous carbon

The glaze of this tile did not show any presence of amorphous carbon on the surface, except for trace amounts inside the glaze (Figure 5.2.1.3.2(e)) and the body of the tile (Figure 5.3.4.1(c)). The amorphous carbon detected in both cases is presumed to be due to accidental contamination during the manufacture of the tile. This contamination is identified by two broad bands around 1350 cm^{-1} and 1600 cm^{-1} and these bands are associated with the “D” and “G” Raman bands of graphitic carbon.^{29,30} A high-resolution photo of these inclusions is shown in Figure 5.3.6.1.

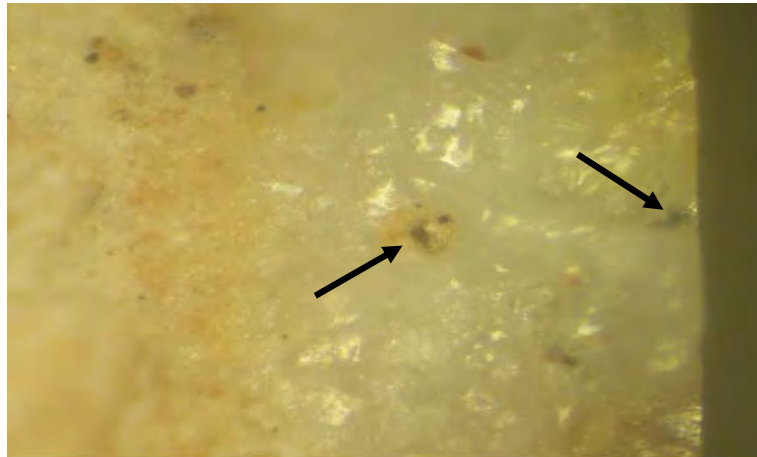


Figure 5.3.6.1. Amorphous carbon inclusions found in the glaze and presumed to be contamination that occurred during the manufacturing process. This photo was acquired with an Olympus camera mounted on top of the microscope using a 50X objective lens

5.4 Implications for restoration and preservation

The valuable information obtained from the study of the Citadel tile shard could be used for purposes of restoration and preservation of the Citadel itself. First, all the

pigments that were used have been positively identified. Secondly, the composition of the body of the tile has been determined, based on its major components. The direction of research for additional information to assist in the restoration process should include, among others, the manufacturing recipes of that time (~ 1615) for the various pigments and body material, and the raw material supply for the specific components (glaze, body or pigment).

5.5 Conclusion

The characterisation of the pigments and body of the tile shard from the Citadel of Algiers was accomplished by using micro-Raman spectroscopy as the major technique, complemented by powder X-ray diffraction (XRD) and energy-dispersive X-ray spectrometry(EDX). The results reveal a rich variety of pigments which include the newly rediscovered ternary yellow pigment ($\text{Pb}_2\text{SnSbO}_{6.5}$), Naples yellow ($\text{Pb}_2\text{Sb}_2\text{O}_7$), lead (II) stannate (Pb_2SnO_4), rosiaite (PbSb_2O_6), cassiterite (SnO_2) and cobalt blue (CoAl_2O_4).

The body of the tile is composed largely of hematite ($\alpha\text{-Fe}_2\text{O}_3$), maghemite ($\gamma\text{-Fe}_2\text{O}_3$), magnetite (Fe_3O_4), quartz ($\alpha\text{-SiO}_2$), glassy silica and traces of calcite (CaCO_3) and amorphous carbon.

The accumulated chemical information may be used in conjunction with information on preparation and raw material sources to design an appropriate restoration and conservation response programme for these ancient tiles. Micro-Raman spectroscopy proved to be very useful in pigment characterisation when used in conjunction with complementary techniques such as XRD and EDX.

5.6 References

1. Kock, L.D. and de Waal, D. *Spectrochim Acta Part A*. 2008, **71**, 1348.
2. De Waal, D. Tile shard donated for Raman Spectroscopy studies in the Department of Chemistry, University of Pretoria. 2006.
3. Clark, R.J.H., Cridland, L., Benson, M., Kariuki, K.D.M., Harris, D.M. and Withnall, R. *J. Chem. Soc. Dalton Trans.* 1995.
4. Kühn, H. In: *Artists Pigments*, Vol. 2, A. Roy (ed.), Oxford, Oxford University Press, 1994.
5. Martin, E. and Duval, A.R. *Stud. Conserv.* 1990, **35**, 117.
6. Wainwright, N.M., Taylor, J.M. and Harley, R.D. In: *Artists' Pigments*, Vol. 1, R.L. Feller (ed), Cambridge, Cambridge University Press, 1986, p 219.
7. Ruiz-Moreno, S., Perez-Pueyo, R., Gabaldon, A., Soneira, M-J. and Sandalinas, C. *J. Cultural Heritage*. 2003, **4**, 309s.
8. Sandalinas, C. and Ruiz-Moreno, S. *Studies in Conservation*. 2004, **49**, 41.
9. Sandalinas, C., Ruiz-Moreno, S., Lopez-Gill, A. and Miralles, J. *J. Raman Spectrosc.* 2006, **37**, 1146.
10. Cascales, C., Alonso, J.A. and Rasines, I. *J. Mater. Sci. Lett.* 1986, **5**, 675.
11. Dik, J., Hermens, E., Peschar, R. and Schenk, H. *Archaeometry*. 2005, **47**, 593.
12. Edwards, H.G.M. *J. Raman Spectrosc.* 2004, **35**, 656.
13. Katiyar, R.S. and Krishnan, R.S. *Phys. Lett.* 1967, **25A**, 525.
14. Ocaña, M., Serna, C.J., Garcia-Ramos, J.V. and Matijević, E. *Solid State Ionics*. 1993, **63**, 170.
15. Yu, K.N., Xiong, Y., Liu, Y. and Xiong, C. *Phys. Rev.* 1997, **55**, 2666.
16. Colomban, P., Milande, V. and Le Bihan, L. *J. Raman Spectrosc.* 2004, **35**, 527.

17. Colombaro, P., de Laveaucoupet, R. and Milande, V. *J. Raman Spectrosc.* 2005, **36**, 857.
18. Christesen, S., Gonser, K., Lochner, J.M., Sedlacek, A., Chyba, T., Sink, D., Pendell Jones, J., Corrado, B. and Slaterbeck, A. *UV Raman Detection Of Chemical Agents*. Naval Surface Warfare Center, Dahlgren, Virginia USA, 2004.
19. Long, D.A. *The Raman Effect*. New York, Wiley, 2002.
20. Pettinger, B., Ren, B., Picardi, G., Schuster, R. and Ertl, G. 2005, **36**, 541.
21. De Waal, D. *Asian Chem. Lett.* 2004, **8**, 57.
22. De Faria, L.A., Silva, S.V. and de Oliveira. M.T. *J. Raman Spectrosc.* 1997, **28**, 873.
23. Burgio, L. and Clark, R.J.H. *Spectrochim. Acta.* 2001, **57**, 1491.
24. Mortimore, J.L., Marshall, L-JR., Almond, M.J., Hollins, P. and Matthews W. *Spectrochim. Acta.* 2004, **60A**, 1179.
25. Legodi, M.A. and de Waal, D. *Spectrochim. Acta Part A.* 2007, **66**,135.
26. Orlianges, J.C., Champeaux, C., Catherinot, A., Merle, Th. and Angleraud, B. *Thin Solid Films.* 2004, **453**, 285.
27. Nakamoto, K. *Infrared and Raman Spectra of Inorganic and Coordination Compounds*, Part A, Theory and Applications in Inorganic Chemistry, New York, Wiley, 1997, p 138.
28. Mammone, J.F., Nicol, M. and Sharma, S.K. *J. Phys. Chem. Solids.* 1981, **42**, 379.
29. Ristić, M., Ivanda, M., Popović, S. and Musić, S. *J. Non-Crystall. Solids.* 2002, **303**, 270.
30. Kawashima, Y. and Katagiri, G. *Phys. Rev.* 1995, **B14**, 52.

Appendix 5.1

EDX data: Yellow section of Citadel tile

University of Pretoria etd – Kock, L.D. (2009)

Elements	Wt% Sec 1	Wt% Error	Wt% Sec 2	Wt% Error	Wt% Sec 3	Wt% Error	Wt% Sec 4	Wt% Error	Wt% Sec 5	Wt% Error	Wt% Sec 6	Wt% Error	Wt% Sec 7	Wt% Error
Na	0.45	0.08	0.34	0.08	0.19	0.07	0.32	0.08	0.17	0.06	0.26	0.08	0.18	0.07
Mg	0.33	0.06	0.15	0.06	0.12	0.06	0.18	0.06	0.04	0.06	0.08	0.06	0.16	0.05
Al	3.00	0.13	2.43	0.12	2.08	0.12	2.59	0.12	1.77	0.11	2.22	0.11	1.98	0.11
Si	22.48	0.21	22.05	0.21	22.47	0.20	21.61	0.20	21.85	0.19	20.88	0.19	17.04	0.17
P	0.48	0.08	0.20	0.08	0.14	0.08	0.26	0.08	0.00	0.00	0.14	0.07	0.15	0.07
S	0.00	0.00	0.00	0.00	0.00	0.00	0.00	0.00	0.00	0.00	0.00	0.00	0.00	0.00
Cl	0.41	0.16	0.58	0.16	0.62	0.15	0.53	0.15	0.28	0.15	0.30	0.15	0.10	0.14
K	3.99	0.16	3.28	0.23	3.17	0.16	4.03	0.15	2.90	0.14	3.44	0.21	2.45	0.03
Ca	4.12	0.17	1.69	0.14	1.64	0.15	2.35	0.14	1.41	0.13	1.57	0.13	0.87	0.12
Mn	0.16	0.17	0.09	0.17	0.00	0.00	0.07	0.17	0.03	0.15	0.00	0.00	0.08	0.15
Fe	1.49	0.19	1.05	0.19	2.33	0.19	1.02	0.18	0.96	0.17	0.75	0.17	3.00	0.18
Co	0.00	0.00	0.26	0.20	0.15	0.19	0.00	0.00	0.32	0.19	0.14	0.19	0.00	0.00
Cu	0.14	0.26	0.17	0.26	0.29	0.25	0.38	0.25	0.31	0.25	0.20	0.23	0.24	0.23
Pb	59.36	3.54	61.80	3.56	58.15	3.50	60.47	2.34	63.78	2.28	64.65	3.35	67.71	2.19
Ti	0.00	0.00	0.04	0.11	0.05	0.10	0.01	0.13	0.00	0.00	0.00	0.00	0.11	0.11
Cr	0.00	0.00	0.00	0.00	0.00	0.00	0.00	0.00	0.00	0.00	0.10	0.11	0.09	0.11
Sn	0.54	0.60	2.05	0.50	3.46	0.57	1.20	0.47	2.56	0.44	1.37	0.46	0.69	0.40
Sb	3.06	0.81	3.82	0.37	5.15	0.76	4.59	0.36	3.21	0.34	3.91	0.34	4.53	0.31
Ba	0.00	0.00	0.00	0.00	0.00	0.00	0.41	0.31	0.42	0.24	0.00	0.00	0.62	0.28

Chapter 6

Glaze analysis of shards and plates

Probing pigments successfully through the glaze using micro-Raman spectroscopy for the first time necessitates the detailed study of the glaze through which the incident laser beam travels and the Raman scattered radiation passes before detection. Among the properties that will be investigated are: (1) type of glaze: for example SiO_2 or SnO_2 ; (2) element type and relative concentration in the glaze; (3) possible melting temperature of the glaze based on the methods of Colombari and co-workers;¹⁻⁵ and (4) level and type of technology employed by the manufacturers. Based on the results from the analysis, comparisons will be made with samples whose manufacturers and, to some extent, manufacturing technology are known. Differences and/or similarities can then be used to group or exclude samples according to likely manufacturing technology and therefore origin.

6.1. Glaze analysis method

The method of glaze analysis that was used in this work is that already employed by Colombari and co-workers.¹⁻⁵ The Raman spectrum of the glass/glaze network is composed of broad bands around 500 cm^{-1} and 1000 cm^{-1} . The band at 500 cm^{-1} has been attributed to ν_2 bending vibrations of the isolated SiO_4 unit, while that around 1000 cm^{-1} is composed largely of the stretching vibrations of the coupled ν_1 and ν_3 vibrations.⁵ It is deduced that the highly connected SiO_4 tetrahedral units in the SiO_4 network will have high Raman band intensity from the bending vibrations, as illustrated with arrows in Figure 6.1.1.

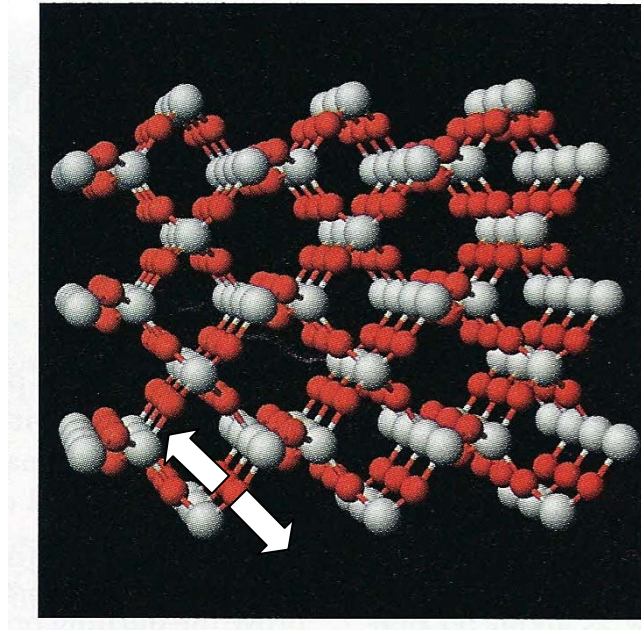


Figure 6.1.1. In highly connected SiO₄ tetrahedral units, such as in the SiO₂ network, the bending vibrations illustrated here with white arrows are most intense and are associated with the 500 cm⁻¹ envelope in the Raman spectrum (Silicon atoms are the grey spheres and the red spheres are those of oxygen atoms.) [The Figure was obtained and modified from Kotz, J.C. and Treichel, P. Chemistry and Chemical Reactivity, 4th Ed, Harcourt Brace College Publishers, Orlando, Florida USA.]

When fluxing agents are added to the amorphous glaze, such as calcium, sodium and other fluxing agents that are used to lower sintering temperatures, this out-of-axis bending vibration is reduced. However, the stretching Si-O vibration that is associated with the 1000 cm⁻¹ region is not affected. It is this difference that led Colombar⁶ to define an index of polymerisation, I_p , such that, $I_p = A_{500}/A_{1000}$, where A_i is the area under the Raman band centred at wavenumber i . It follows that a relationship can be developed between the glass/glaze sintering temperature and the glass/glaze composition.

Since the Raman spectra of porcelain glazes are also generally dominated by broad bands around 500 cm^{-1} and 1000 cm^{-1} , which are associated with ν_2 bending vibrations and the coupled ν_1 and ν_3 Si-O stretching vibrations of the isolated tetrahedra, we focused our analysis in this region. In the deconvolution of the silicate stretching envelope (ca $700 - 1300\text{ cm}^{-1}$) one can define five components within this region, namely Q_0 (originating from an isolated tetrahedron), Q_1 (tetrahedra linked by a common oxygen atom, Si_2O_7), Q_2 (tetrahedra linked by sharing two oxygen atoms, $3\text{Si}_3\text{O}_9$ with n-tetrahedral cycles), Q_3 (tetrahedra linked by sharing three oxygen atoms) and Q_4 (as it appears in pure SiO_4).⁶⁻⁹ These Q_n values are found to have characteristic Raman signatures and should assist in determining the degree of polymerisation of the silicate network and hence the type and concentration of the fluxing agents used.

6.2. Application to blue and white porcelain glaze

Fluorescence in Raman spectroscopy as applied to the study of glazed ceramic artifacts greatly affects the spectral assignment because it can mask spectra collected from the glaze and/or pigments in the sample. In this case the fluorescence emanates from the glaze of the artifacts and is attributed largely to the presence of impurities¹⁰ and the degree of porosity of the glaze under study.¹¹ The use of a confocal set-up in Raman microscopy ensures that mainly the spectrum from the focus point is obtained.¹²⁻¹⁴ This allows the collection of scattered radiation from volumes of the order of one cubic micron at the focus point, thereby discriminating between the glaze spectra and those from the interfacial region (glaze/ceramic). This region is usually composed of decorative pigments and other colouring agents which are then detected through the intervening glaze.^{13,14}

Figure 4.2.1. and Figure 4.2.2 show the glaze depth profile spectra (raw data), illustrating the systematic approach adopted towards obtaining interfacial pigment

Raman spectra. One of the questions raised pertains as to whether the clear ceramic/glaze interfacial pigment spectra so obtained^{13,14} are dependent on the glaze type as a function of the glaze composition and/or of the processing temperature? The glaze on the samples already studied was analysed in order to answer this question.

In addition, the information obtained was used to further compare and contrast Ming porcelain artifacts and shards of archaeological origin. Intact Ming dynasty porcelain plates and a tile shard from the Citadel of Algiers were also studied and comparisons were made. A well-documented method developed by Colomban and co-workers^{7,15,16} for the analysis of glaze/glass was used in the analysis of the glaze. Since the glaze thicknesses of the samples studied are between 0.1 mm and 0.4 mm, laser powers of 40 mW and 20 mW respectively were required.¹³

6.2.1. Samples

The samples used in the glaze studies are the same as those used for the pigment studies. The pigments on these samples have been studied in depth and the results have been reported.^{13,14} Figure 6.1.2 shows the sample set, made up of Ming samples A and B, unknown samples of archaeological origin C, D and F, sample E of Meissen origin and the Citadel tile, sample G. In addition, the Ming plates (samples H and I of the Hongzhi (1488–1505) and Wanli (1573–1620) imperial periods respectively) were also studied.

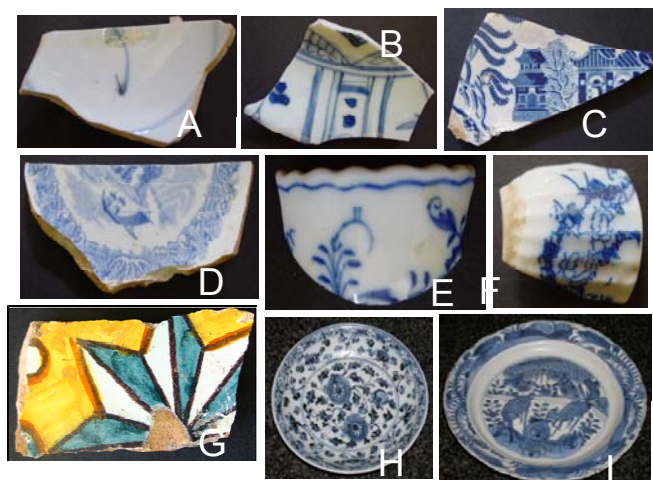


Figure 6.2.1.1. These sets of shards and intact plates are those that were used for the glaze analysis. Samples A and B are Ming shards, C, D and F are of archaeological origin, E is of Meissen origin, H and I are intact museum collection pieces and G is the tile shard from the Citadel of Algiers

The glaze thicknesses were estimated with a ruler and the measurements were made on the broken edges where this was possible. The samples were used as received with no further preparation, apart from wiping with methanol to clean the glaze surfaces where necessary.

6.2.2. Raman and EDX measurements

A Dilor Raman machine (Dilor XY multi-channel spectrometer) with a spectral resolution of about 2 cm^{-1} , equipped with a liquid nitrogen-cooled CCD detector was used in the Raman measurements. An Olympus confocal microscope in a 180° backscattering configuration was attached to the spectrometer. 50X and 100X windows were used for the silicate glazes found on the blue and white porcelain samples and Olympus objective lenses with long focal lengths were used. Integration times were typically between 120 and 300 seconds, with two to three accumulations in each spectrum.

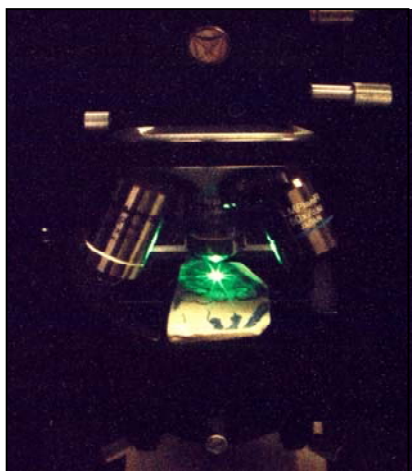


Figure 6.2.2.1. The Figure illustrates the position of the shard in a normal horizontal position for probing the glaze directly. This position is also ideal for probing the ceramic/glaze interface through the glaze on the shards.

The excitation radiation was 514.5 nm wavelength supplied by an Innova 300 argon ion laser with the power set typically at between 0.5 mW and 40 mW. The laser powers are reported as measured at the sample, the target being the glaze and not the pigment in those samples that had some pigment exposed to the surface. Data acquisition, baseline corrections and spectra processing were carried out with LabSpec® software (Jobyn Yvon, Horiba Group).

Peak fitting was undertaken with Origin® software (Microcal Software Inc.). The EDX measurements were carried out with a JEOL JSM – 5800LV scanning electron microscope operated at low vacuum, with an accelerating voltage of 20 kV. The use of low vacuum eliminated the need for gold sputtering to enhance surface conductivity.

6.2.3. Results on sample glazes

The raw data Raman spectra collected from the glaze surfaces to the interfacial region of the porcelain samples are shown in Figure 4.2.1. and Figure 4.2.2., where used in the glaze analysis studies. Only the glaze surface spectra of the samples were used in these studies in order to compare the various glaze properties.

It was also found that relatively high fluorescence emanated from the intact Ming plates (samples H and I) and both the Ming shards (samples A and B) show intermediate and mutually similar relative fluorescence intensities. This is in contrast to the unknown archaeological shards (samples C, D and F) and the Meissen shard (sample E), which showed relatively little fluorescent activity, making it easier to probe through the glaze. Visually, the unknown shards of archaeological origin and the Meissen shard show a clear transparent glaze as compared with the Ming porcelain (shards and intact plates), which have a tint of white inside the glaze due to the higher density of bubbles or air pockets in the glaze. This high density of bubbles in the glaze qualitatively correlates with increased fluorescence. In the case of porcelain glaze, fluorescence is usually attributed to organic or inorganic contaminants in the open pores within the glaze.⁸

Since the high laser powers used on these blue and white samples is expected to have cleaned the glaze surfaces of any organic impurities, the relative degrees of fluorescence intensity on these samples is most likely due to inorganic impurities, the glaze composition and/or the microstructure rather than that from surface-borne organic impurities.

Organic or inorganic impurities trapped inside the glaze could also give rise to fluorescence. The glaze spectra from all the samples were similarly treated by a

two-point correction to remove the slope and move the baseline to zero. The baseline corrections were effected by LabSpec® software.

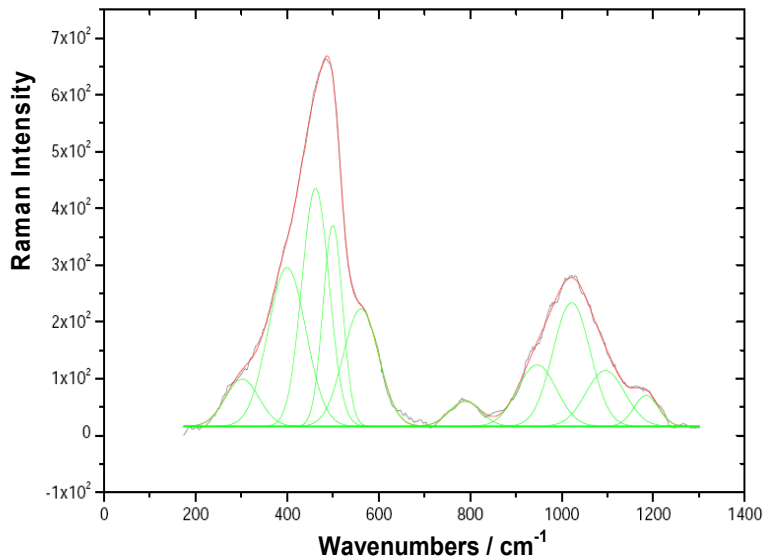


Figure 6.2.3.3. Representative deconvolution results from glaze spectra (514.5 nm wavelength radiation; 50X objective lens). Figure 4.2.1. (a) was used in the illustrated deconvolution.

The same smoothing functions within the same spectral window between 200 cm^{-1} and 1300 cm^{-1} were used to prepare spectra before a Gaussian function was applied in a peak-fitting procedure using the Origin® curve-fitting software to produce the spectra shown in Figure 6.2.3.3. Since the index of polymerisation ($I_p = A_{500}/A_{1000}$) is correlated with the processing temperature and composition of glassy silicates,⁶ this parameter was calculated from the Raman signature of the various glaze types and used to predict the glaze properties. The data extracted from Figure 6.2.3.3 are shown in Table 6.2.3.1.

Table 6.2.3.4. Peak maximum as obtained from the deconvolution process of the glaze spectra for the various blue and white samples and the calculated index of polymerisation (I_p). The νQ_n values are indicated in cm^{-1}

Sample	νQ_0	νQ_1	νQ_2	νQ_3	νQ_4	I_p
Ming A	803	937	1006	1061	1134	1.4
Ming B	798	951	1022	1089	1162	2
Unknown C	794	938	1007	1083	1161	2.7
Unknown D	789	945	1011	1093	1174	2.3
Unknown F	795	939	1012	1086	1166	4
Meissen E	798	964	1026	1093	1165	1.8
Plate H (Hongzhi)	782	919	975	1040	1118	2.1
Plate I (Wanli)	788	946	1021	1095	1184	2.4
Tile G						0.3

The index of polymerisation from Table 6.2.3.1 is also presented graphically in Figure 6.2.3.4, which gives values for the I_p per sample, showing the spread of the index of polymerisation (I_p) for the various samples. At $I_p = 0.3$ for the tile glaze, it may indicate sintering temperatures of < 600 °C for this tile shard.⁶ The rest of the samples show I_p values above 1.3 which could indicate sintering temperatures well above 1 000 °C.

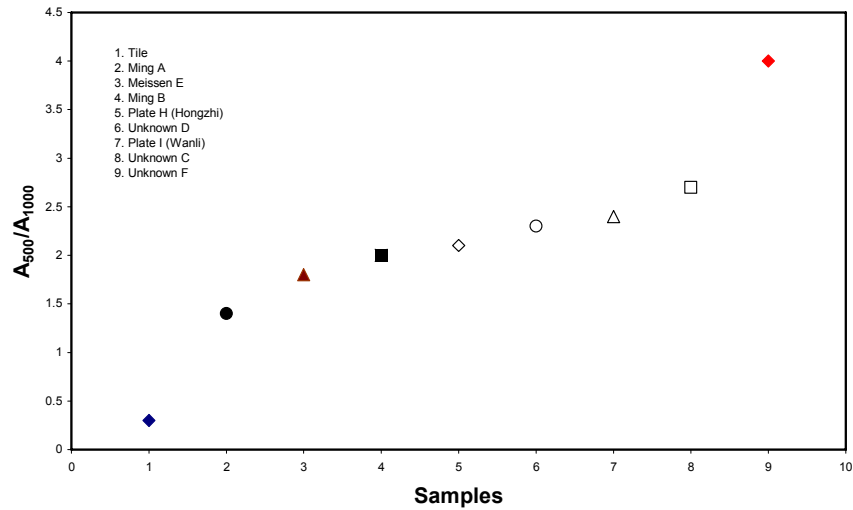


Figure 6.2.3.4. Plot of the A_{500}/A_{1000} ratio (index of polymerisation, I_p) of the various samples. This ratio has been found to correlate closely with the sintering temperature of the glaze

Differentiation between lead-based and alkali-based glaze types is possible,^{6,9} while processing temperature determinations follow directly from consideration of the degree of connectivity of the SiO_4 polymeric units, which are determined from the relative Raman intensities of the Si-O bending (500 cm^{-1}) and stretching (1000 cm^{-1}) modes.⁷

The EDX results (Table 6.2.3.2) also show the weight of Pb in the tile glaze to be approximately 53%, the highest in the set of samples.

Table 6.2.3.2. EDX data listing the main elements in the glaze of the selected samples

Element (Wt%)	Ming A	Ming B	Unknown C	Unknown D	Unknown F	Meissen E	Tile G
Na	0.15	1.03	0.99	0.83	1.06	0.64	0.14
Mg	0.23	0.07	0.56	0.29	0.07	1.05	0.2
Al	9.74	8.8	8.41	8.53	7.86	11.32	2.01
Si	57.97	62.49	52.64	47.98	66.52	64.16	28.5
K	8.49	9.7	7.52	5.99	12.73	7.28	3.7
Ca	20.32	14.52	8.3	16.89	6.32	12.86	0.65
P	0.09	0	0.1	0.11	0.07	0.18	0.09
S	0	0	0	0	0	0	0
Cl	0.27	0.11	0	0.07	0.09	0	0.12
Ti	0.35	0.16	0.38	0.3	0.09	0.13	0.07
Fe	2.24	3.08	1.54	0.59	1.89	2.38	0.44
Co	0.15	0.03	0.52	0.34	0	0	0
Pb	0	0	19.03	18.09	3.35	0	52.71
Sn	n.d.	n.d.	n.d.	n.d.	n.d.	n.d.	9.78

(n.d. = Not determined)

These glaze types contain lead, alkaline earth metals and alkali metals acting as fluxing agents that lower the glass transition temperature of the glassy networks. Both the Ming samples (A, B, H and I) and the unknown samples show I_p values far above 1.3, corresponding to glass transition temperatures of about 1 000 °C or more.⁷ Again, the EDX results confirm the dominance of Ca over Pb in the Ming samples. There is no detectable lead content in the Ming samples. Note that only shards, and not intact plates, were used in the EDX studies due to the small size of our EDX instrument sample chamber.

The Meissen sample (E), with an I_p of 1.3, also corresponds to Ca-based glazes (Pb-poor), with Raman-predicted glass transition temperatures of about 1 000 °C or more (see also Table 6.2.3.2 for EDX data confirming the Meissen shard glaze composition). These results are also consistent with those of other Meissen porcelain studies.¹⁶ The depth profiling method can also be used to estimate the glaze thickness on intact ceramic artifacts. The glaze thicknesses of the samples are listed in Table 6.2.3.3, as estimated by direct measurement with a ruler (in the

case of the broken shards) and by using a laser beam (all listed samples) to reach the ceramic/glaze interface.

Table 6.2.3.3. Glaze thicknesses of the samples studied as determined by direct measurement using a ruler and by approximate location of the ceramic/glaze interface using a laser beam

	Ming A	Ming B	Unknown C	Unknown D	Unknown F	Meissen E	Tile G	Plate H (Hongzhi)	Plate I (Wanli)
Thickness (mm)	0.4	0.4	0.1	0.1	0.1	0.2	n.d.	-	-
Thickness (μm)	450	424	124	128	116	240	n.d.	394	420

(n.d. = Not determined).

6.4 Conclusion

The glaze types on all the blue and white ceramic samples studied in this work ranged from Ca-based (samples A, B and E) to Pd-dominated (samples C, D and G) and had glass transition temperatures ranging from high ($\sim 1\ 000\ ^\circ\text{C}$ or more) to low ($\sim 600\ ^\circ\text{C}$). All the types were studied successfully by using the depth profiling method. The SnO_2 -dominated glaze type of the tile shard from the Citadel of Algiers was also successfully probed using this method. The variation in the value of the index of polymerisation ($I_p = A_{500}/A_{1000}$), which is known to be closely correlated with the degree of polymerisation of the silicate network and is affected by the type and concentration of fluxing agents in the glaze, shows that the samples are vastly different and have had different manufacturers. This result further supports the conclusions reached in an earlier study,¹³ namely that the two groups of shards (Ming and archaeological) are not likely to have a common origin. Using the depth profiling method, we are also able to approximate the glaze thickness on intact ceramic pieces.

6.5 References

1. Colomban, P., Liem, N.Q., Sagon, G., Tinh, H.X. and Hoành, T.B. *J. Cult. Heritage*. 2003, **4**, 187.
2. Colomban, P., Milande, V. and Le Bihan, L. *J. Raman Spectrosc.* 2004, **35**, 527.
3. Colomban, P. and Truong C. *J. Raman Spectrosc.* 2004, **35**, 195.
4. Prinsloo, L.C. and Colomban, P. *J. Raman Spectrosc.* 2008, **39**, 79.
5. Prinsloo, L.C., Wood, N., Loubser, M., Verryn, S.M.C. and Tiley, S. *J. Raman Spectrosc.* 2005, **36**, 806.
6. Colomban, P. *J. Non-Cryst. Solids*. 2003, **323**, 180.
7. Colomban, P., March, G., Mazerolles, L., Karmous, T., Ayed, N., Ennabli, A. and Slim, H. *J. Raman Spectrosc.* 2003, **34**, 205.
8. Liem, N.Q., Thanh, N.T. and Colomban, P. *J. Raman Spectrosc.* 2002, **33**, 287.
9. Colomban, P. and Treppoz, F. *J. Raman Spectrosc.* 2001, **32**, 93.
10. Osticioli, I., Zoppi, A. and Castelluci, M. *J. Raman Spectrosc.* 2006, **37**, 974.
11. Colomban, P. *Mater. Res. Soc. Symp. Proc.* 2005, **852E**, 008.4.1.
12. Huang, P.V. *Vibrational Spectrosc.* 1996, **11**, 17.
13. Kock, L.D. and de Waal, D. *J. Raman Spectrosc.* 2007, **38**, 1480.
14. Kock, L.D. and de Waal, D. *Spectrochim. Acta.* 2008, **71A**, 1348.
15. Colomban, P., Tournie, A. and Bellot-Gurlet, L. *J. Raman Spectrosc.* 2006, **37**, 841.
16. Colomban, P. and Milande, V. *J. Raman Spectrosc.* 2006, **37**, 606.

Chapter 7

Overall conclusion

Raman spectroscopy analysis of underglaze pigments of porcelain of archaeological origin was undertaken. The samples that were used in the study form four categories: (1) shards of unknown origin from archaeological sites around Pretoria, kept by the National Cultural History Museum, and shards of Ming origin also from the National Cultural History Museum in Pretoria; (2) one shard of Meissen origin from Germany; (3) intact plates from the Ming dynasty, as well as one intact plate of unknown origin; and (4) a tile shard from the Citadel of Algiers.

Raman spectroscopic analysis was undertaken, with additional techniques being used to complement the Raman work, namely energy-dispersive X-ray spectrometry (EDX) and X-ray powder diffractometry (XRD). Synthesis methods were also used to aid in the characterisation of pigments. Reference compounds were synthesised and their analyses were compared and contrasted with those it was intended to identify on the artifacts.

The overall study proved very successful in the characterisation of all the pigments on all the samples that were chosen for the study. Firstly, cobalt blue was positively identified on all of the blue and white porcelain shards and plates, except on the unknown intact museum plate on which an olivine-type blue pigment was identified. Comparative studies between the Ming blue pigment and the blue pigment on the pieces of unknown origin were used to look for differences between these two groups that could be used to indicate differences in place of origin or manufacture. For instance, the use of amorphous carbon to darken the blue pigment on the unknown shards is not known to have been common among the Ming manufacturers.

Secondly, the use of white (hence pure) anatase to whiten the surface of the porcelain artifact before the application of the glaze is also not found to be common among the Ming manufacturers.

These differences could be used by archaeologists in solving some of the mysteries emanating from excavated porcelain shards from archaeological sites.

Studies of pigments on the tile shard from the Citadel of Algiers also proved very successful. All pigments were identified and characterised, except for the blue pigment on the tile for which Raman spectroscopy was unable to yield a spectrum. However, a cobalt blue spectrum was eventually obtained from a crevice on the surface after repeated attempts to probe the surface. It has been shown elsewhere that cobalt ions dissolved in the glaze do not give a distinct Raman signature but do give a brilliant blue colour. The ancient ternary (Pb-Sn-Sb) pigment that was also identified on the yellow section of the tile was successfully characterised and for the first time – a Pb-O vibration for this pigment was assigned at 127 cm^{-1} .

The method of glaze depth profiling uniquely employed during these studies proved very useful, especially in probing underglaze pigments on all the blue and white porcelain (shards and plates), and can now be used in further studies to compare and contrast pigments from museum pieces with those of archaeological origin. This technique will certainly complement the analytical techniques that are employed by archaeologists.

Overall, these studies proved very successful. However, due to the small sample group, further work should continue along the same lines in this young field in order to further establish Raman spectroscopy as a routine analysis technique in art and archaeology.